OBSERVED AND MODELLED CHARACTERISTICS OF THE MARINE ATMOSPHERIC BOUNDARY LAYER OVER THE NORTHEAST PACIFIC OCEAN: A COLD AIR OUTBREAK CASE STUDY

By

Greg Unrau

B.Sc. Atmospheric Science, The University of British Columbia, 1992

A THESIS SUBMITTED IN PARTIAL FULFILLMENT OF

THE REQUIREMENTS FOR THE DEGREE OF

MASTER OF SCIENCE

in

THE FACULTY OF GRADUATE STUDIES

DEPARTMENT OF GEOGRAPHY

DEPARTMENT OF OCEANOGRAPHY

We accept this thesis as conforming

to the required standard

THE UNIVERSITY OF BRITISH COLUMBIA

March 1996

In presenting this thesis in partial fulfilment of the requirements for an advanced degree at the University of British Columbia, I agree that the Library shall make it freely available for reference and study. I further agree that permission for extensive copying of this thesis for scholarly purposes may be granted by the head of my department or by his or her representatives. It is understood that copying or publication of this thesis for financial gain shall not be allowed without my written permission.

Department of Geography
Department of Oceanography
The University of British Columbia
2075 Wesbrook Place
Vancouver, Canada
V6T 1W5

Date: MARCH 30, 1996

Abstract

The Marine Atmospheric Boundary Layer was investigated during a cold air outbreak (CAO) over the Northeast Pacific ocean. The horizontal structure and downwind modification of the lower boundary layer were studied. Considerable moisture is supplied to the atmosphere through the turbulent flux of latent heat. The bulk flux of latent heat increases downwind while the bulk flux of sensible heat decreases. The highest recorded total surface heat flux is 365 Wm^{-2} based on eddy correlation statistics. Turbulence kinetic energy increases downwind and velocity variances were found to be more sensitive to stability than others have observed (Panofsky *et al.*, 1977). A spectral analysis suggests the presence of roll circulations in the horizontal wind components (u, v) and specific humidity q at scales ranging from 5 to 25 km, as well as an increasing roll aspect ratio downstream. Boundary layer height increases downwind but height isolines are oriented more perpendicular to the sea surface temperature gradient than to the mean wind direction.

A quasi-two-dimensional K-theory similarity model (Brown, 1972, 1974a, 1974b) was applied to a 40 $\times$ 40 horizontal grid and was used to estimate surface air velocities, stability and surface sensible heat flux. It incorporates the effects of stratification and baroclinicity and unlike other boundary layer models, explicitly parameterizes large eddy circulations. Model derived near surface air velocities, friction velocities and the flux of sensible heat emulate observed fields reasonably well. Modelled velocities are larger than observed values but not significantly in well determined regions of the model domain. In regions where modelled and observed air velocities agreed poorly, data paucity and nonstationarity effects are the proposed causes.

Table of Contents

List of Tables

List of Figures

Glossary of Acronyms

ABL	Atmospheric Boundary Layer
ABM	Australian Bureau of Meteorology
ACE	Arctic Cyclone Experiment
ADHOC	Advanced Higher Order Closure
AES	Atmospheric Environment Service
AGCM	Atmospheric General Circulation Model
AIDJEX	Arctic Ice Dynamics Joint Experiment
CABL	Convective Atmospheric Boundary Layer
CAO	Cold Air Outbreak
CI	Convective Instability
ECMWF	European Center for Medium Range Weather Forecasting
ERS	Earth Resources Satellite
GALE	Genesis of Atlantic Lows Experiment
GCM	General Circulation Model
GLA	Goddard Laboratory for Atmospheres
GOASEX	Gulf of Alaska Experiment
IPI	Inflection Point Instability
MABL	Marine Atmospheric Boundary Layer
MCC	Mesoscale Cellular Convection
MIZEX	Marginal Ice Zone Experiment

NOAA	National Oceanic and Atmospheric Administration
NWS	National Weather Service
OGCM	Oceanic General Circulation Model
OLE	Organized Large Eddies
PBL	Planetary Boundary Layer
SASS	Seasat-A Satellite Scatterometer
SMMR	Scanning Multi-Channel Microwave Radiometer
STREX	Storm Transfer and Response Experiment
WMO	World Meteorological Organization

Acknowledgements

I could probably write another 150 pages recognizing and exhorting the people who have contributed to this thesis. It will however have to suffice to mention only a few.

First I want to thank my committee members for their helpful comments and valuable direction. Thanks to Dr. Gordon McBean for helpful input and advice during the initial stages of my thesis work. Thanks to Dr. Stephen Pond for his advice and for filling the position of administrative advisor during Dr. McBean's absence. Thanks to Dr. Douw Steyn for accepting the task of first reader and for being an integral part of the honing process as I worked towards the final product. And thanks to Dr. Phil Austin for his input as second reader and for providing invaluable programming and word processing advice.

A special thanks to Robert Key at Princeton for providing the objective analysis software and the Splus know how to implement it.

There is no question that the time I have spent completing this degree would have been dry and lonely without the companionship and love provided by my wife Elaine. Thanks go to her for being unconditionally supportive.

Among the people in the departments of Geography and Oceanography I thank Roy Hourston for his help during the initial months of my research as I attempted to comprehend a lot of new technical information and software. And thanks to Ken Reid for his help and for the good times we shared playing soccer in "The Dome". Other help has come from Joe Tam, Denis "Mr. Emacs" Laplante, Vincent Kujala and Jim Mintha. Mark Allen, Jennifer Shore, Scott Tinis and Markus Kellerhals need mention as well, for their helpful hints and willingness to answer questions.

Financial support for this research was provided by both the Atmospheric Environment Service and the National Science and Engineering Research Council of Canada. Additional personal funding was provided through a Teaching Assistantship in the Department of Geography.

ᵽᵻ᷇ᵽᵻ᷈ ᵽᵻ᷈ ᵬᵻ᷈ ᵴᵹ᷇ ᵽᵌ᷄ ᵽ ᵯᵋ ᵽᵒᵰ ᵒᵽ ᵽᵕᵶ ᵯᵐᵌ᷄::

—Numbers 20:8 (Tengwar Sindarin)

Chapter 1

Introduction

1.1 Introduction

A cold air outbreak (CAO) occurring over an extensive body of water, often produces large vertical transfers of potential and kinetic energy. The energy manifests itself as turbulent fluxes of sensible heat (Q_H), latent heat (Q_E) and momentum (τ). Previous studies have recorded surface total heat fluxes (Sensible + Latent) varying from 600 Wm^{-2} (SethuRaman *et al.*, 1986), to 1174 Wm^{-2} (Grossman and Betts, 1990) and as high as 2015 Wm^{-2} (Vukovich *et al.*, 1991). The climatological sensible heat flux is 20 Wm^{-2} averaged over the entire globe and 15 Wm^{-2} averaged over the ocean surface (Brümmer *et al.*, 1992). During a CAO the Bowen ratio ($\beta = Q_H/Q_E$) is generally between .33 and .50 (see Brümmer *et al.*, 1992; Chou, 1993). Energy transfer is enhanced not only by large sea-air temperature differences, but also by stronger humidity gradients and higher wind speeds. This enhanced transfer qualifies marine CAOs as an excellent framework within which to study air-sea interactions and the associated modification of the marine atmospheric boundary layer.

During a CAO the marine atmospheric boundary layer (MABL) plays a key role in the energy redistribution process. Through turbulent mixing, fluxes of moisture and thermal energy are transferred from near the surface, through the MABL and into the free atmosphere where they have a direct influence on the large scale atmospheric circulation. The horizontal momentum flux is downward under neutral conditions although secondary

circulations can result in a significant upward but spatially variable component. These fluxes result in mixing that occurs at a rate many orders of magnitude faster than the mixing rate for molecular diffusion (Holton, 1979).

Preferred Northern hemisphere locations of CAOs are the Greenland sea, Barents sea and Bering sea, as well as the warm ocean boundary currents on the east sides of the continents, namely the Kuroshio Current and the Gulf Stream (Brümmer *et al.*, 1992). The Greenland and Barents seas produce the largest yearly averaged surface sensible heat fluxes of over 50 Wm^{-2} (Budyko, 1978). Although the Northeast Pacific ocean is not a preferred location, CAOs occur an average of twice per winter season (Okabe, personal communication) and their contribution to atmosphere-ocean exchanges is not trivial.

Two synoptic regimes are responsible for North American CAO events. Off the east coast of the United States and Canada, 15-20 CAOs occur per winter season (Grossman and Betts, 1990). Outbreaks occur in the wake of a cold front where continental arctic (cA) or continental polar (cP) air plunges south-eastward. The frigid air rushes through the Appalachian valleys, then over the North Atlantic ocean where it interacts strongly with the warm Gulf Stream boundary current. This interaction results in some of the largest recorded values of total surface heat flux (Vukovich *et al.*, 1991).

Over the Northeast Pacific on the western side of the continent, the synoptic situation is similar. In the beginning stages of a CAO, the polar jet stream migrates south, accompanied by the surface arctic front. The front displaces warmer air to the south and a high pressure anti-cyclone builds in the Yukon and British Columbia interior. Over the mainland a strong stable lapse rate is established and cloudless conditions prevail with strong winds through mountain valleys and coastal fjords (Jackson, 1993). Radiational cooling causes further temperature decreases leading to concomitant increases in both air density and surface pressure. In the vicinity of the quasi-stationary arctic front is a low pressure system off the southwest coast of British Columbia or the northwest portion

of Washington State. This regime causes cold arctic air to advect across the British Columbia coast and out over the Northeast Pacific ocean.

Over water, the MABL is modified significantly in the downwind direction. Dynamically or convectively driven organised secondary flows may develop, and depending on the stability and moisture characteristics of the air, cloud streets may form. Downstream, boundary layer depth has been observed to increase while roll vortices decay into mesoscale cellular convection (MCC) (see Hein and Brown, 1988; Grossman and Betts, 1990; Vukovich *et al.*, 1991; Brümmer *et al.*, 1992). Internal MABL dynamics are far from completely understood. Further study is imperative if full knowledge of the turbulent energy exchanges at the air-sea interface and their influence on both the MABL and the larger scale atmospheric dynamics, is to be realized. The purpose of this study is to examine a CAO disturbed MABL as modified by interaction with an underlying ocean surface.

1.2 Motivation

Coupled global circulation models still lack adequate parameterizations of MABL processes (Kiehl, 1992). The parameterizations available for short- and medium-range weather forecasting are accompanied by a 20% uncertainty at low to moderate wind speeds, and a larger one at high wind speeds (Hasse, 1990). A consequence of poor parameterizations is climate drift when Oceanic General Circulation Models (OGCM) are coupled to Atmospheric General Circulation Models (AGCM) and a number of flux correction schemes have been suggested to compensate for the observed drift.

One source of model drift is disagreement between AGCM computed surface heat fluxes and OGCM computed surface heat fluxes. Weaver and Hughes (1995) suggest that the mismatch magnitude between OGCM and AGCM surface heat and freshwater fluxes

is not as important for climate drift as the difference in OGCM and implied AGCM heat and freshwater mass transports. It has also been observed that even with flux corrections which are usually added at each time step, the coupled model can still exhibit slow drift (Cubasch, 1989). The ultimate goal is to eliminate any flux corrections primarily by developing more accurate boundary layer parameterizations of the dynamical processes which contribute to the coupled air-sea system. There are a number of key ingredients which when combined, maximize the accuracy of an AGCM parameterization. These include: an accounting for the dependence of boundary layer height on surface conditions, sufficient robustness to respond to different surface types, and a need to distinguish between conditions where the thermal structure is unstable, neutral or stable. Also needed is consistent coupling with other parameterizations used in the free atmosphere domain above, and those used in the ocean domain below. Further study of the boundary layer processes which depend upon air-sea interaction is therefore needed to develop parameterizations which not only meet the aforementioned requirements but are also computationally feasible. This is one motivation for this thesis.

A second motivation for this study is in response to the lack of literature addressing the CAO disturbed MABL over the Northeast Pacific ocean. This study is the the first of its kind over this region. Similar investigations have been done by Brümmer *et al.* (1992) over the Spitsbergen Current in the Eastern Atlantic, and by Vukovich *et al.* (1991) over the Gulf Stream. The Northeast Pacific does not offer the extreme wintertime air-sea temperature gradients found at western boundary currents, nevertheless, it is of import to verify and to possibly universalize the observed character of the lower atmosphere during such energetic and influential synoptic events.

1.3 Objectives

Two objectives underly this thesis. The first will attempt to answer two related questions using the described technique(s):

- What is the mesoscale structure of the modifying lower MABL during a CAO in both the horizontal and vertical directions?
  - Investigate profiles of temperature and moisture.
  - Investigate horizontal distribution of near surface moisture, temperature, wind, energy fluxes and turbulence quantities.
- How is this structure related to the turbulent energy exchanges taking place at the air-sea interface?
  - Investigate relationships between turbulent energy fluxes and atmospheric stratification and boundary layer features (large eddies and clouds).

The second objective is to assess the ability of a simple quasi-two-dimensional analytic boundary layer similarity model to reproduce the observed horizontal boundary layer flow structure.

In the next chapter, a brief summary of boundary layer theory is presented along with a review of current understanding of the boundary layer processes during a CAO. In chapter 3, the data acquisition and processing are discussed with an accompanying explanation of the Storm Transfer and Response Experiment (STREX) and the mission which collected the data used in this study. Chapter 4 presents the data analysis including a synoptic summary and in chapter 5, the model output is elucidated with respect to the observational analysis. A summary and conclusions are given in chapter 6.

Chapter 2

Theory and Background

2.1 Introduction

In this chapter, a theoretical framework is developed within which the observational and model analysis is carried out. It consists of a brief review of boundary layer theory, followed by a discussion of boundary layer scaling and the Monin-Obukhov Similarity concept. The CAO modifying MABL is further clarified, and the final sections delve into both the current status of boundary layer modelling and details of the model used in this thesis.

2.2 Boundary Layer Theory

Early concepts leading to the formulation of boundary layer theory came from laboratory experiments of Boussinesq (1877, 1903) and from Prandtl's proposal of the mixing length concept. Boussinesq (1877) was first to suggest eddy viscosity and thermal conductivity coefficients as parameterizations for mean transport by turbulent eddies. Later, Prandtl (1904) presented the basic boundary layer scaling ideas in a Heidelberg lecture and formally introduced the mixing length hypothesis a few years later (Prandtl, 1925).

In previous laboratory shear flow studies, a region near the boundary was found to be influenced by the frictional force or drag of the surface. This provoked researchers to rethink shear flow theory and to consider flows which obeyed potential flow (zero-drag) theory but within some region of which the drag was in fact non-zero. D'Alembert's

paradox as it became known, was resolved by the introduction of the boundary layer idea.

Prandtl realized that if large scale flow is calculated around a rigid body, the thin boundary layer near the surface could be ignored and potential flow theory would apply. But because potential flow theory provides no information about the drag at the surface a separate boundary layer solution is required to include viscous effects. These concepts can be extended to all geophysical fluids.

Near the same time that Prandtl proposed his theories, Ekman (1905) presented an analytical solution for a viscous fluid in laminar motion within a rotating frame. The same laminar solution was found independently by Taylor (1914); however he had applied it to the Atmospheric Boundary Layer (ABL) while Ekman had applied the solution to the Oceanic Boundary Layer. The so called Ekman/Taylor layer and modifications thereof are an important aspect of any description of ABL flow.

2.3 Scaling Regimes

The ABL is often categorized into two distinct regions: the surface layer and the Ekman/Taylor layer. The surface layer is a thin zone (10s to 100s of meters) near the boundary and exhibits strong shear. It is in this layer where the fluxes of heat, moisture and momentum are assumed constant within 10% of their surface values (Stull, 1988). Both similarity theory (see section 2.3.1 below) and mixing length theory (Stull, 1988) predict a logarithmic wind profile in this layer. Observations by Paulson (1970) agree, although Panin (1990) notes that oceanic waves and atmospheric stratification can significantly alter the log profile. Scales of motion within this region are small enough that the Coriolis parameter can be ignored. Turbulent eddies are small and the flow can be considered eddy laminar. The flow is turbulent with respect to the molecular viscosity

but laminar with respect to the eddy viscosity and that laminar-like mean flows coexist with the small scale turbulence. Observations of large scale laminar-like flows lend support to the eddy-laminar hypothesis.

The Ekman/Taylor layer extends from the top of the surface layer to the top of the boundary layer. Here rotation cannot be neglected. This region is much deeper than the constant flux layer and the largest eddy diameter is comparable to boundary layer depth. The boundary layer top is defined as either the beginning of a thin temperature inversion layer or the height at which the boundary layer wind becomes geostrophic. Together these two layers comprise the entire ABL with a total thickness ranging from 100s to 1000s of meters.

Boundary layer scaling is an important technique for providing universal representations of boundary layer processes. Valid scaling relationships are primarily educed using dimensional analysis, along with dynamic similarity and asymptotic limiting (see Brown, 1991; Stull, 1988; Chou *et al.*, 1986). Figure 2.1 indicates the wide variety of vertical scaling classes that are necessary to characterize the full range of boundary layer motion. For the turbulent surface layer, Monin-Obukhov Similarity Theory (MOST) (Monin and Obukhov, 1954; Wyngaard, 1973; Sorbjan, 1986) is used as long as u_* is not zero and mean winds are moderate to strong. The bulk of data used in Chapter 4 were obtained in the lower MABL where these assumptions are valid (i.e. mean winds ranged between 10 and 25 ms^{-1} and u_* values were never zero.)

2.3.1 Monin-Obukhov Similarity Theory (MOST)

MOST allows inferences of certain boundary layer properties through the measurements of others by using empirical or theoretical relationships among those properties (Wyngaard, 1973). In MOST, turbulence details are assumed to depend only on the following four independent variables:

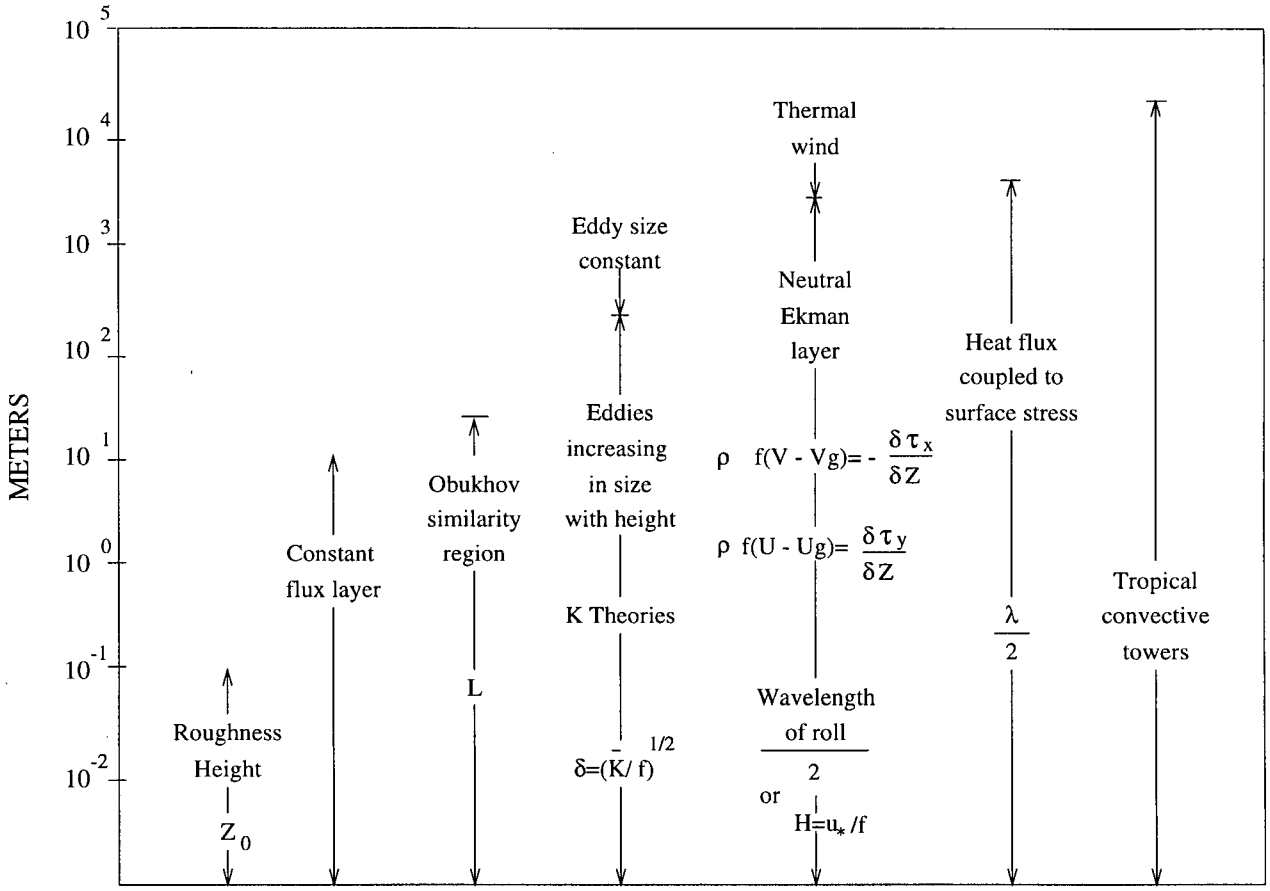

Figure 2.1: Scales present in the full range of boundary layer motions. From Brown (1991).

z	characteristic height
u_*	friction velocity
$H_o/\rho C_p$	kinematic surface sensible heat flux
$g/\overline{\theta_v}$	buoyancy parameter

In the above parameters, ρ is air density, C_p is the specific heat of air at constant pressure, g is the acceleration due to gravity and $\overline{\theta_v}$ is mean virtual potential temperature (in Kelvin degrees). From dimensional analysis (e.g. Buckingham, 1914) and the resulting dimensionless groups, the similarity hypothesis states that dimensionless variables (e.g. wind speed, height, temperature and humidity) are universal functions of the stability parameter z/L where z is height with the origin at the surface and L is the Monin-Obukhov length:

$$L = \frac{-\overline{\theta_v} u_*^3}{kg(\overline{w'\theta_v'})_s} \tag{2.1}$$

where,

k = von Kármán's constant (≈ 0.4)

$(\overline{w'\theta_v'})_s$ = kinematic surface buoyancy flux.

Due to the high costs of both ship and aircraft time, platform motion, salt corrosion etc., the majority of boundary layer theories have been tested against data taken over land. Nevertheless, marine studies that have been carried out do show similarities between the MABL and continental ABL above the first few meters of the surface (see Panin, 1990). Marine atmospheric boundary layers are not subject to the complex topography which so often complicates the study of the continental ABL and MOST can therefore be employed over the ocean assuming surface homogeneity. In the next section, the MABL under the influence of a CAO is further clarified. Previous studies are summarized and the known mechanisms driving MABL circulation are explored.

2.4 Cold Air Outbreaks (CAOs) and the Marine Atmospheric Boundary Layer (MABL)

CAOs cause multiple scale disturbances of trenchant air-sea interaction. The often large associated property gradients evoke intense and complex energy exchange processes varying from voluminous fluxes of heat, moisture and momentum to extensive dynamically or convectively driven large eddy circulations to semi-organized convective plumes (Hein and Brown, 1988; Chou, 1993; Grossman and Betts, 1990; Vukovich *et al.*, 1991). Due to increased energy exchange, the boundary layer character is substantially altered by the resulting heat, moisture and momentum fluxes.

2.4.1 Observations of CAO Modifying MABL Structure

With the development of better MABL observational programs using aircraft and remote sensing, came the ability to investigate the more complex details of air-sea energy transfer under a wide range of synoptic conditions including CAOs. Palmen and Newton (1969) showed that 70% of the total change in oceanic heat storage occurs in winter and in studies cited by them, it is suggested that the greatest changes in ocean heat storage occur in the latitude belt 30-40 degrees in winter. The heat loss of 70 Wm^{-2} is twice the summer maximum. Zhao and McBean (1986) also found that most ocean to atmosphere heat transfer occurs during winter. By using ship reports and applying them to a bulk method for sensible and latent heat, Budyko (1963) found that the most intense energy exchange from ocean to atmosphere is off the Japanese and U.S. east coasts. Bunker and Worthington (1976) added to the findings of Budyko (1963) by calculating the annual heat loss from the ocean to the atmosphere (380 Wm^{-2}) centered on a line between 40N, 56W and 35N, 72W. They noted that this area is often inundated with dry, cold wintertime air flowing over the warm Gulf Stream. Bunker (1976) extended this work

and calculated monthly estimates of sensible and latent heat flux for selected areas over the North Atlantic. In an area near the annual heat loss maximum, he showed that total heat loss for January was 550 Wm^{-2} (150 Wm^{-2} sensible, 400 Wm^{-2} latent), a substantial portion of which can be associated with CAOs from the continent flowing over the warm water of the Gulf Stream.

The early 1970s saw the start of large scale data collection programs, devoted specifically to the study of air-sea interaction during CAOs. From the Global Atmospheric Research Program (GARP) Air Mass Transformation Experiment (AMTEX) (Lenschow, 1972; Lenschow and Agee, 1974, 1976) estimates of sensible heat loss over the Kuroshio current indicated nearly a twofold increase during CAOs (WMO, 1981). Total fluxes of greater than 750 Wm^{-2} were observed. In 1982 the Mesoscale Air-Sea Exchange Experiment (MASEX) (Chou and Atlas, 1982) was conducted off the east coast of the U.S. Four daylong experimental flights were conducted during CAOs. Chou and Atlas (1982) used mixed layer scaling on the 20 January CAO, and found a shear-dominated mixing regime, corresponding to a dynamically driven circulation as opposed to a convectively driven one. Other recent field programs devoted in part or in full to studying CAO boundary layer modification were: the Genesis of Atlantic Lows Experiment (GALE) (Dirks *et al.*, 1988), the 1983 Marginal Ice Zone Experiment (MIZEX) (Kellner *et al.*, 1992; Hein and Brown, 1988) the 1984 Arctic Cyclone Experiment (ACE) (Hein and Brown, 1988), Arktis '88 (Brümmer, 1989), and the Konvection and Turbulence experiment (KONTUR) (Hoeber, 1982).

Vukovich *et al.* (1991) studied CAO MABL evolution off the U.S east coast using GALE aircraft and satellite data, combined with results from a simple one dimensional (vertical) time-dependent boundary-layer model. They found that the heat flux distribution off the coast rapidly produced large horizontal temperature (10 °C) and humidity (4 $g\,kg^{-1}$) differences over distances on the order of 100 km. The boundary layer destabilized

over short distances offshore and MABL depth increased rapidly. The bulk estimates of heat fluxes suffered from considerable uncertainty in the values of the exchange coefficients for heat and water vapor due to the variations of wind speed and stability. Lidar estimates of boundary layer height were as high as 2200 m. Wind speeds were observed to increase offshore.

In another study, (Grossman and Betts, 1990) used GALE data to investigate air-sea interaction during an extreme CAO. The vertical θ_v gradients indicated a slightly unstable subcloud layer which became progressively more unstable downstream. These were similar to observations made in CAOs from the coast of China (Riehl, 1979). A downwind increase in wind speed occured and nearly constant wind direction with height was observed. The wind profile shape may have been the result of a balance between frictional veering of the wind and backing resulting from cold air advection. Estimates of stability were based on the virtual potential temperature gradient and z_i/L, with the boundary layer height (z_i) chosen to include the cloud layer. In an extreme CAO case, where the maximum sea-air temperature difference was 23 degrees, the subcloud layer depth decreased with fetch while cloud layer top height (primarily stratocumulus overcast) increased downwind.

2.4.2 MABL Flow Regimes and Forcing Mechanisms During a CAO

2.4.2.1 Roll Vortices

For a comprehensive review of roll vortices in the ABL see Brown (1980) and Etling and Brown (1993). These atmospheric phenomenon often manifest themselves as horizontally oriented quasi two-dimensional vortices (see Figure 2.2) with a distinct counter rotating circulation. The pattern results in regions of predominant upward motion alternating with regions of mean downward motion. Most observations of organized eddy circulations

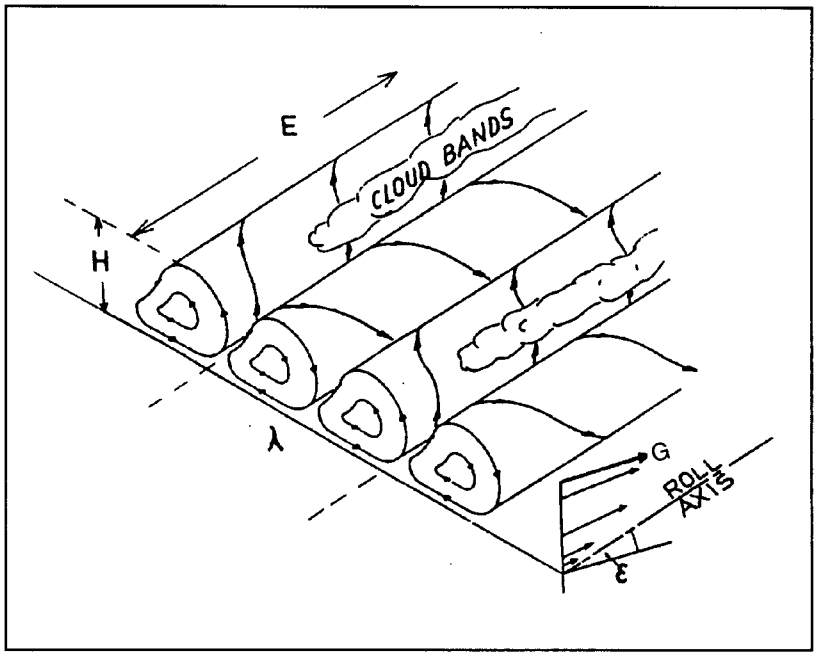

Figure 2.2: Schematic showing idealized roll vortex structure and circulation, and associated atmospheric phenomenon (cloud bands or streets). G is the geostrophic wind. Remaining variables are described in the text. From Etling and Brown (1993).

have been during CAOs over water where cloud streets usually form in the preliminary stages of boundary layer modification (i.e. just offshore). They have also been observed over land but topographical effects usually result in a very short horizontal extent.

A number of early tracer studies using seagulls (Woodcock, 1940, 1942), clouds (Küttner, 1959; Plank, 1965) and insects and snow (Frisch *et al.*, 1974) give evidence for the existence of secondary circulations in the ABL. Other recent boundary layer investigations have noted the presence of such geophysical fluid flows, based on satellite imagery, spectral analysis or doppler radar output (Pennell and LeMone, 1974; LeMone and Pennell, 1976; Grossman, 1982; Walter and Overland, 1984; Walter, 1986; Atlas *et al.*, 1986; Hein and Brown, 1988; Chou and Ferguson, 1991; Martin and Bakan, 1991). From these studies, the structural aspects of roll vortices (Figure 2.2) can be summarized as follows:

vertical extent	H	1–2 km
"wavelength"	λ	2–20 km
aspect ratio	λ/H	2–15
downstream extent	E	10–1000 km
orientation of roll axis to near surface wind	ϵ	-20° to +30°
life time	τ	1–72 h

In two early studies, Küttner (1959, 1971) found that if 3-D convection is to be suppressed, and longitudinal rolls are to dominate, a mean value of shear gradient, $\frac{\partial^2 U}{\partial z^2} > 10^{-5}$ $\mathrm{m^{-1}s^{-1}}$, is required. Plank (1966) showed that there must be criteria other than a critical shear gradient necessary for cloud row formation. LeMone (1973, 1976) used aircraft and tower measurements to study rolls. She found that they consistently occured in moderate winds (< 5 $\mathrm{ms^{-1}}$) and slightly unstable stratification. Furthermore, the turbulent interaction terms (see LeMone, 1973, eqns. 2.7 and 2.11) were deemed unimportant but the distribution of small-scale turbulence *was* modified by the rolls. Previously, roll vortices were considered mainly as merely a good example of dynamical and thermal instabilities in geophysical flows (Etling and Brown, 1993). More recent data obtained from some of the field programs mentioned have suggested the importance of large eddies in the vertical transport of momentum, heat and moisture within the ABL although Chou (1993) suggests that this importance may be limited to momentum transfer as he found no roll signal in computed temperature and moisture spectra.

Recently, Brümmer *et al.* (1992) observed horizontal MABL structure and downwind modification during a moderate to weak CAO near Spitsbergen as part of the Arktis '88 experiment. They observed a rather slow boundary layer depth increase downstream with cloud streets already present at the ice edge. Rolls near the ice edge were generated by dynamical instability due to vertical wind shear at the inversion although

further downstream, thermal instability was more significant and dynamical instability contributed less to MABL circulation. On 15 May 1988, there were no significant downstream variations of the heat fluxes but the next day, fluxes systematically decreased due to a downwind decrease in wind speed. Furthermore, the aspect ratios of rolls increased downstream but were larger than the classical Rayleigh instability aspect ratio of 2.8. Miura (1986) and Kelly (1984) also observed increasing downwind aspect ratios during cold air outbreaks. Hein and Brown (1988) looked at aircraft data from both MIZEX and ACE. Using power, coherence squared and phase spectra they were able to systematically separate rolls from organized plumes. They found that rolls become increasingly more convective in character with distance downstream.

At present there still remains disagreement on the mechanism driving ABL eddy circulations. Theory suggests two likely possibilities: inflection point instability (IPI) and convective instability (CI).

Inflection Point Instability (IPI) In barotropic Ekman flow, the equilibrium shear flow is a balance between Coriolis, pressure gradient and friction forces. The coordinate system used is defined with x and y in the along wind and cross wind directions for the near surface wind, respectively. The flow solution from Etling and Brown (1993) is:

$$U(\hat{z}) = G[\cos\alpha - \exp^{-\hat{z}}\cos(\hat{z}-\alpha)] \tag{2.2}$$

$$V(\hat{z}) = G[-\sin\alpha + \exp^{-\hat{z}}\sin(\hat{z}+\alpha)] \tag{2.3}$$

where,

$\hat{z} = \frac{z}{\delta}$ and $\delta = (\frac{2K_e}{f})^{1/2}$ (Ekman height)

α = angle between the near surface wind axis and the geostrophic flow G

z = height above the surface

K_e = eddy momentum transfer coefficient (eddy viscosity)

f = Coriolis parameter.

The turning angle α is measured counter-clockwise from G to U ($\hat{z} \approx 0$) in the northern hemisphere. The vorticity of the background flow is $\zeta_b = \frac{-\partial U}{\partial z}$ and the vorticity profile exhibits a maximum whose magnitude depends on α. The extremum in the vorticity profile corresponds to an inflection point in the velocity profile. Shear flows with vorticity extrema are unstable with respect to small perturbations. A number of studies have investigated this instability as it relates to ABL shear flows (see Lilly, 1966; Faller and Kaylor, 1966; Etling, 1971; Brown, 1972; Asai and Nakasuji, 1973) and many have found the most unstable mode to be at $\epsilon = 14^o$ to the left of the geostrophic wind in neutral stratification. With no surface heating, the maximum growth rate is smallest for unstable stratifications and increases with increasing static stability. The reason is that $\frac{\partial U}{\partial z}$ at the position of the lowest inflection point is larger in stable and smaller in unstable stratifications; at the same time, K_e at these heights is larger in unstable and smaller in stable stratifications.

Most mathematical analyses (e.g. Etling and Wipperman, 1975) agree that the most unstable mode corresponds to an aspect ratio of ≈ 3. Observed cloud streets had similar aspect ratios and it was therefore assumed that IPI was the cause. In contrast, the parallel instability mode found by Lilly (1966) was a result of a link between the along-axis velocity component u and the vorticity equation. It occurs at $\alpha = 15^o$ and at a $\lambda = 6H$, larger than the IPI mode. In linear stability analysis, growth of this mode is slow compared to that of the IPI mode. Another instability mode based on baroclinic shear flow in a rotating frame is "symmetric" instability. It manifests itself as roll like two dimensional circulations but at much larger wavelengths (100 km) than typically sized ABL rolls. Walter and Overland (1984) observed rolls in near neutral stratification ($z_i/L \approx -2$), which suggests the influence of IPI on roll formation.

Convective Instability (CI) Despite good agreement between IPI theory and observations, most researchers attribute the formation of large eddies to forcing by convective instability. Based on the observation that roll vortices in the ABL are seen most often during CAOs over water (or over land in daytime), early investigators suggested that Rayleigh-Benard instability was the driving mechanism. This is the cause of most convective clouds in the atmosphere. In a shear flow with unstable stratification, linear analysis suggests a longitudinal convective roll regime (Asai, 1970; Kelly, 1977). Deardorff (1972) and Grossman (1982) found rolls when $-25 < z_i/L < -5$ (moderately unstable stratification). In other observations, values of $z_i/L \approx$ -6 to -15 were computed for roll-vortex regimes. These observations have led to the suggestion that rolls are always due to the interaction of thermal convection with boundary-layer shear flow. However there is scatter in the observed aspect ratios of cloud streets which makes it difficult to deduce the underlying mechanism of roll development. Numerical simulations (Chlond, 1992) and field measurements (Brümmer, 1985; LeMone, 1976) indicate a combination of both IPI and CI in near neutral conditions.

2.4.2.2 Mesoscale Cellular Convection

Krueger and Fritz (1961) analysed satellite images containing cellular type cloud structures and found that the cells had diameters of 50–80 km, and had clear centers bounded by a hexagonal ring or U–shaped cloud elements about 15–25 km wide. They were similar in structure to those found by (Benard, 1901) in the lab. Convection cells can occur as either open or closed circulation systems (see Agee *et al.*, 1973; Agee and Dowell, 1974; Burt and Agee, 1977; Sheu and Agee, 1977; Van der Borght and Agee, 1978; Rothermal and Agee, 1980). Radial patterns within the cell structures called *actinae* have been proposed as a transition mode between open and closed cells but conclusive evidence has yet to be presented.

The contribution of numerical simulations to the understanding of MABL dynamics and CAO induced modification is explored next.

2.5 Modelling the MABL

2.5.1 Introduction

Modelling of MABL processes has taken great strides in the last decade as computational power has increased. In this section a discussion of past and present modelling techniques employed to study boundary layer modification is presented along with details of the model used in this thesis.

2.5.2 Previous Modelling Studies of the Modifying MABL

Although this study addresses MABL structure within a specific synoptic situation, the convective atmospheric boundary layer (CABL) exists in conditions other than those of a CAO. The modelling discussion will therefore include CABL simulations of non-CAO boundary layer structure.

Artificial constructs of the CABL vary from simple zero dimensional bulk models (Stage and Businger, 1981a, 1981b; Driedonks, 1982) which can predict boundary layer height evolution, to very high resolution 3-D Large Eddy Simulation (LES) models, capable of resolving actual eddy thermal structures (see Deardorff, 1972; Moeng, 1984; Schmidt and Schumann, 1989). A consistent problem with all current modelling schemes is under-determined sets of governing equations (closure). Both local and non-local closure schemes have been employed with varying success (see Stull, 1988, for a comprehensive review of closure methods). In a comparison of local and non-local turbulence closure methods for the case of a CAO, Chrobok *et al.* (1992) found that simple first-order local closure did not give good agreement with two reference models; one a bulk

model and one a 2-D explicit eddy resolution model. A transilient turbulence model using non-local closure *was* able to parameterize the effects of the large eddies well. The only local closure scheme producing comparable results was one in which eddy diffusivities were parameterized by dimensionless gradient functions. Furthermore it was found that a model with a sufficient fine grid, regardless of dimension, was able to describe the evolution of the CABL very well.

Order of closure is also important to obtaining realistic model simulations. Gradient transport theory (K-theory) is a first order closure method with the second turbulence moments parameterized in terms of the mean vertical shear multiplied by a transfer coefficient. A serious problem with this theory is the apparent violation of the zeroth law of thermodynamics when large eddies produce a counter-gradient flow. See Wyngaard (1973) for a discussion of this problem. Higher order closure schemes do not introduce the same paradox but *do* require increased computation. Many modellers feel that as computer speed continues to increase, K-theory will become obsolete. Brown (1981b) contests that the simplicity of K-theory makes it more desirable than the increased intricacies of higher order closure, especially if the ramifications of secondary flow (i.e. explicit parameterization) are considered and are used to correct a K-theory model. Nevertheless, higher order closure and both higher dimensional and higher resolution modelling remain as important objectives in current atmospheric research. The closure assumption used in the majority of models mentioned above is in fact gradient-transport.

Most modelling efforts simulating realistic CAO-disturbed ABL structure in unstable stratification have had to consider secondary flows. Mason and Sykes (1982) and Mason (1983, 1985) conducted 2-D simulations of the unstably stratified ABL to investigate the structure of 2-D roll circulations. They concluded that CI dominated over IPI for $z_i/L <$ -0.8 and that latent heat release had no marked influence on vortex roll development. Three dimensional large eddy simulations (LES) have helped better the understanding

of turbulence in the CABL, especially with regard to vertical transport of heat, moisture and air pollutants. In 3-D model simulations, the occurence of roll vortices has been limited to unstable stratification. In one of the first atmospheric large eddy simulations, Deardorff (1972) found roll structures for z_i/L = -1.5 and -4.5 but not for z_i/L = -25. Sykes *et al.* (1990) simulated a CAO during GALE using both 2-D and 3-D models. The 2-D model produced organized convection rolls while the 3-D model only produced rolls at early integration times and none later on. Chlond (1992) found from a 3-D simulation of the ABL during a CAO that IPI dominated at the beginning of the CAO and CI, at later times. This result is in contrast to earlier investigations by Mason and Thomson (1987) and Coleman *et al.* (1990) who found no contribution from IPI in 3-D simulations.

2.5.3 The Brown Model

Brown's equlibrium boundary layer model (Brown, 1991; Brown and Liu, 1982; Brown, 1972) is based on the simultaneous solution of the modified mean flow (including perturbation terms) Navier-Stokes equation (see Brown, 1991, pg. 436), a stability equation and an energy equation. Equilibrium is reached when the mean velocity profile has been modified to a point where the energy flux from the mean to the perturbation component of the flow becomes zero (Brown, 1991). Although the model assumes IPI is the driving mechanism for roll formation, the roll shape has been found to be very similar to observations in strongly convective regimes. Furthermore, the model produces roll characteristics which closely resemble the rolls produced in numerical solutions that produce nonlinear equilibrium flows.

Due to the differing physical processes governing the flows in both the surface layer and the Ekman/Taylor layer, there are necessarily two distinct flow solutions (i.e. modified Ekman layer and log surface layer).

Rossby and Montgomery (1935) patched Prandtl's logarithmic parallel flow layer to

Ekman's exponential planar spiral and obtained the following similarity solutions for neutral barotropic flow:

$$\left[\frac{kG}{u_*}\right]\sin\alpha = -B \tag{2.4}$$

$$\left[\frac{kG}{u_*}\right]\cos\alpha = -A' \equiv \ln\left[\frac{ku_*}{fz_o}\right] + A \tag{2.5}$$

where,

k = von Kármán's constant,

G = geostrophic wind,

u_* = surface friction velocity,

z_o = surface roughness length,

B, A and A' = arbitrary patching parameters.

They did not have the consequent Ekman flow solution modified by stratification dependent secondary flow and were further hindered by the lack of a suitable parameterization of surface layer stratification effects which Businger *et al.* (1971) presented nearly 40 years later.

Brown (1974a, 1974b) integrated the ideas of Rossby and Montgomery (1935) and Businger *et al.* (1971) into a two layer 1-D(z) patch solution including stratification dependent secondary flow. His model employing K-theory for both layers, yields equations 2.4 and 2.5 with explicit analytic expressions for A and B as functions of λ_R (a height scale ratio) and the stratification parameter Ψ. The 2-layer model (Figure 2.3) yields a finite perturbation solution for the outer boundary layer which is then patched to the accepted logarithmic surface layer. The similarity solution is based on computing the geostrophic drag coefficient u_*/G:

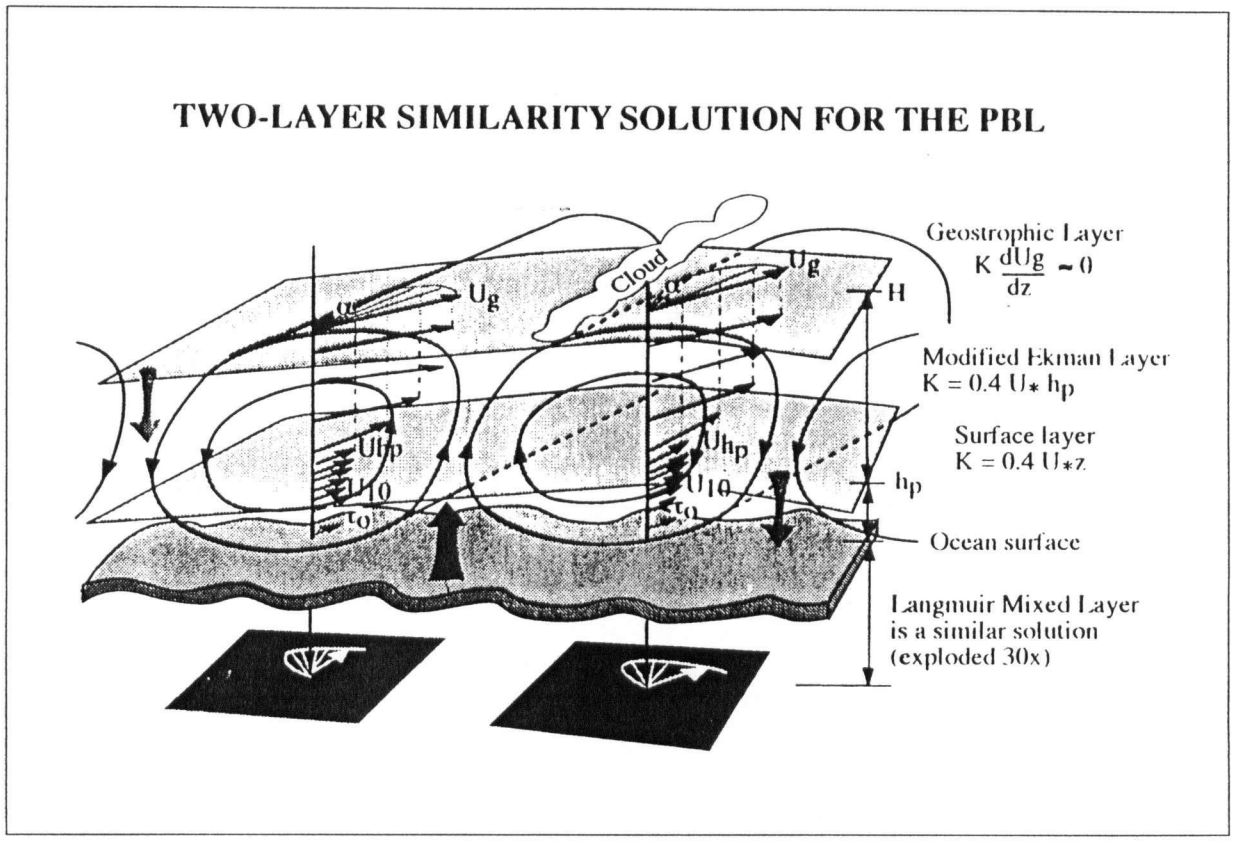

Figure 2.3: Brown's (Brown and Foster, 1994) two-layer similarity model. OLE circulations are shown as counter rotating roll vortices. Hodographs at two stations are shown including surface stress (τ_o), U at 10 m, patch height (h_p), geostrophic height (H) and turning angle (α).K is eddy viscosity, U_* is friction velocity and z is height.

$$\frac{u_*}{G} = \mathcal{F}(MSLP, \Delta T, T_{(x,y)}) \tag{2.6}$$

where,

$MSLP$ = mean sea level pressure,

ΔT = Sea-Air temperature difference,

$T_{x,y}$ = horizontal temperature gradients.

The drag coefficient is determined with respect to the height scale ratio $\lambda_R = h_p/\delta$ where h_p is the patching height (equated with surface layer top) and $\delta = (2K_e/f)^{1/2}$ is the outer layer characteristic scale where K_e is the eddy viscosity coefficient at h_p and f is the Coriolis parameter.

The basic equations are:

1. SURFACE LAYER SOLUTION $(0 \leq z \leq h_p)$:

$$\frac{u}{u_*} = \frac{1}{k}\left[\ln(\frac{z}{z_o}) - \Psi(\frac{z}{L})\right] \tag{2.7}$$

Ψ is a function of $\frac{z}{L}$. Businger *et.al.* (1971) and Kondo (1975) parameterizations are used.

2. EKMAN LAYER SOLUTION $(h_p \leq z \leq \infty)$

$$U = \cos\alpha + U_T\eta + \exp^{-\eta}[(\cos\eta - \sin\eta)\sin\alpha + V_T\cos\eta] + U_2 \tag{2.8}$$

$$V = \sin\alpha + V_T\eta - \exp^{-\eta}[(\cos\eta + \sin\eta)\sin\alpha + V_T\sin\eta] + V_2 \tag{2.9}$$

where,

$[U, V]$ = nondimensionalized winds $(\hat{U}/G, \hat{V}/G)$,

the non-dimensional geostrophic wind is,

$[U_g, V_g] = (\cos\alpha, \sin\alpha) + [U_T, V_T]\eta$,

the thermal wind is,

$[U_T, V_T] = g\delta[-T_y, T_x]/(fT_oG)$,

and,

$[U_2, V_2]$ = secondary flow modification to the Ekman mean flow solution,

$\eta = z/\delta$,

α = boundary layer turning angle (geostrophic departure angle),

δ = outer layer characteristic scale,

The subscripts x and y correspond to partial differentiation, g to geostrophic wind, T to thermal wind and 2 to secondary flow.

The surface layer solution is valid only near the surface while the Ekman solution holds from the top of the surface layer to the top of the boundary layer. The two solutions are patched with equal velocities, shear and K_e at $z = h_p$. Complete similarity equations incorporating thermal wind and secondary flow can be written:

$$\left[\frac{kG}{u_*}\right](\sin\alpha + \beta) = -B \tag{2.10}$$

$$\left[\frac{kG}{u_*}\right](\cos\alpha + \gamma) = -A' \tag{2.11}$$

where,

$$B = 1/(2\lambda_R)[1 - \lambda_R\Psi_\eta(h_l)], \tag{2.12}$$

$$A' = \Psi(h_l) + \ln(E\lambda_R) + B, \tag{2.13}$$

$$\beta = \frac{1}{2}(V_T - U_T) + \frac{1}{2}(V_{2_\eta} - U_{2_\eta})_{\lambda_R}, \tag{2.14}$$

$$\gamma = \frac{1}{2}(V_T + U_T) + \frac{1}{2}(V_{2_\eta} + U_{2_\eta})_{\lambda_R}, \tag{2.15}$$

$$\delta = 2k\lambda_R u_*/[f(1 - \lambda_R\,\eta(h_l)], \tag{2.16}$$

$$h_l = (\lambda_R \delta)/L, \tag{2.17}$$

$$E = \delta/z_o \tag{2.18}$$

The subscript η denotes partial differentiation and L is the Monin-Obukhov length. The resistance law is expressed as:

$$\frac{u_*}{G} = k\left[\frac{-\gamma A' - \beta B + \{B^2 + A'^2 - [\gamma B - \beta A']^2\}^{1/2}}{B^2 + A'^2}\right] \tag{2.19}$$

Based on Brown (1978), $\lambda_R \approx .15$ and from Brown (1970, 1972), $U_{2_\eta} \approx V_{2_\eta} \approx 0.1$.

The computational method is a triple nested iteration scheme with the initial tolerance set at 0.1% (i.e. the difference between the guessed value and the actual value at the patch height must be 0.1% or less). At each grid point, the innermost loop iterates on z_0 (roughness length) and the middle loop iterates on u_*/G (similarity function) while the outer loop iterates on z/L (stability) according to a model suggested by Liu *et al.* (1979) to account for humidity and molecular sub-layer effects. If the first iteration in any loop fails to converge, the tolerance is increased to 10%. If the second iteration fails to converge, the horizontal temperature gradient is cut in half, but the tolerances remain at 10%. If the thermal wind is strong enough it may overwhelm the secondary flow parameterization in which case it is assumed that no solution can be found and the model fails.

Brown (1970) found that secondary flow modification was maximum for neutral stratification and decreased slightly as stratification became unstable. No modification occured at low wind speeds. If there is a moderate thermal wind or an error in its calculation, large errors can arise in A and B for stratification less than moderately stable (Brown, 1982; Arya and Wyngaard, 1975; Yamada, 1976; Krishna, 1981). Non-steady state flow, sloping terrain or other horizontal inhomogeneities remain as possible contributing factors to observed scatter in A and B.

The only initialization field necessary for the model to run is sea level pressure ($MSLP$); however, surface air temperature, sea surface temperature (SST) and humidity can also be supplied to allow for calculations of heat fluxes and to incorporate thermal wind and stratification. Forcing fields and model parameters are detailed in Appendix B.

The model does not account for the up-gradient mean heat flux in the convectively driven ABL explicitly, but it is in line with simple approaches for the CABL as proposed by Wyngaard and Brost (1984) and applied to situations of a CAO by Chrobok *et al.* (1992). Furthermore, the model has been extensively checked against observations (Brown, 1978; Brown and Liu, 1982; Brown and Levy, 1986) and has been investigated as a boundary layer model in general circulation models (Brown and Foster, 1991; Foster and Brown, 1991, 1994a; Brown and Foster, 1994). Details of the model are presented in the next section.

2.5.3.1 Applications of the Brown Model

The Brown model has seen extensive verification and application in the last two and a half decades. It's first applications were by Brown (1978, 1981a) to data obtained from the Arctic Ice Dynamics Joint Experiment (AIDJEX). The experiment was run within an 800 km diameter circle of 6–10 buoys in the center of the Beaufort Sea. In the middle of the circle were four manned camps $\approx$ 100 km apart. The model was initialized by a 50 km grid of sea level pressures and then used to relate geostrophic flow from the large scale pressure field to the surface stress vector (u_*/G). Derived values of the similarity parameters A and B were compared with measured values and AIDJEX data with satisfactory results. The measurement of the similarity parameter λ_R was not resolvable by the AIDJEX data. Using a value of $\lambda_R = 0.15$ to predict u_*, U_{10} and α gave good agreement although it was determined that results were not sensitive to a 15%

error in λ_R. Brown (1981a) notes that the geostrophic/PBL model will work well only in well-determined, fairly uniform fields.

The model was tested on a larger scale by Brown and Liu (1982). Surface winds were determined from synoptic scale temperature and pressure fields and compared with surface measurements in GOASEX (Gulf of Alaska Experiment) and JASIN (Joint Air-Sea Interaction Experiment). Pressure values were obtained from National Weather Service (NWS) analyses (400 km resolution) and supplemented by local observations. An interpolated (20×20) pressure grid, with a square domain of 1000 km sides, was applied to the model. The overall accuracy of the model, based on the comparisons suggest that large-scale PBL winds derived from $MSLP$ and temperature compare to local average fields or point measurements within 2 ms^{-1} and 20°. It was noted that winds near regional maxima or minima or near fronts are smoothed out, and can be in error by 3 ms^{-1} and 30°.

An "inverse" version of the model has been employed by Brown and Levy (1986) to determine sea level pressure fields from satellite scatterometer derived surface winds. They extended the work further (Levy and Brown, 1991) by comparing Seasat-A Satellite Scatterometer (SASS) and Scanning Multi-Channel Microwave Radiometer (SMMR) data combined with the Brown PBL model, with Australian Bureau of Meteorology (ABM) conventional $MSLP$ and ECMWF pressure analyses. ABM sea level pressures were gridded onto a 47×47 polar stereographic grid mesh centered on the South Pole. This corresponds to a grid box resolution of $\approx$ 400 km. ECMWF latitude-longitude grid resolution was $\approx 1.12^{o}$. The Southern Hemisphere (SH) pressure gradients obtained by the PBL-scatterometer method are significantly stronger than those obtained by the weather services. It was suggested that remotely sensed data added to standard analysis techniques and satellite imagery can greatly enhance analysis and prognosis in remote oceanic regions and improve climatological flux estimates.

Recently Brown and Zeng (1994), used ERS-1 (Earth Resources Satellite) scatterometer data along with the inverse PBL model to estimate central pressures in 25 mid-latitude cyclones. When the geostrophic wind is known the pressure field can be obtained by solving Poisson's Equation with Von Neumann boundary conditions. A 50 km grid was used and the pressures were smoothed on a 100 km scale. The model domain was approximately 5^o longitude ($\approx$ 500 km) by 20^o latitude. Using the model scatterometer method, they found a 2 hPa lower average than in the ECMWF analyses.

The latest application of the model was in three papers by Brown and Foster (1994); Foster and Brown (1994a, 1994b). Oceanic surface winds and fluxes calculated with a modified version of the Brown two-layer similarity model were compared with those obtained by the NASA Goddard Laboratory for Atmospheres (GLA) GCM. The GLA GCM utilizes an advanced higher order closure (ADHOC) model incorporating a modified Mellor-Yamada level 2.5 turbulence model above the surface layer. The grid used in the comparison was $4^o \times 5^o$ resolution and data determined by a twelve day, seventeen $\sigma-$layer GCM integration were used. The model domain encompassed all oceanic grid points that were at least two grid points away from land and had a minimum latitude of 22^o. Northern and southern hemisphere cases were combined. It was found that the Brown model, when matching a homogeneous Ekman layer (no OLE) to the GLA logarithmic surface layer produced surface winds and fluxes comparable to a typical ADHOC model. Further study revealed that incorporating OLE into the similarity model effected a 5 to 20% increase in U_{10} and fluxes of heat and momentum. OLE circulations are not parameterized in any current GCMs due to inadequate grid resolution. It was further concluded that differences in viscous sub layer, surface layer and thermal wind parameterizations lead to significantly different surface winds and fluxes.

Chapter 3

Study Area and Analysis Methods

3.1 Storm Transfer and Response Experiment (STREX)

The primary goal of STREX was to gain understanding of lower MABL processes during frontogenesis and frontolysis. The field phase ran from 1 November to 15 December, 1980. A total of 10 independent missions were executed using a large suite of observing platforms including: 3 research ships, 6 aircraft, 23 drifting buoys, anchored buoys, satellites, merchant ships and others. A comprehensive review of the STREX field program and its observation systems can be found in either Fleagle *et al.* (1982) or the STREX field phase report (Miyake and Recker, 1980).

The 45 day endeavour resulted in the collection of one of the most comprehensive data sets describing the structure of both the upper ocean and the storms in the north Pacific. This study investigates data collected during mission #6, the specific purpose of which was to explore the lower MABL and subsequent air-sea interactions during a CAO. None of the other missions shared this objective.

3.2 Mission #6 Description

STREX mission #6 was executed on 2 Dec 1980 in the Northeast Pacific Ocean. The study area (shown in Figure 3.1) encompassed a region approximately 1500 km E-W by 500 km N-S just west of the Queen Charlotte (Graham and Moresby) Islands. The primary data collection platform, a NOAA P-3 aircraft collected approximately 9 hours

(1713Z Dec 2 – 0200Z Dec 3) of 1-sec flight level averages of position, radar and geopotential altitude, pressure, temperature, dewpoint, relative humidity and both components of the horizontal wind. Two Omega dropwindsondes were deployed, one each at the beginning and end of the flight, giving horizontal winds, temperature and humidity profiles. The P-3 also flew a descent profile and ascent profile as it entered and left the boundary layer sampling region respectively. Additional profile data were supplied by radiosonde releases at station P′ by the USS Oceanographer, station P by the CCGS Vancouver and at the primary meteorological observation site Port Hardy (YZT). A WC-130 Hercules aircraft flew an 8 hour synoptic pattern during which time 7 Omega dropwindsondes were released. In previous and later missions this pattern was used to sample the atmosphere both pre- and post-frontally. During mission #6 the WC-130 provided useful boundary layer profiles which complemented the P-3 data and supplied further information on the region to the west of the P-3 sampling region.

3.3 Data Processing

The NOAA P-3 flight level data used in this study were 20-sec centered averages computed from the original 1-sec averages. Air temperatures were converted to virtual temperatures using the method outlined in Wallace and Hobbs (1977, pg. 52). Virtual temperatures were converted to virtual potential temperature using Poisson's Equation. Relative humidity was converted to specific humidity using known relationships between specific humidity, vapour pressure and relative humidity. Virtual temperature, virtual potential temperature, specific humidity, dew point temperature, along- and cross-winds, and pressure were then allocated to 5 heights, namely: 50, 90, 150, 240 and 315 metres. The bin ranges were as follows: 50 m (35-65 m), 90 m (65-115 m), 150 m (115-190

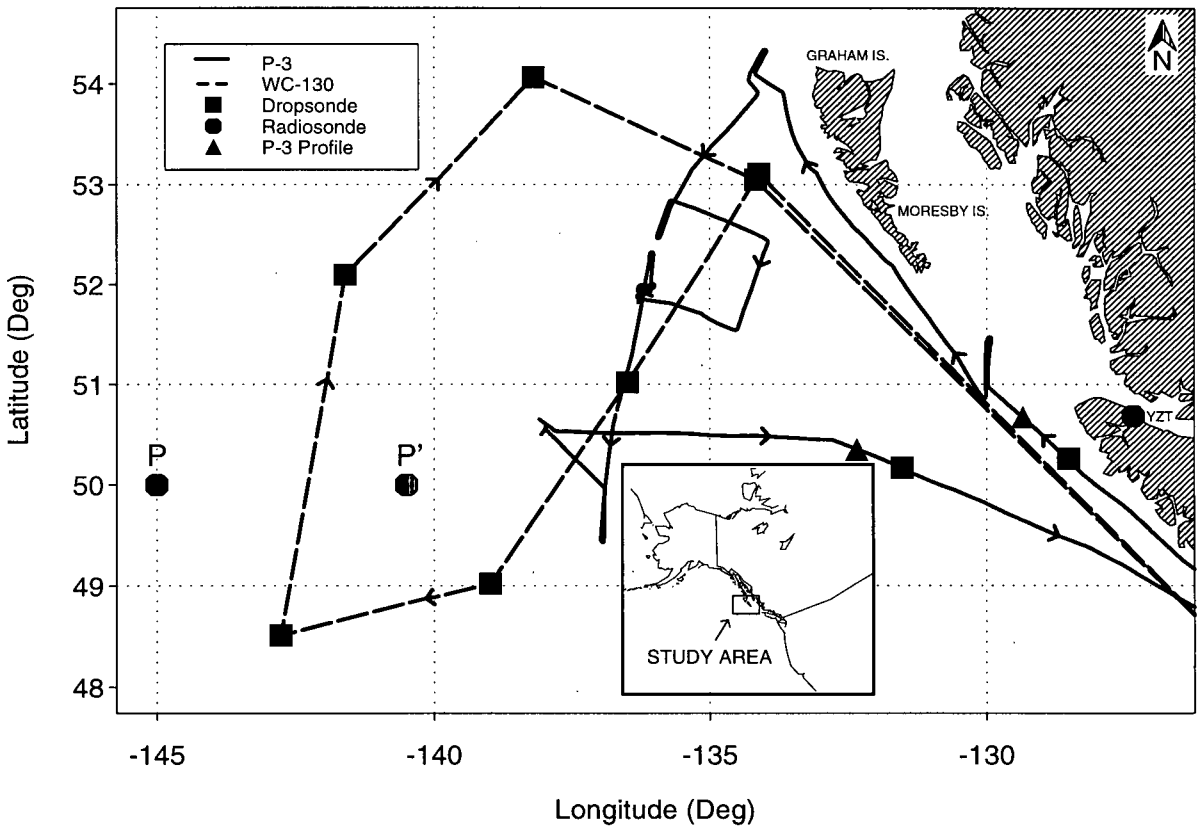

Figure 3.1: STREX mission #6 study region and flight paths of both the NOAA P-3 and the WC-130 Hercules aircraft. Also shown are the locations of dropsonde releases and upper air stations (Port Hardy–YZT, CCGS Vancouver–P and USS Oceanographer–P′).

m), 240 m (190-285 m), 315 m (285-400 m). The only variable that was corrected during this allocation procedure was pressure using the hydrostatic relation. The largest height adjustment in the highest level used (150 m) was 40 metres, corresponding to a temperature correction of .40°C for neutral stability. Temperature adjustments due to adiabatic processes were assumed small enough to be neglected. The moisture variables were not corrected due to the lack of a known relationship between moisture and the vertical coordinate. The error should be small since the specific humidity would not change significantly over a maximum vertical distance of 40 metres. Winds were also left unadjusted. Upon investigating the binned data, the two highest levels (240 m and 315 m) were eliminated from the analysis due to insufficient data in the height ranges corresponding to those levels.

The NOAA P-3 also obtained 48 records of 40 Hz turbulence statistics from fast response on-board instrumentation: a small bead thermistor for temperature, a microwave refractometer cavity for humidity and a gust probe for velocity (see Chou, 1993; Greenhut and Gilmer, 1985, for complete details). The instrumentation was used to obtain averaged estimates of the mean and perturbations of water vapor density, air temperature, surface temperature and the three wind components. The perturbations were used to calculate the alongwind stress component (τ_x) and the sensible (Q_H) and latent (Q_E) heat fluxes. Record lengths ranged from 118 seconds to 592 seconds with an average of 243 seconds. Using the average aircraft speed (104 ms^{-1}), these values translate to 12.2 km, 61.6 km and 25.3 km respectively. For path lengths of 20 km or longer, the calculated fluxes should be steady and relatively uncorrelated with flight leg length (e.g. Reinking, 1980; Greenhut, 1981; Walter *et al.*, 1984). 20 km corresponds to a record length of 192 seconds or longer. 17 of the records were shorter than this cutoff. A number of criteria were used to determine the validity of any one point. During some legs snow rendered SST measurements inconclusive and may have contaminated the humidity sensor. Other

points were obtained at heights above what would be considered reasonable for surface layer measurements. Also, if flux values appeared to be extraneously large or small (based on a scatterplot) the associated point was ignored. Of the original 48 records, 36 were retained for analysis. The resulting data point distribution is shown in Figure 3.2.

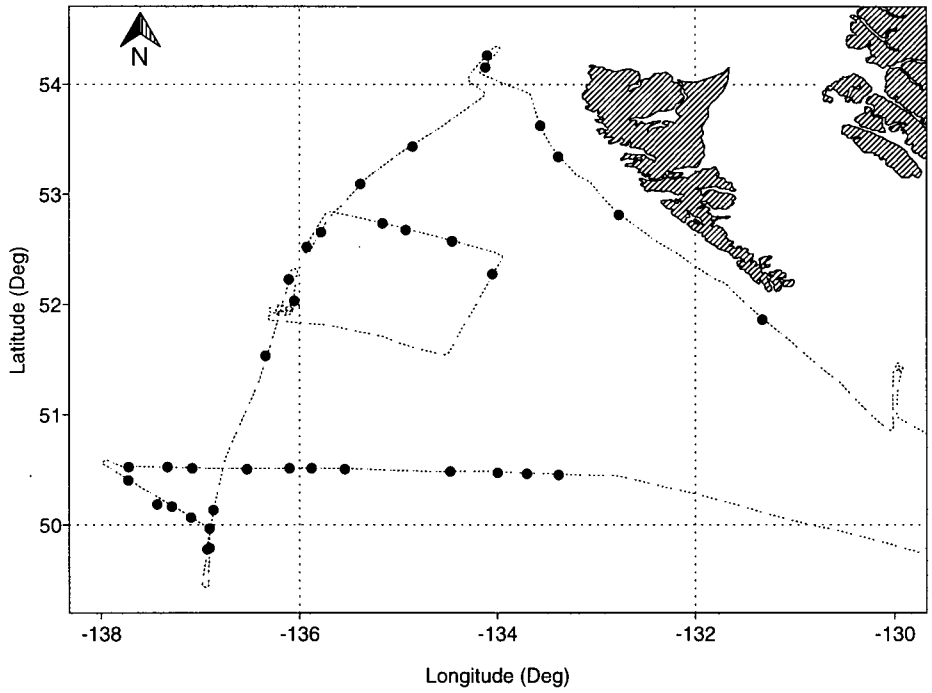

Figure 3.2: Turbulence data point distribution. Locations are delineated by solid dots and P-3 flight path is indicated by a dashed line.

The remaining data were obtained from radio- or drop-sonde profiles. The two P-3 dropsondes recorded pressure (hPa), height (m), temperature (°C), wet bulb depression (°C), wind speed (ms^{-1}) and direction (°). The 7 WC-130 dropsondes provided the same information as did two of the three radiosonde stations (P and P′). Port Hardy recorded relative humidity instead of wet bulb depression. During the mission #6 intensive observation period (18Z 2 Dec – 0Z 3Dec) radiosondes were released at 3 hour intervals from

station P′ while at station P, sondes were deployed every 6 hours and at Port Hardy, every 12 hours. Missing temperature profile values were estimated by linear interpolation. The primary use of the temperature profiles was to obtain estimates of boundary layer height based on the location of a capping inversion. A small error would be introduced if an inversion in the temperature profile existed where values were being interpolated. The interpolation could mask the true location of the inversion base. Estimates of boundary layer height in those cases should therefore be accompanied by a 5% uncertainty. It was also desirable to obtain virtual potential temperatures from the profiles. Potential temperatures were calculated using Poisson's equation. To compensate for moisture a number of relationships between dew point temperature and vapor pressure were employed. Dew point temperature was calculated from dew point depression and air temperature. Then, based on the equation $e(T) = e_s(T_d)$, ambient vapor pressures were computed using an approximated form of the Clausius-Clapeyron equation (Wallace and Hobbs, 1977, pg. 95). Specific humidities were then easily determined using $q \approx 0.622(\frac{e(T)}{P})$ where P is pressure.

Two significant problems that plagued the analysis were data paucity and irregular data point spacing. The former cannot be eliminated, but interpolation serves as a feasible tool to bring spatial regularity to data. Using an objective analysis scheme based on LeTraon (1990) (see Appendix A) the variables were interpolated onto 40×40 rectangular grids and plotted for each of the three levels. Grid edges were defined by the minimum and maximum latitude and longitude values for N-S and E-W grid sides respectively. The grid boundaries varied between the different levels, corresponding to an interpolated spatial resolution of 9x10 km at level 1 and 13x13 km at both levels 2 and 3. Consequently the plotting domain for level 1 is significantly smaller than the domain for levels 2 and 3. The resolution estimates are based on the distance spanned by 1 degree of longitude at 51.5° N latitude. The E-W resolution would increase or decrease to the

North and South respectively but not significantly enough to negate the Cartesian grid assumption.

3.4 Interpolation Validation

Interpolated pressure fields were plotted and compared with two references to test the interpolation method's ability to produce realistic results. The references were National Meteorological Center (NMC) output presented in the synoptic analysis and Atmospheric Environment Service (AES) surface analyses. The pressure plots at all three levels were found to closely emulate both of the reference sources. It is therefore assumed that plots of temperature, humidity and wind at any given level are representative of the mean horizontal MABL structure.

3.5 Measurement Errors

Wind speed and direction were computed from the Omega aided inertial navigation system true air speed and aircraft heading. During each flight leg there were no significant turns made and therefore wind speeds are accurate to $\pm$ 1 ms^{-1}. This is a median absolute error based upon tower flybys and accumulated positive errors over a flight (see Merceret, 1983). It assumes in-flight calibration to remove heading dependent errors and no serious errors in Omega updating during the flight. Air temperature was measured by a platinum resistance thermometer corrected for compressibility and exposure effects with an accuracy of $\pm$ 0.2°C. Very wet environments would likely increase the uncertainty. Dew point temperature was measured by a platinum resistance thermometer embedded in a thermoelectrically cooled mirror. The mirror temperature was automatically adjusted until dew formed on its surface. This temperature was measured to an accuracy of $\pm$ 1°C. A radar altimeter measured the radar altitude with an associated uncertainty of $\pm$ 3 m.

Sea surface temperature (SST) was measured by a downward looking Barnes precision radiation thermometer (PRT-5), an infrared radiometer with a window of 9.5-11.5 μm. The measurement error was $\pm$ 2°C or up to $\pm$ 10°C when there were clouds in the optical path between the radiometer and the sea surface. A further source of error is introduced during cloudy conditions, since the PRT-5 also records sky reflectance from the sea surface (Overland and Wilson, 1984). According to Overland and Wilson (1984) the SST time series they used required corrections based on comparisons with Airborne Expendable Bathythermograph (AXBT) measurements. There were also a number of cold spikes which correlated well with passages through rain squalls. The SST data obtained in this study were averaged over a larger number of samples and it is assumed that any spikes were smoothed out by the averaging. Errors in sonde data are unknown. Further error calculations were done using characteristic values and the functional relationships between variables (see Young, 1962, for method). Table 3.1 provides a list of all the observational variables collected by the P-3 aircraft instrumentation for which there was a determinable uncertainty plus error estimates for quantities that were calculated using the measured variables.

3.6 Stationarity and Diurnal Variation

An inherent assumption in the forthcoming analysis is the steady state of the 2 Dec CAO. Given that the total length of mission #6 was 9 hours and the synoptic time scale is 3 days, the amount of synoptic scale variation should be minimal. Using NMC 12 hourly $MSLP$ plots (shown in Section 4.2) a rough estimate was made of the time rate of change of pressure during mission #6. Between 12Z 2 Dec and 0Z 3 Dec $\frac{\delta MSLP}{\delta t} \approx 1$ hPa hr^{-1} while between 0Z 3 Dec and 12Z 3 Dec $\frac{\delta MSLP}{\delta t} \approx 0.25$ hPa hr^{-1}. The value of $\frac{\delta MSLP}{\delta t}$ during mission #6 can therefore be assumed to be ≈ 0.6 hPa hr^{-1}. A value of

VARIABLE	UNCERTAINTY	CHAR. VALUE	UNITS
z	3	100	m
P	5.0×10^{-1}	985	hPa
SST	2	10	^{o}C
T	2.0×10^{-1}	270	K
T'	5.0×10^{-2}	2.0×10^{-1}	K
θ	1.0×10^{-1}	275	K
θ_v	3.0×10^{-1}	275	K
T_d	1	265	K
q	1.6×10^{-1}	1.5	$\mathrm{g\,kg^{-1}}$
ρ_v	2.0×10^{-1}	2	$\mathrm{g\,m^{-3}}$
ρ_v'	1.1×10^{-2}	5.0×10^{-1}	$\mathrm{g\,m^{-3}}$
$\lvert\vec{U}\rvert$	1	15	$\mathrm{ms^{-1}}$
u', v'	1.8×10^{-2}	1	$\mathrm{ms^{-1}}$
w'	5.8×10^{-2}	1.0×10^{-1}	$\mathrm{ms^{-1}}$
$\overline{w'T'}$	5.2×10^{-3}	4.4×10^{-2}	$\mathrm{ms^{-1}K^{-1}}$
$\overline{w'\rho_v'}$	1.4×10^{-2}	7.8×10^{-2}	$\mathrm{gm^{-2}s^{-1}}$
$\overline{w'u'}$	5.8×10^{-2}	-4.3×10^{-1}	$\mathrm{m^2s^{-2}}$
Q_H	10 ($\approx$ 15%)	60	$\mathrm{Wm^{-2}}$
Q_E	60 ($\approx$ 20%)	300	$\mathrm{Wm^{-2}}$
Q_T	70 ($\approx$ 20%)	360	$\mathrm{Wm^{-2}}$
τ	7.4×10^{-2} ($\approx$ 15%)	-4.8×10^{-1}	$\mathrm{kgm^{-2}s^{-1}}$
u_*	5.8×10^{-2}	6.3×10^{-1}	$\mathrm{ms^{-1}}$
L	120 ($\approx$ 20%)	-615	m
$\zeta = z/L$	7.6×10^{-2} ($\approx$ 20%)	-3.6×10^{-1}	m
$\zeta_i = z_i/L$	1.0 ($\approx$ 10%)	-10	m

Table 3.1: Table identifying the variables collected during mission #6 for which there were determinable errors. Each quantity is accompanied by an uncertainty a characteristic value and units. Previously undefined variables are: dew point temperature (T_d), water vapour density (ρ_v) and inversion base height (z_i).

0.1 $\mathrm{hPa\,hr^{-1}}$ or lower would best substantiate the stationarity assumption. Although the analysis will assume steady-state conditions, non-stationarity may be influencing both the pressure and temperature fields to some extent.

The assumption of stationarity is applied to the SST distribution for two reasons. The first rationale is based on the actual amount of oceanic cooling that takes place. The ocean's high heat capacity ($\approx$ 4200 $\mathrm{JK^{-1}kg^{-1}}$) implies the absolute amount of cooling is small compared to the larger scale SST distribution. Secondly, the amount of time over which observations were taken was short compared to the time necessary for a substantial change in SST due to evaporative or sensible cooling, to occur. A constant heat source(sink) of approximately 300 $\mathrm{Wm^{-2}}$ and a 100 meter oceanic mixed layer corresponds to approximately 15 days for the water to heat(cool) by 1°C. This calculation is based on an assumption of no lateral heat advection. In contrast a 1000 meter atmospheric boundary layer ($C_p \approx 1004$ $\mathrm{JK^{-1}kg^{-1}}$) subject to the same heat flux would take about one hour to heat or cool by 1°C.

The convection turnover timescale in the marine atmospheric boundary layer is approximately 25–30 minutes, corresponding to a spatial scale of 150 km (assuming an aircraft speed of 100 $\mathrm{ms^{-1}}$). The spatial distance between P-3 data points is $\approx$ 2 km. The data should therefore have been able to resolve steady state convective phenomena over $\approx$ 25–30 minute intervals corresponding to the collection of 75–90 data points. With the above limitations in mind it will be assumed that the 2 Dec 1980 CAO was in a steady state.

The modification of the MABL is also dependent upon both land surface processes which have considerable diurnal variability during the cloud conditions associated with a CAO, and ocean surface processes which have little diurnal variation. Grossman and Betts (1990) noted that the daytime heating of land would warm and possibly dry the MABL subcloud layer air while at night, radiational cooling would *cool* the air leaving

the coastal area. These widely varying initial conditions would most likely affect the rate at which the warmer ocean surface would warm and moisten the air flowing over it.

During mission #6 the aircraft flew from 9 am local to 6 pm local time (17z -02z) which encompasses less than half the entire diurnal cycle. Therefore diurnal variations can be considered small enough to be neglected. The assumption is strengthened by the fact that less direct solar heating of the surface occured as a result of continuous cloud cover. This moderating effect helped to reduce the amplitude of the diurnal cycle.

Note that the the southeast region of the study domain is one in which the collection time between any two data points could be as much as 8 hours. Should there be any non-stationary effects, they would manifest themselves most obviously in that region.

3.7 Air-Sea Energy Exchange

The driving mechanism for energy and mass exchange between air and sea is turbulence. Sensible heat warms the atmosphere locally by conduction through adjacent air and sea molecules. Heat is then carried throughout the ABL and to the free atmosphere by turbulent transport. Latent heat is held in water vapor when evaporation occurs at the sea surface. The vapor is distributed throughout the ABL by turbulent mixing and the atmosphere warms when the vapor condenses. The momentum flux expressed by the Reynold's stresses (τ_x, τ_y) is also transported by turbulent processes and contributes to dynamical processes within both the boundary layer and the free atmosphere.

Considerable effort has been devoted to measuring these fluxes (e.g. Chou, 1993). The eddy correlation method allows for the direct determination of fluxes of momentum, heat and moisture. Indirect flux calculation schemes include, bulk aerodynamic methods, inertial subrange dissipation and profile methods. In this study, fluxes were determined using both the eddy correlation and the bulk aerodynamic methods.

Eddy Correlation Method In the eddy correlation method turbulent fluxes τ, Q_H, and Q_E are formulated as:

$$\tau = -\rho\overline{w'u'} \tag{3.20}$$

$$Q_H = \rho C_p\overline{w'\theta'} \tag{3.21}$$

$$Q_E = L_v\overline{w'\rho_v'} \equiv \rho L_v\overline{w'q'} \tag{3.22}$$

where,

ρ = Air density.

C_p = Specific heat of air at constant pressure.

L_v = Latent heat of vaporization.

$\overline{w'u'}$ = mean covariance of vertical and along wind air speeds.

$\overline{w'\theta'}$ = mean covariance of vertical wind speed and potential temperature.

$\overline{w'\rho_v'}$ = mean covariance of vertical wind speed and water vapour density.

Following Chou (1993), the crosswind stress component is neglected since it should be negligible near the surface (Greenhut, 1981). The sensible heat flux at 50 m is about 95% that at the surface, with a slope of about $-1.1z/z_i$ in the clear boundary layer or subcloud layer. The latent heat flux at 50 m is generally within $\pm 2\%$ of that at the surface (Chou *et al.*, 1986).

Bulk Aerodynamic Method The bulk equations are:

$$\tau = \rho C_D(U_{10} - U_S)^2 \tag{3.23}$$

$$Q_H = \rho C_P C_H (U - U_S)(\theta_S - \theta_{10}) \tag{3.24}$$

$$Q_E = \rho L_v C_E (U - U_S)(q_S - q_{10}) \tag{3.25}$$

where,

ρ = air density.

C_P = Specific heat of air at constant pressure.

C_D = Drag coefficient at reference height (10 m).

C_H = Stanton number.

C_E = Dalton number.

L_v = Latent heat of vaporization.

U_{10} = Wind speed at reference height (10 m).

U_S = Wind speed at surface.

θ_{10} = Potential air temperature at reference height(10 m).

θ_S = Potential sea surface temperature.

q_{10} = Specific humidity at reference height (10 m).

q_S = Specific humidity at surface.

The mean q_S is usually taken as the saturation value at θ_S. To determine U_{10}, wind speeds from the aircraft data were adjusted to 10 m using the log relation (see Stewart, 1979) and incorporating a stability correction:

$$U_z = \frac{u_*}{k}(\ln \frac{z}{z_o} - \Psi(\frac{z}{L})) \tag{3.26}$$

where,

z = reference height (10 m),

u_* = friction velocity,

k = von Karman's constant,

$\Psi(\frac{z}{L})$ = Monin-Obukhov stability function.

Roughness height z_o was determined at each point by substituting observed U and u_* at each measured height into the log (neutral stability) relation and solving for the roughness parameter. The exchange coefficients, C_D, C_H and C_E are often assumed to be constant ($\approx 10^{-3}$), but in theory they depend on reference height, stability and surface roughness. In this study, the coefficients were calculated following Fleagle and Nuss (1985). Although the lower boundary layer is slightly unstable according to ζ values, there is sufficient evidence (Stull, 1988) to suggest that the variation in each of the exchange coefficients between neutral and unstable conditions is small enough to be considered negligible.

The neutral drag coefficient (C_{Dn}) was calculated using a wind dependent criteria:

$$C_{Dn} \times 10^{-3} = \begin{cases} 1.14 & \text{if } U < 10 \text{ ms}^{-1}, \\ 0.49 + 0.065\,\overline{U}_{10} & \text{if } U > 10 \text{ ms}^{-1} \end{cases} \tag{3.27}$$

The neutral Stanton number (C_{Hn}) was assigned the value 1.14×10^{-3} between the values suggested by Smith (1980) and Large and Pond (1982) and the neutral Dalton number (C_{En}) was approximated as 1.48×10^{-3} based on data reported by Friehe and Schmitt (1976). Fleagle and Nuss (1985) assigned standard deviations of 20% to 30% to the coefficients, representing the combined effects of observational errors and dependence of the fluxes on physical factors (e.g. OLE) not included in the bulk equations.

Chapter 4

Observational Results

4.1 Introduction

This chapter details the analysis of data obtained during STREX mission #6. Interpretation of results is carried out with respect for both data paucity and irregular data point distribution. A synoptic summary appears in the first section, followed by a section discussing both mean vertical and mean lower horizontal MABL structure during the 2 Dec, 1980 CAO. The next section presents a heuristic model comparison of bulk and eddy determined stability and surface heat fluxes followed by a discussion of the turbulence characteristics of the lower MABL in the X-Y plane. The last two sections present first a spectral analysis of the wind, temperature and moisture data and second some speculation on the boundary layer role of OLE during a cold air outbreak.

4.2 Synoptic Summary

Synoptic conditions at 12 hour intervals over the period 12Z 1 Dec 1980 to 12Z 3 Dec 1980 are discussed. This time span encompasses the mission #6 observation period and a twenty four hour period before and a twelve hour period after it. Figures 4.1 to 4.5 show surface pressure contours based on surface analyses from the National Meteorological Center (NMC). At 12Z 1 Dec, a strong elongated surface high (1046 hPa) stretched across the Yukon Territory (YUK.), British Columbia (B.C.) and Alberta (AB) with a NW-SE orientation. A steep NE-SW pressure gradient obtained over central B.C.

($\nabla P \approx 53 \times 10^{-3}$ hPa km^{-1}), while over the southern coastal zone, pressure gradients were weak ($\nabla P \approx 6 \times 10^{-3}$ hPa km^{-1}) and had a NW-SE orientation.

An arctic front defining the leading edge of the continental arctic (cA) air mass was situated over southern B.C. near the Canada (CA)/United States (U.S.) border. Over the next 24 hours a surface low pressure system (990 hPa) built off the Washington (WA) coast and by 0z 3 Dec (Figure 4.4) strong outflow winds had developed over the northern B.C. coastal zone. During the same period, the low deepened slightly and stalled over southwestern B.C. while the arctic high remained well defined and moved slightly northeast. Pressure gradients increased only slightly over interior B.C. ($\nabla P \approx 54 \times 10^{-3}$ hPa km^{-1}) but steepened considerably over the study area ($\nabla P \approx 25 \times 10^{-3}$ hPa km^{-1}). Each gradient maintained its respective NE-SW or NW-SE orientation. By the end of the synoptic observation period the surface low had begun to fill and the anticyclone was weakening. The arctic front remained stationary throughout the entire period due largely to an enduring upper level flow pattern.

Figures 4.6 to 4.6 depict 500 hPa height (m) contours. At 12z 1 Dec a substantial trough lay over most of B.C. and extended slightly over the ocean. Geostrophy implies predominantly north winds through Alaska (AK), the Yukon Territory and over the ocean. A high (5580 m in Figure 4.6) over the northwest portion of the Gulf of Alaska contributed to tighter packing of height contours and to stronger winds. The trough deepened over the next 36 hours and by 0z 3 Dec (Figure 4.9) a low center (5148 m) had formed between the Queen Charlotte Islands and Vancouver Island. Further strengthening of the flow occurred due to a repositioning by the high southeast towards the Queen Charlotte Islands. This upper level pattern remained in place for the entire observation period and when coupled with the surface flow, facilitated strong cold air advection from the central B.C. interior over the ocean and through the STREX study area (see Figure 3.1).

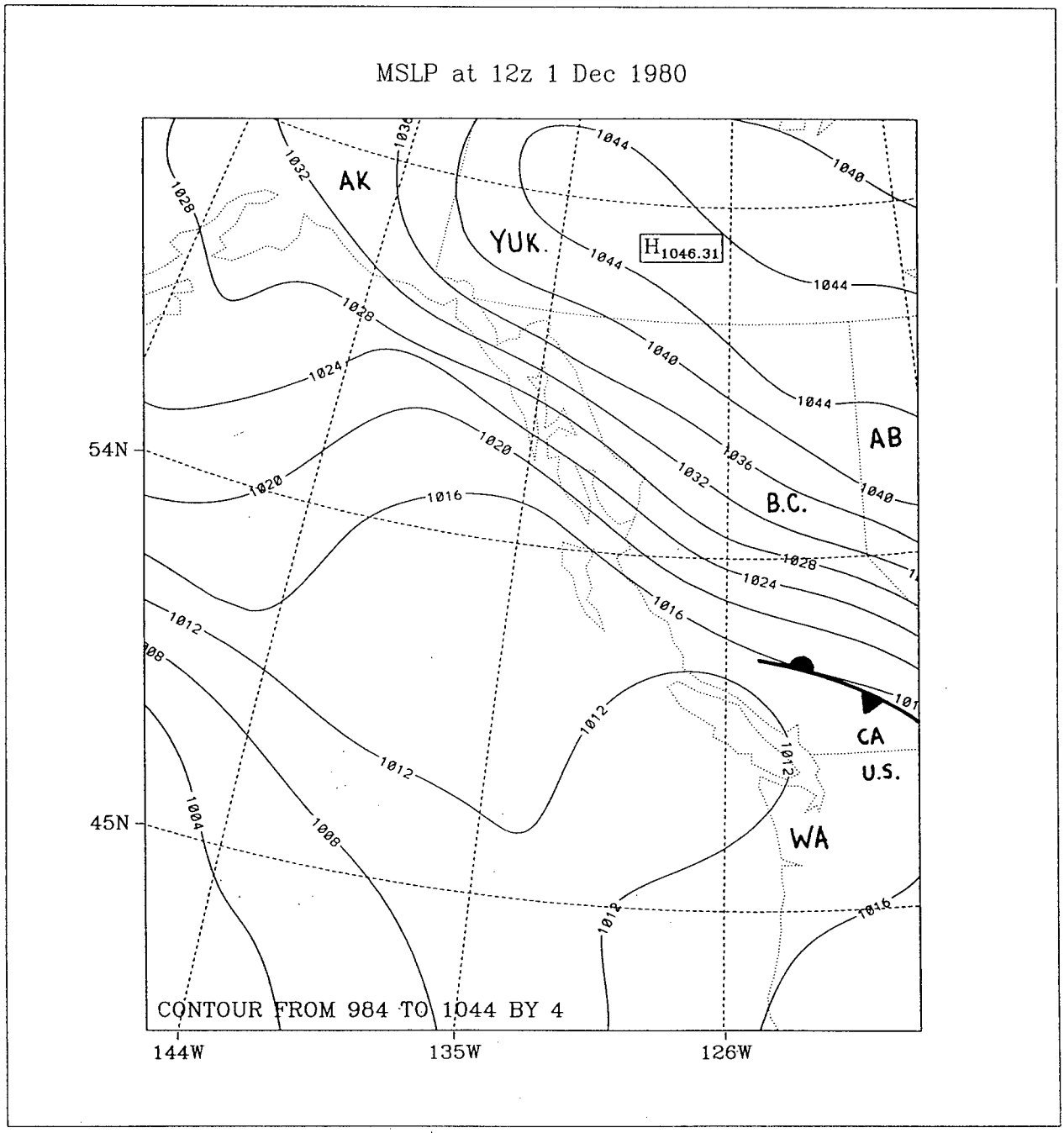

Figure 4.1: Mean sea level pressure (hPa) contours at 12z 1 Dec 1980. Contour interval is 4 hPa. Surface fronts are indicated by conventional symbols.

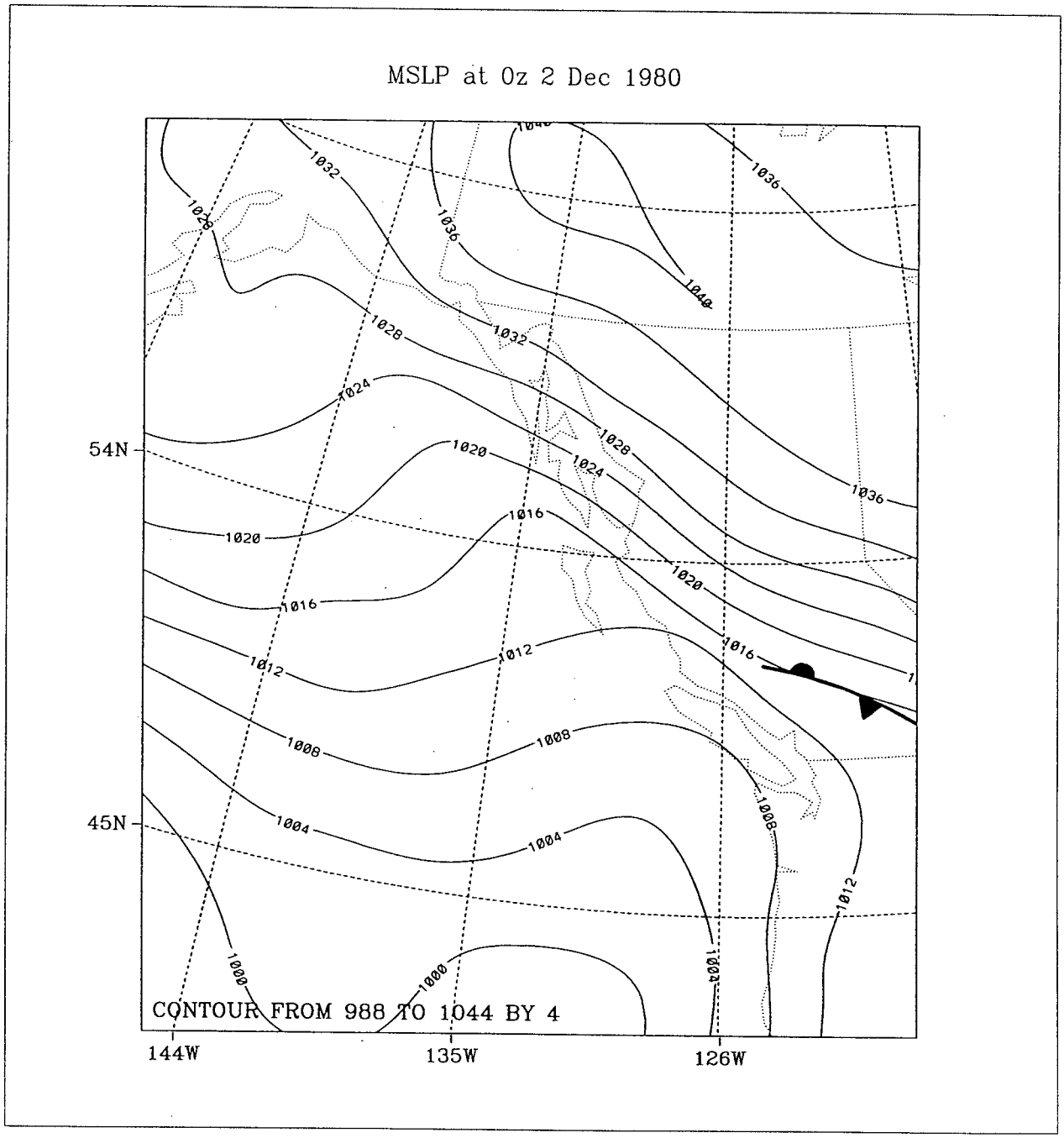

Figure 4.2: As in Figure 4.1 but at 0z 2 Dec 1980.

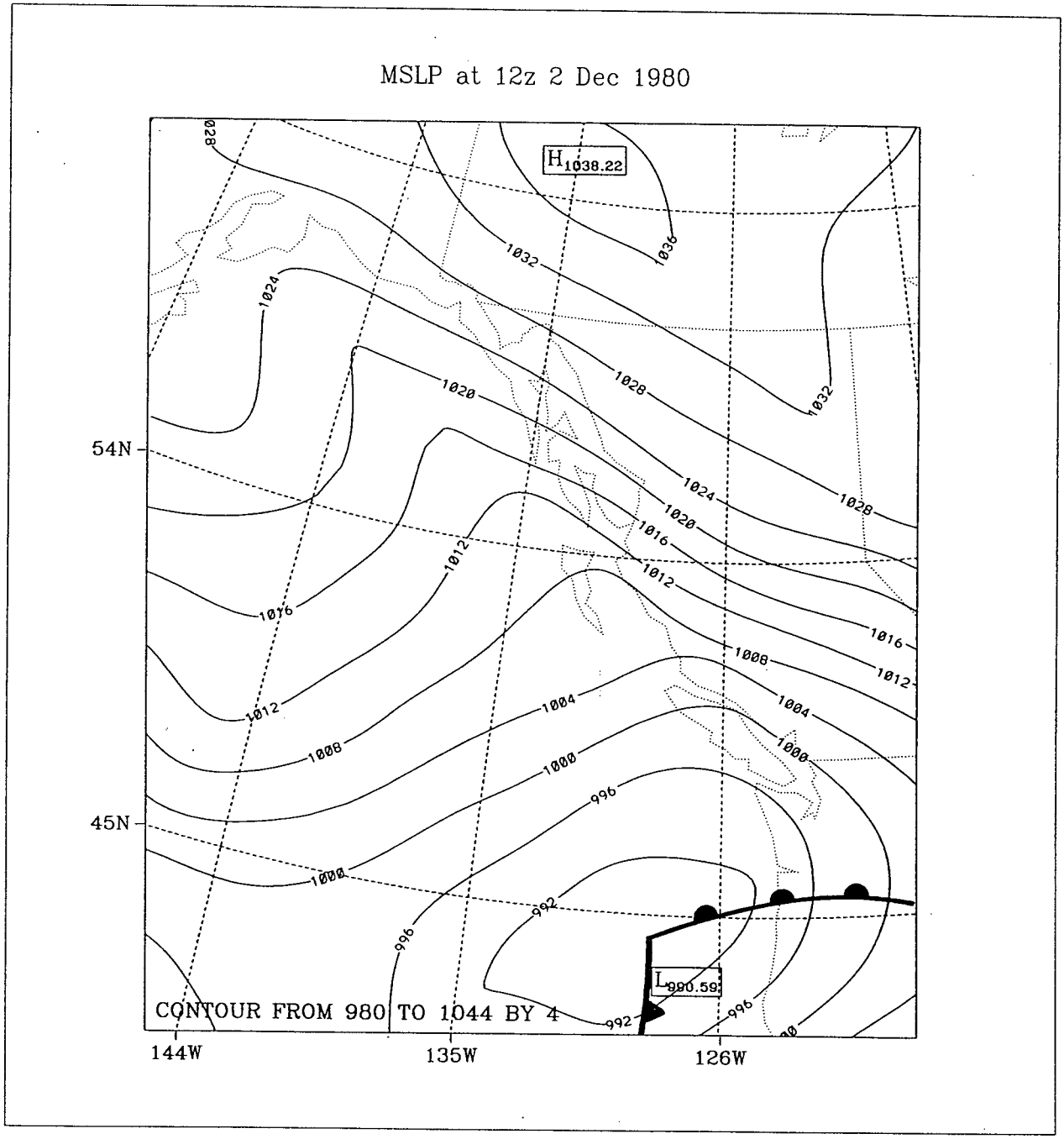

Figure 4.3: As in Figure 4.1 but at 12z 2 Dec 1980.

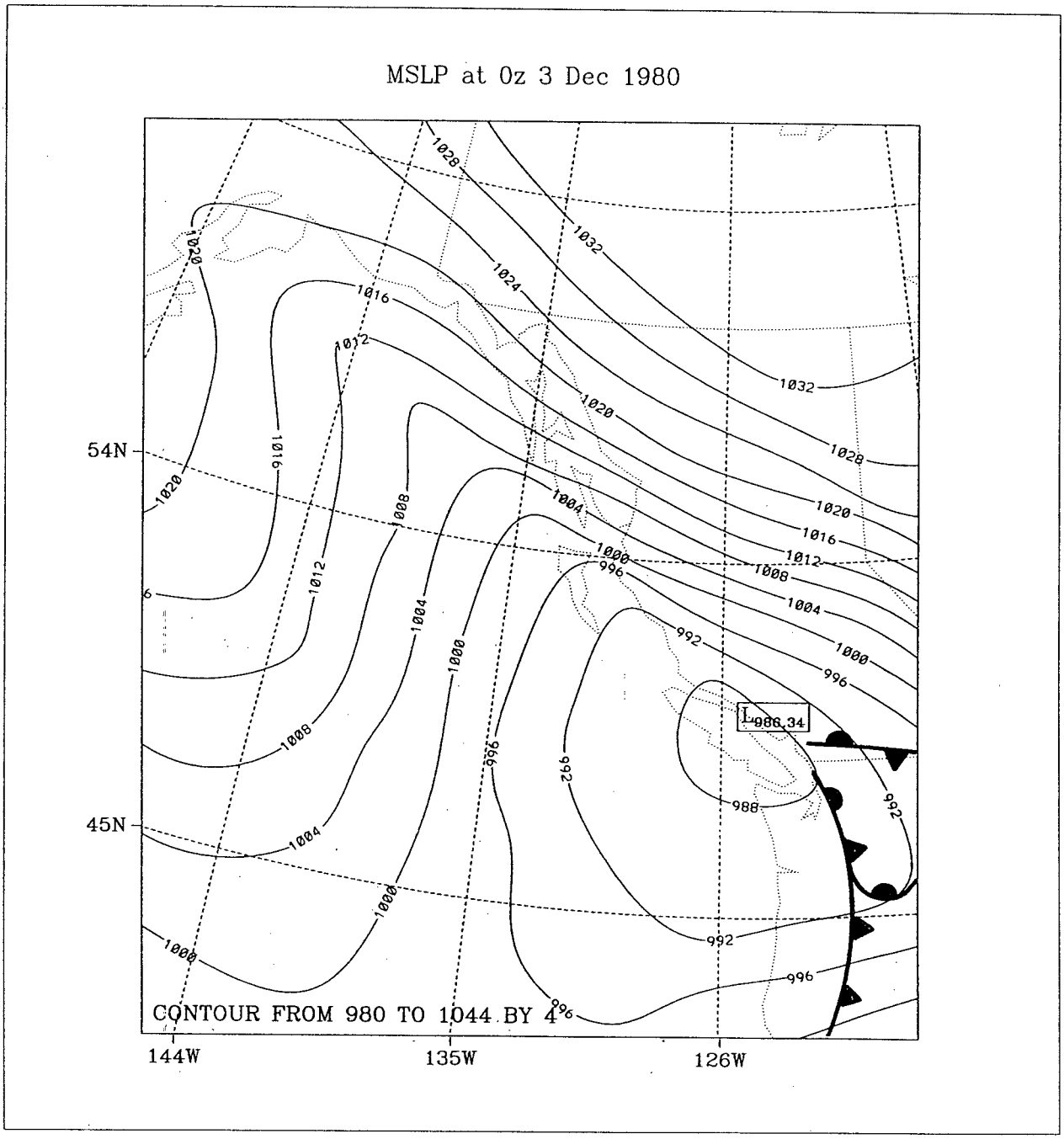

Figure 4.4: As in Figure 4.1 but at 0z 3 Dec 1980.

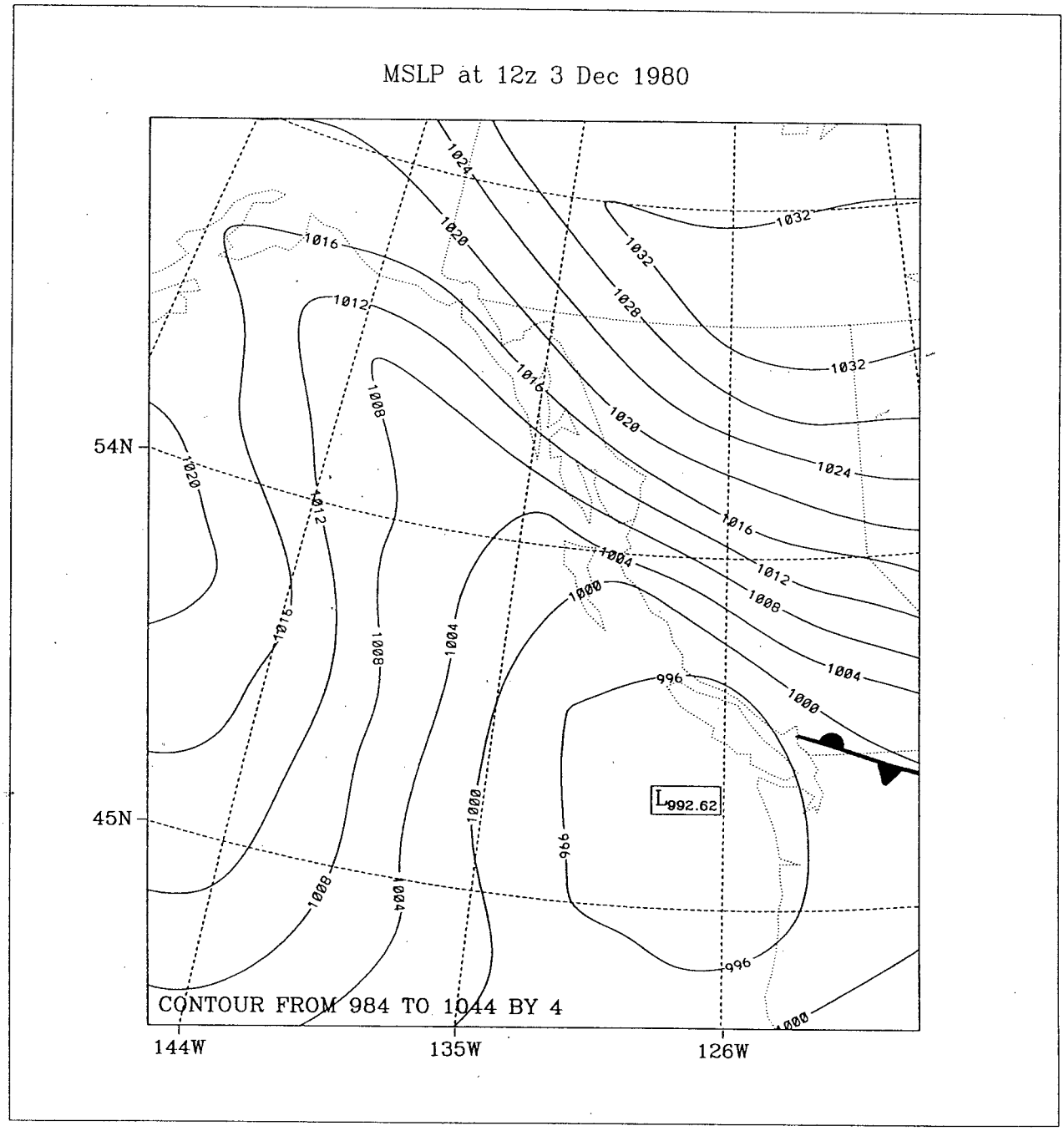

Figure 4.5: As in Figure 4.1 but at 12z 3 Dec 1980.

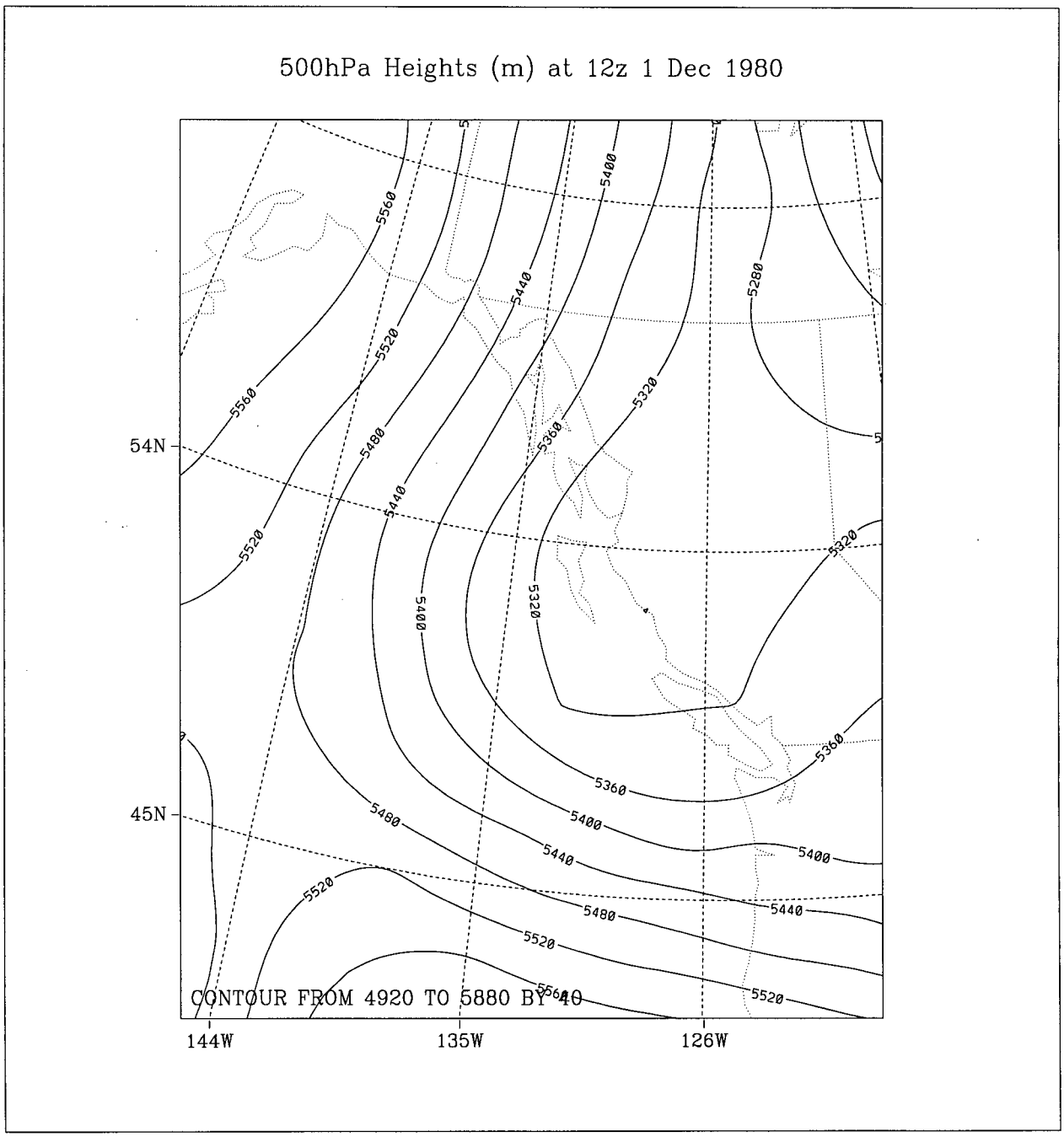

Figure 4.6: 500 hPa height (m) contours at 12z 1 Dec 1980. Contour interval is 40 m.

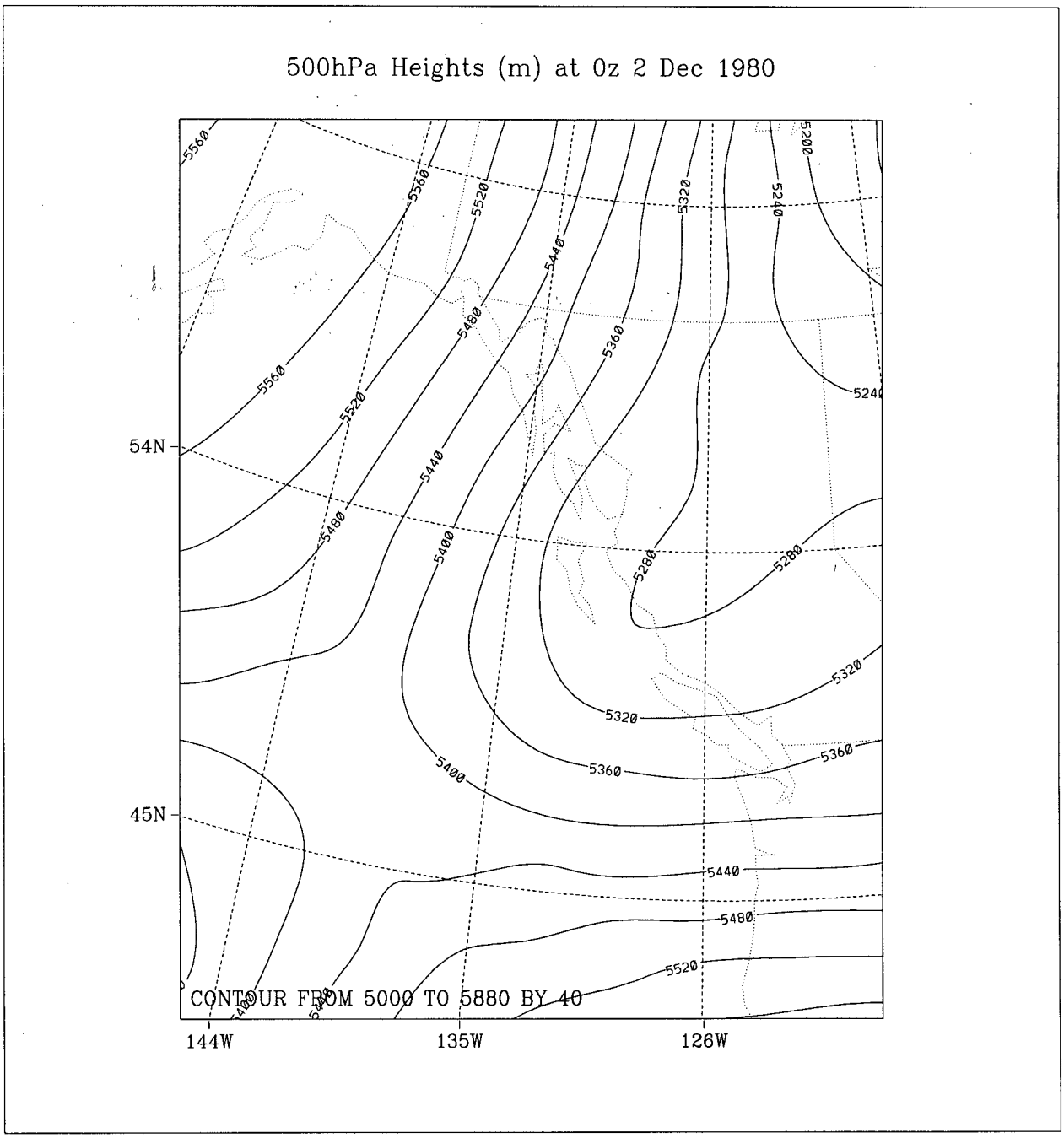

Figure 4.7: As in Figure 4.6 but at 0z 2 Dec 1980.

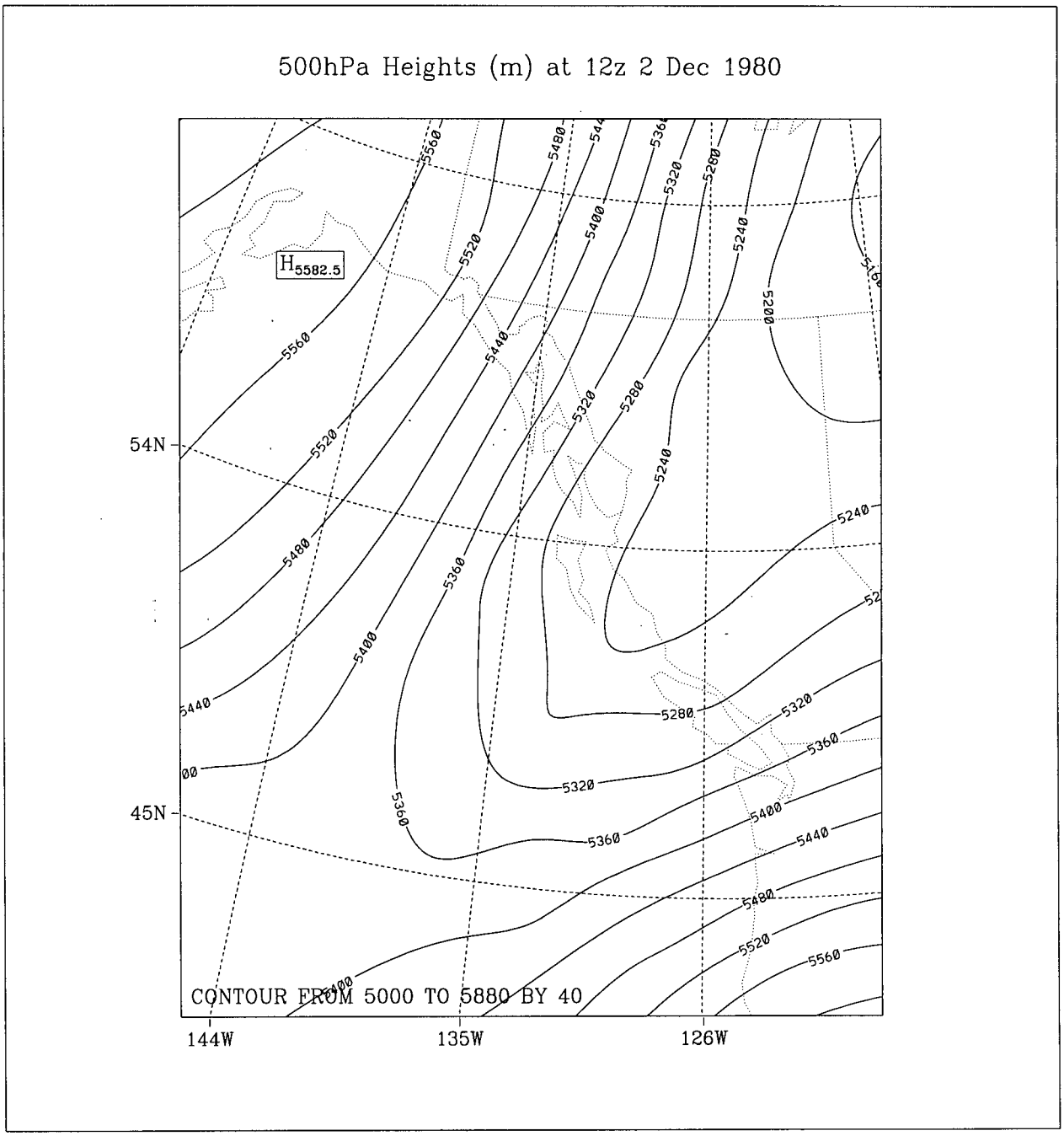

Figure 4.8: As in Figure 4.6 but at 12z 2 Dec 1980.

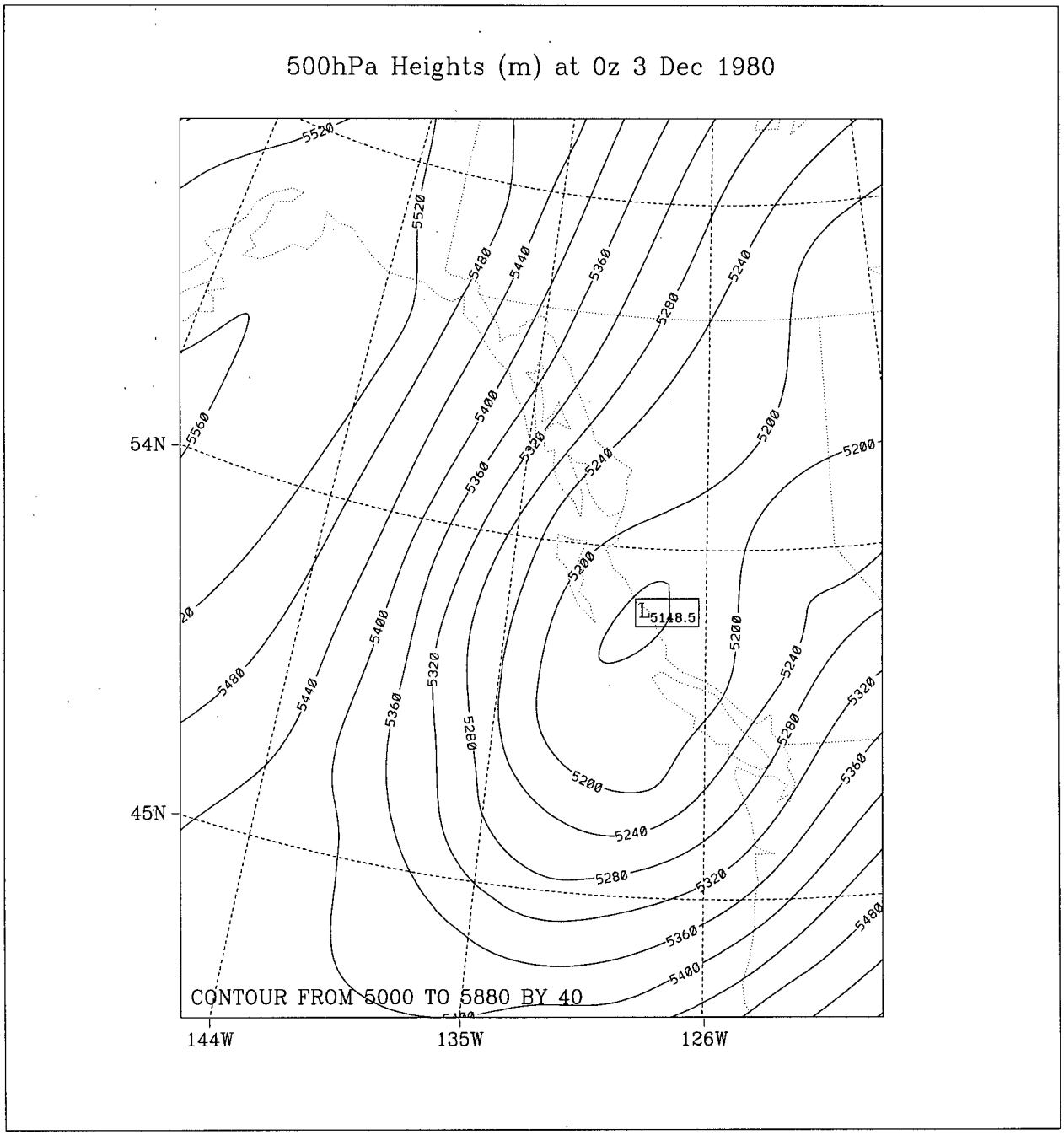

Figure 4.9: As in Figure 4.6 but at 0z 3 Dec 1980.

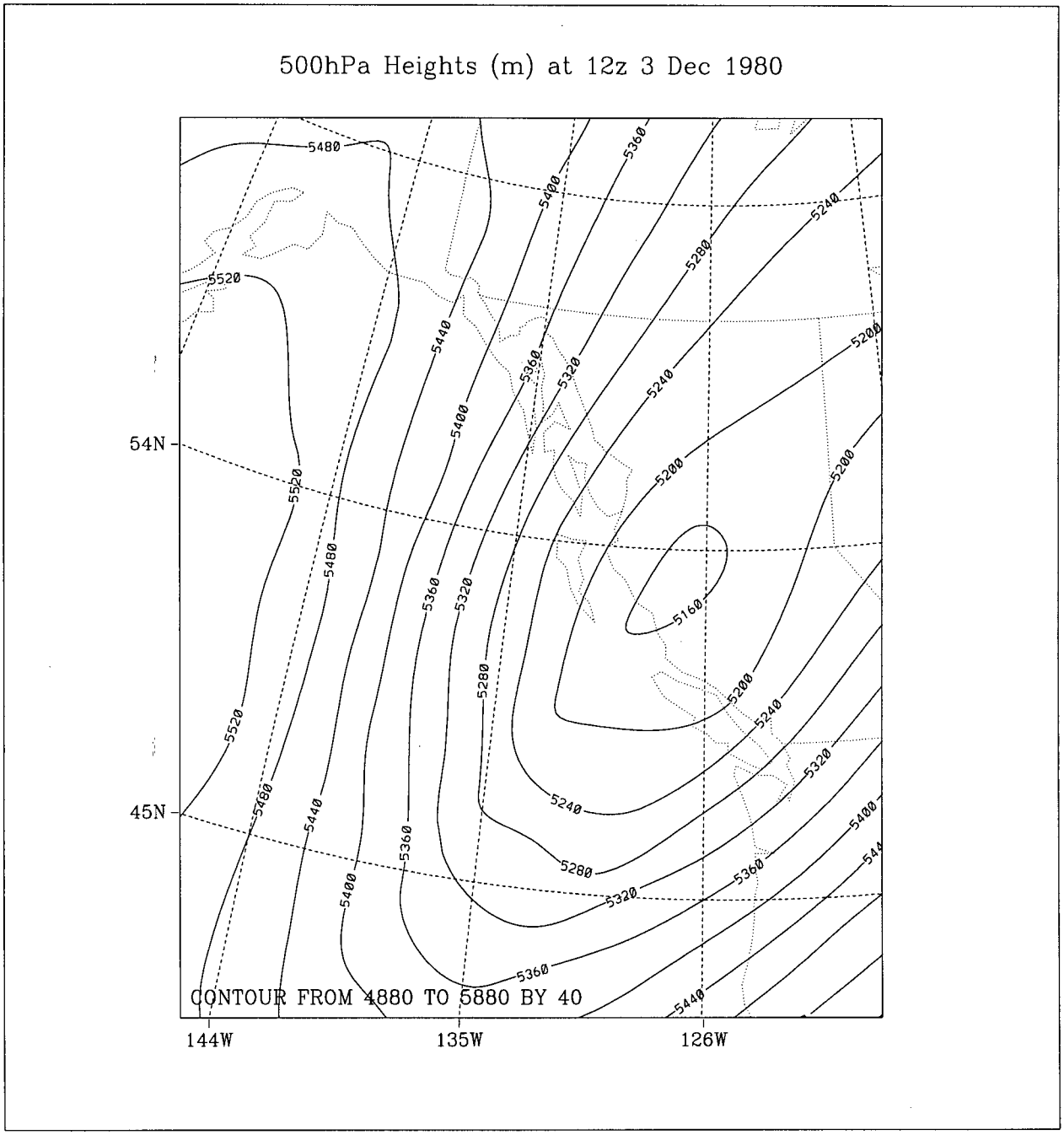

Figure 4.10: As in Figure 4.6 but at 12z 3 Dec 1980.

Temperature advection at any level can be inferred from superimposed contour plots of temperature and height. The 850 hPa level was used since the required data were most readily available at that pressure. Mean spatial characteristics at 850 hPa are assumed to be analogous to those at the surface. Figures 4.11 to 4.15 show 850 hPa temperature contours superimposed over 850 hPa height contours. Strongest advection corresponds to locations where large temperature gradients coincide with large height gradients.

Based on the map series 4.11 to 4.15, the strongest temperature advection over the study area occurred at 0Z 3 Dec (Figure 4.14) which coincides with the time period of mission #6 aircraft flights. The strongest temperature advection should also correspond to the most intense air-sea energy exchange. Bane and Osgood (1989) define an intense CAO as one in which the 850 hPa temperature is -15 °C or lower. 850 hPa temperatures in the mission #6 CAO ranged from -6 °C to -10 °C over the period 12z 1 Dec to 12z 3 Dec.

4.3 Results

4.3.1 Mean Vertical MABL Structure

Mean vertical MABL structure was investigated using profiles obtained both from radiosonde stations and from dropsondes deployed by the P-3 and WC-130 aircraft. Vertical temperature, moisture and wind characteristics are presented in the next three sections.

4.3.1.1 Temperature

Profiles of virtual potential temperature are shown in Figure 4.16. A capping inversion can be seen in all of the profiles except P3B and YZT. Evidence of a capping inversion is more clearly evidenced in the gradient ($\partial\theta_v/\partial z$) profiles (Figure 4.17). With the exception of the P3B and YZT profiles, there is a distinct jump in each profile. Temperatures

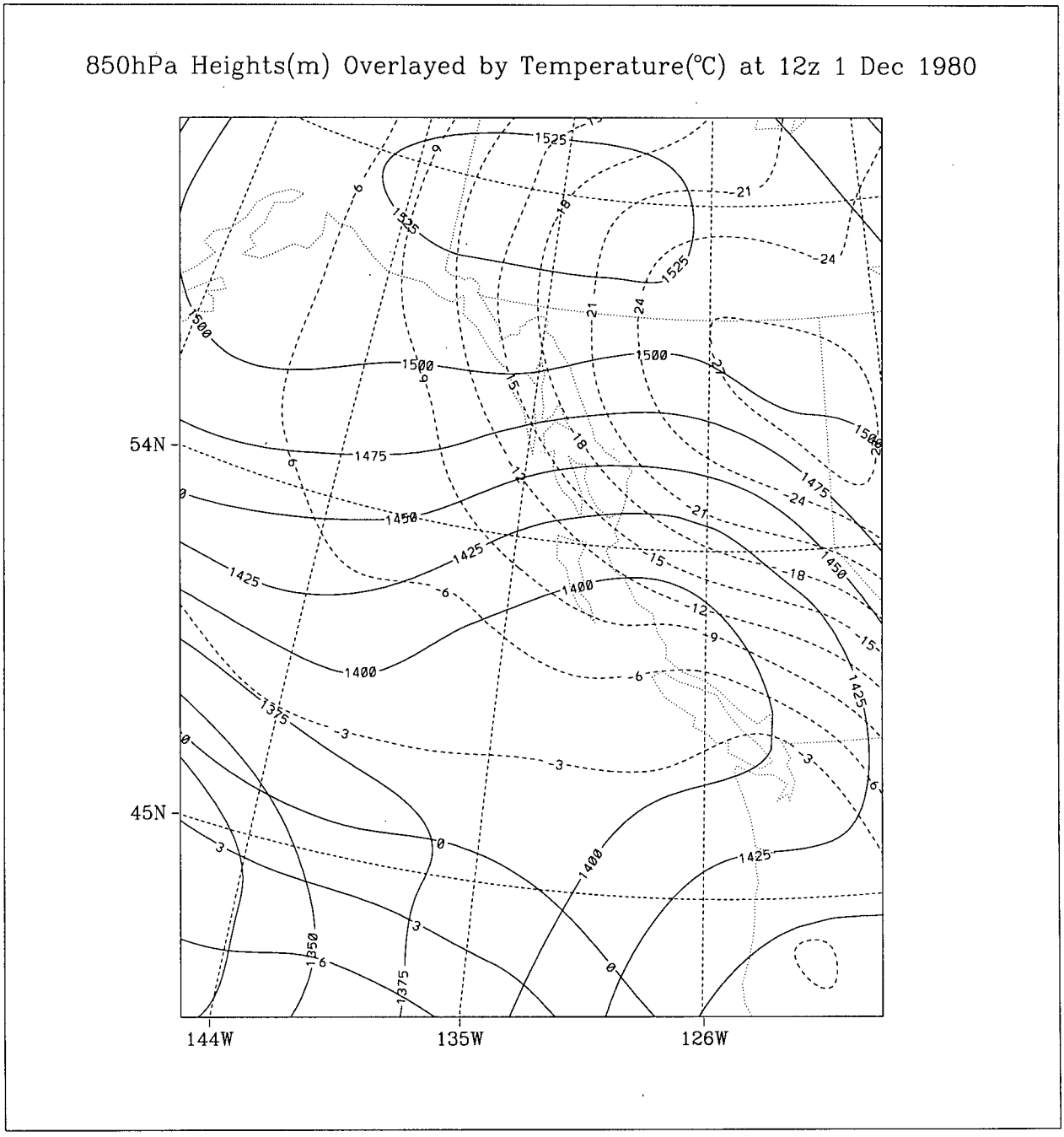

Figure 4.11: Figure from which 850 hPa temperature advection may be inferred over the STREX mission #6 study region at 12z 1 Dec 1980. Negative temperature (°C) contours are dashed, while zero and higher contours are solid. Height (m) contours are solid. Contour intervals are 3°C and 25 m.

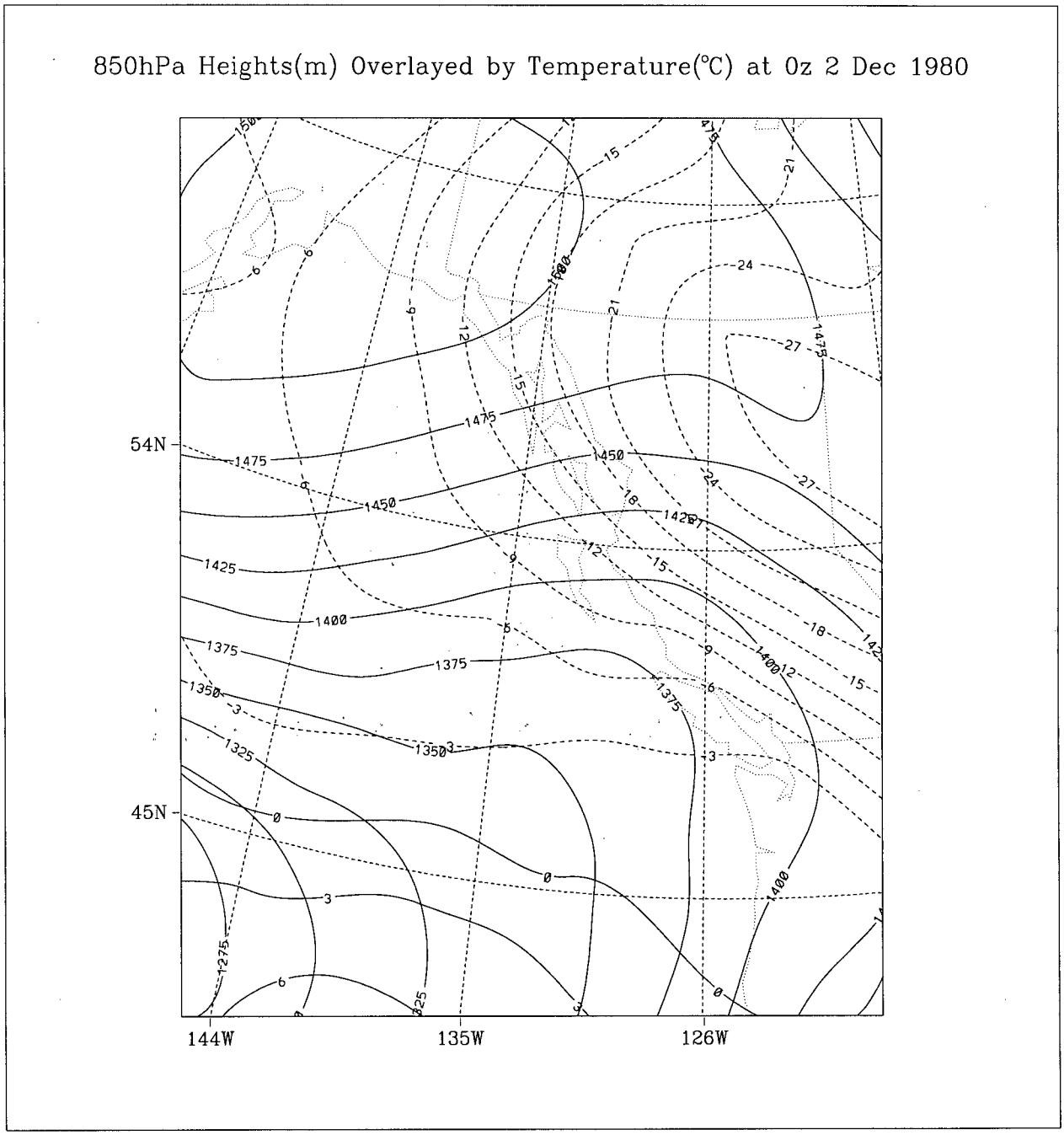

Figure 4.12: As in Figure 4.11 but at 0z 2 Dec 1980.

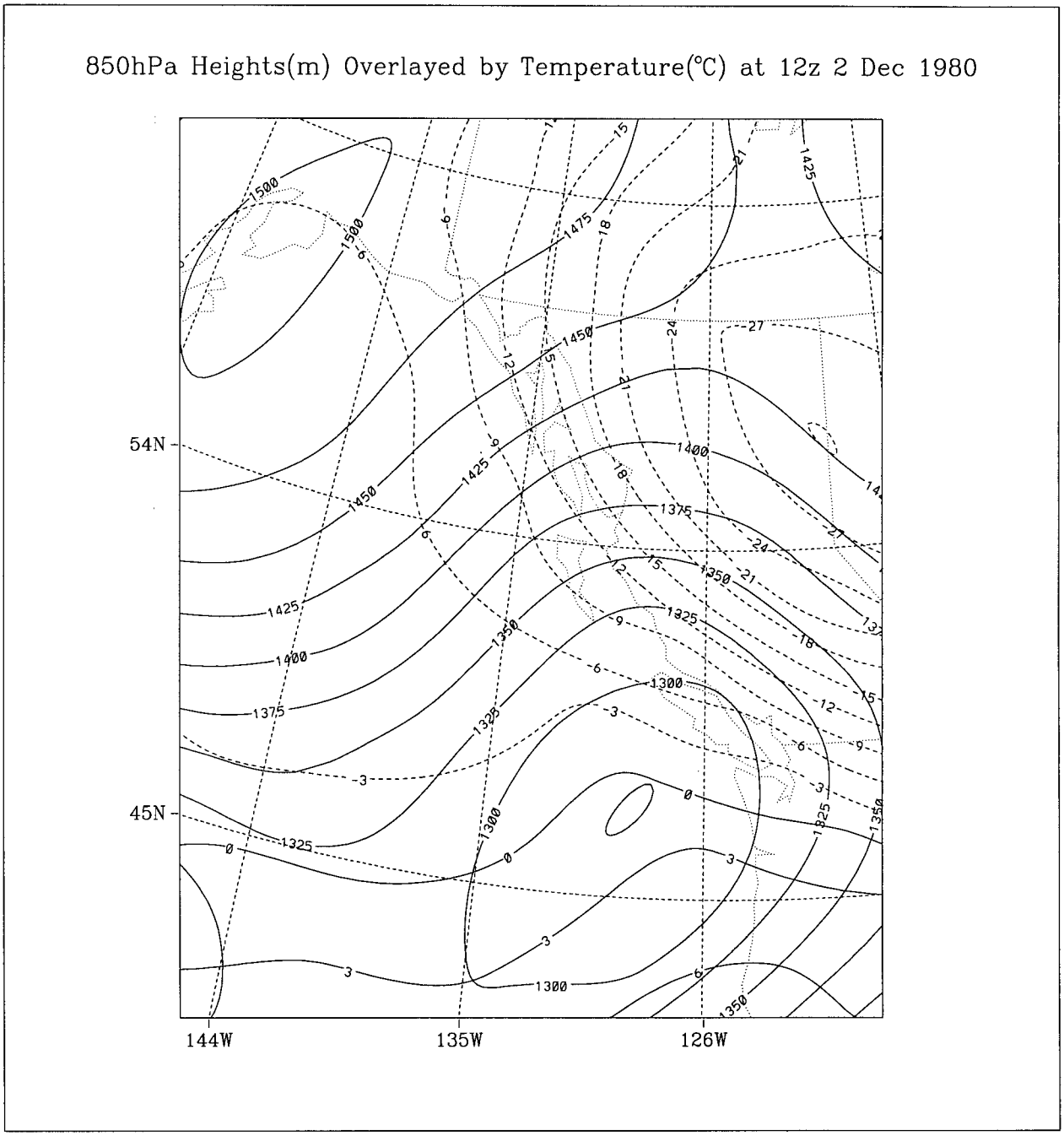

Figure 4.13: As in Figure 4.11 but at 12z 2 Dec 1980.

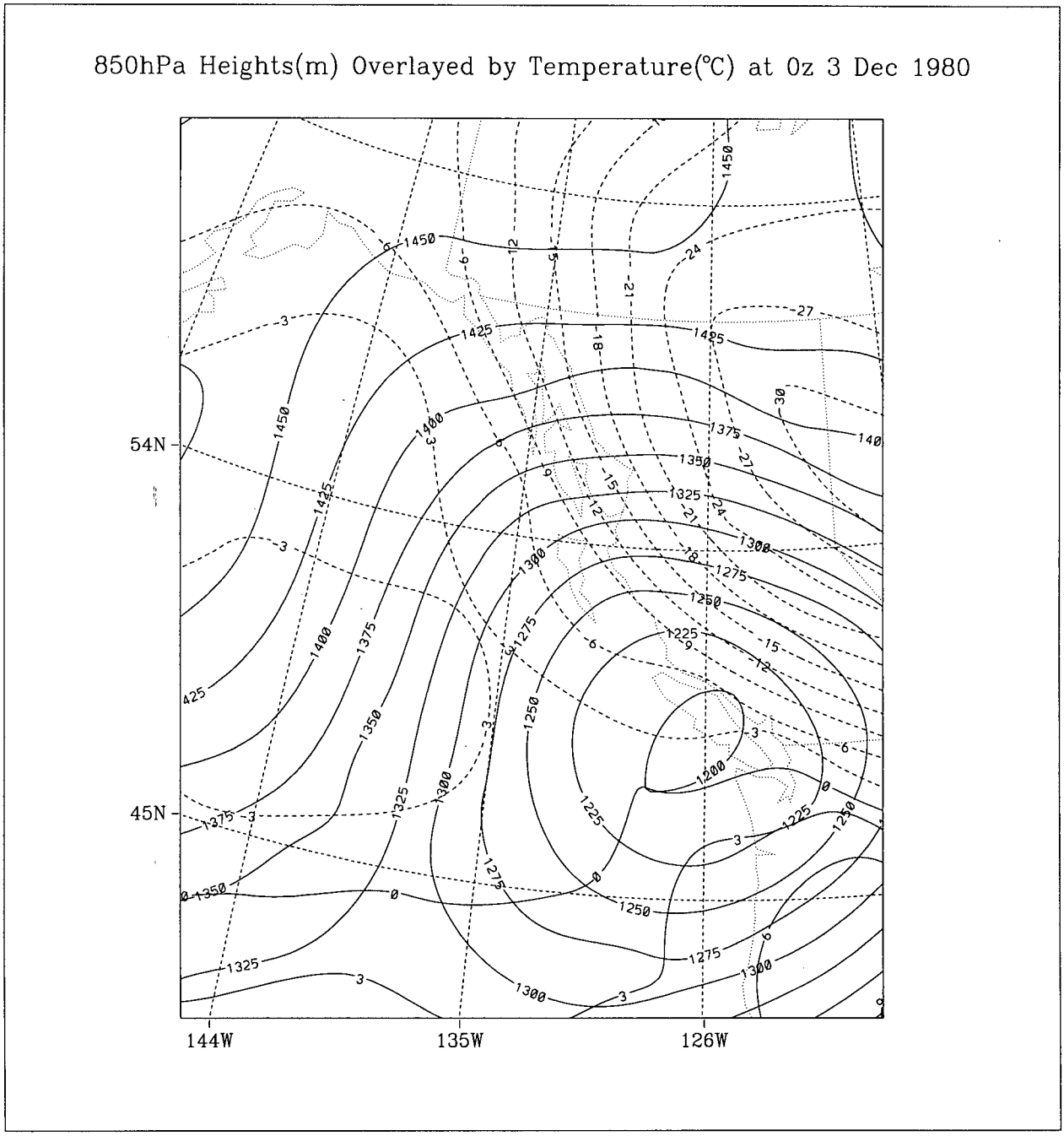

Figure 4.14: As in Figure 4.11 but at 0z 3 Dec 1980.

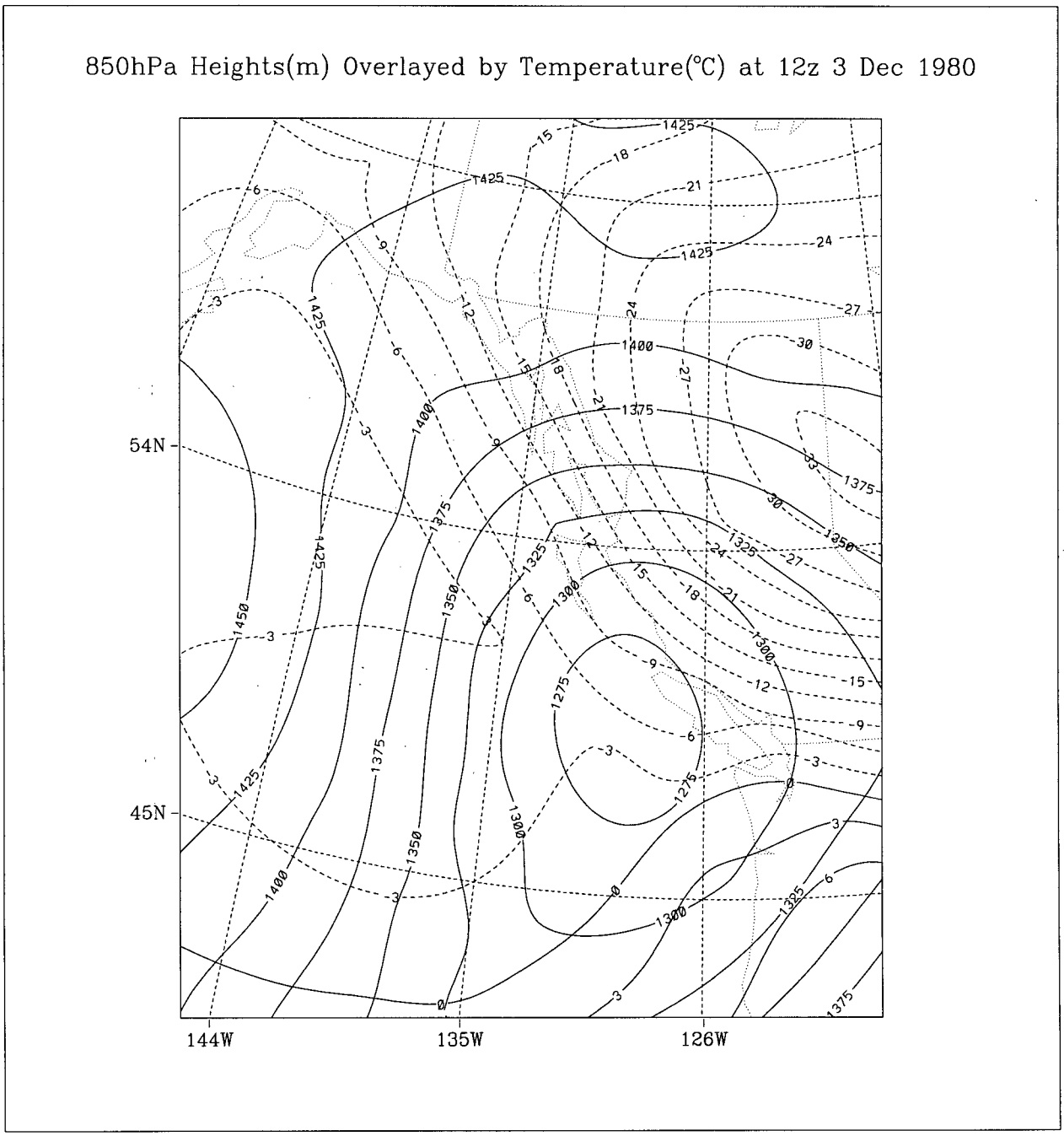

Figure 4.15: As in Figure 4.11 but at 12z 3 Dec 1980.

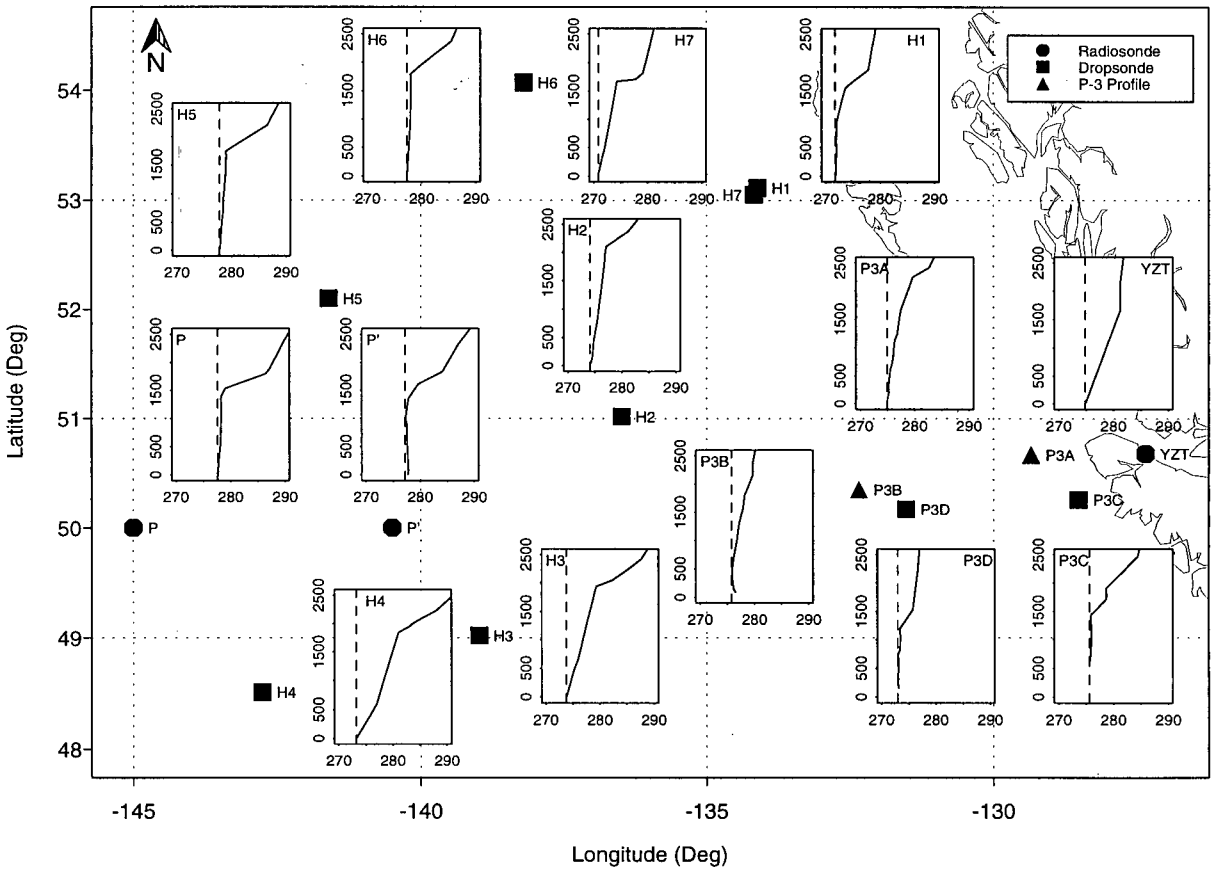

Figure 4.16: Profiles of θ_v obtained during mission #6. Vertical coordinate is height in meters and horizontal coordinate is virtual potential temperature (θ_v) in Kelvin degrees. Dashed lines indicate minimum temperature in the profiles. A profile can be matched with its respective location by pairing the station label with its twin on the profile plot. Locations are shown by the solid symbols.

increase to the west and to the south.

A majority of the profiles also exhibit weak stability through all levels. The profiles furthest upwind tend to have the strongest stratification as the cold continental air has presumably had little time to destratify by interacting with the underlying warm water surface. There is a weakly unstable region in the lower portion of both the station P′ and P3B profiles. Profiles in the northwest and southeast corners show well mixed conditions with nearly neutral lapse rates. Stability is strongest in the northeast and southwest portions of the study area, and the profile exhibiting the greatest stability is the one furthest south (H4). This behaviour is contrary to observations by Grossman and Betts (1990) of increasing instability downwind.

The relative strength of stability between profiles can be seen by examining Figure 4.17 ($\partial\theta_v/\partial z$). The largest gradient in the MABL is in the H4 profile (.005 Km^{-1}) but the lower portion of the Port Hardy (YZT) profile also has a steep positive gradient (.003 Km^{-1}). It is unclear what is causing the increasing downwind stability. It is possibly due to a decrease in the influence of organized secondary circulations and a subsequent reduction in mixing.

Cloud cover during mission #6 was stratocumulus overcast in the central and upper portions of the study area and scattered cumulus further to the south. In the latter region, the aircraft was probably travelling along the edge of a transition from organized large eddy vortex streets to semi-organized mesoscale cellular convection (MCC) as can be inferred from the satellite photo (Figure 4.53, pg. 121). It is possible that due to a downwind increase in cloud free skies, radiative cooling became larger than the warming resulting from the supply of heat at the ocean surface, resulting in a stability increase.

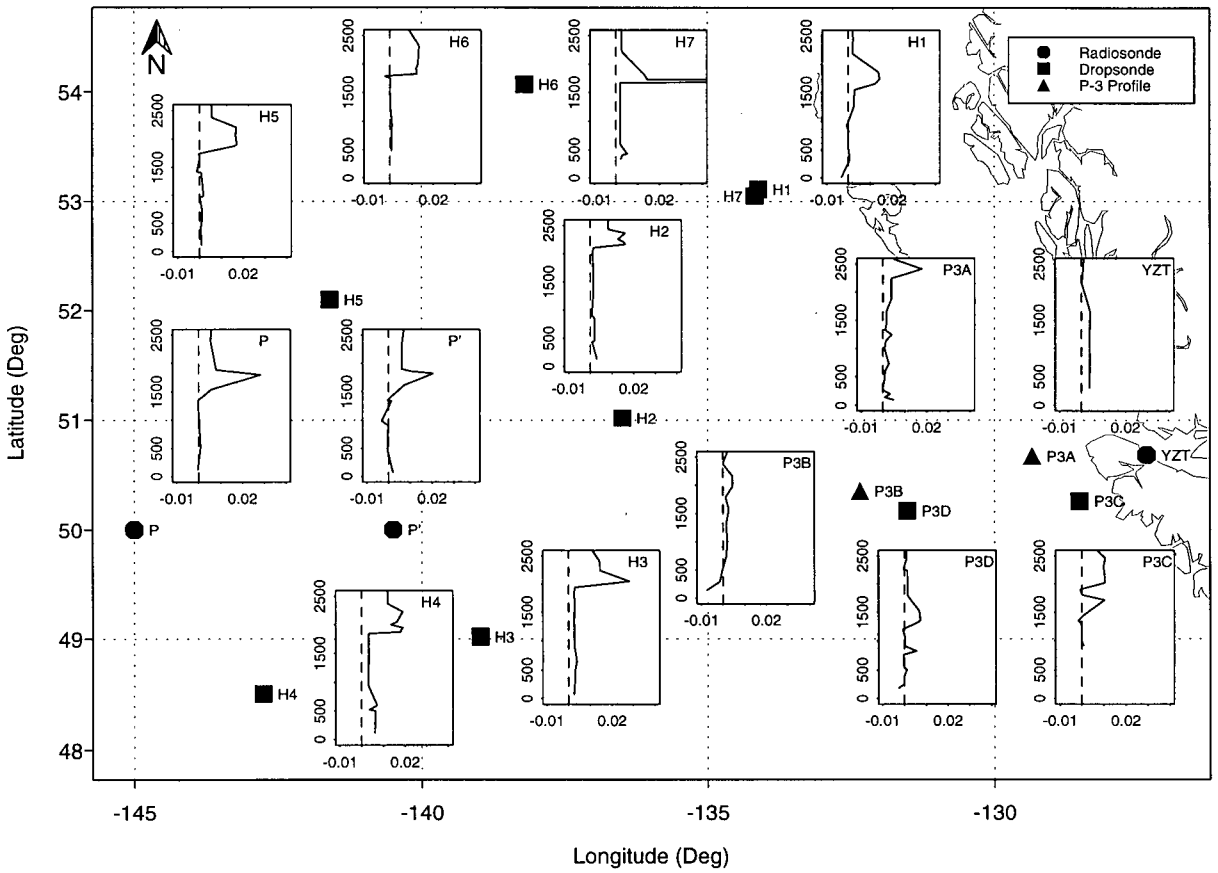

Figure 4.17: As in Figure 4.16 but for θ_v gradients. Vertical coordinate is height in meters and horizontal coordinate is $(\frac{\partial \theta_v}{\partial z})$ in Km^{-1}. Dashed line indicates zero gradient.

4.3.1.2 Humidity

Figure 4.19 depicts vertical humidity profiles and Figure 4.20 shows humidity gradient ($\partial q/\partial z$) profiles. Most of the humidity profiles have negative slopes with some exhibiting a jump of 0.5 $g\,kg^{-1}$-2 $g\,kg^{-1}$ between 1500 meters and 2500 meters. When compared with θ_v profiles there is strong correlation between heights at which these jumps occur in corresponding profiles (Figure 4.18).

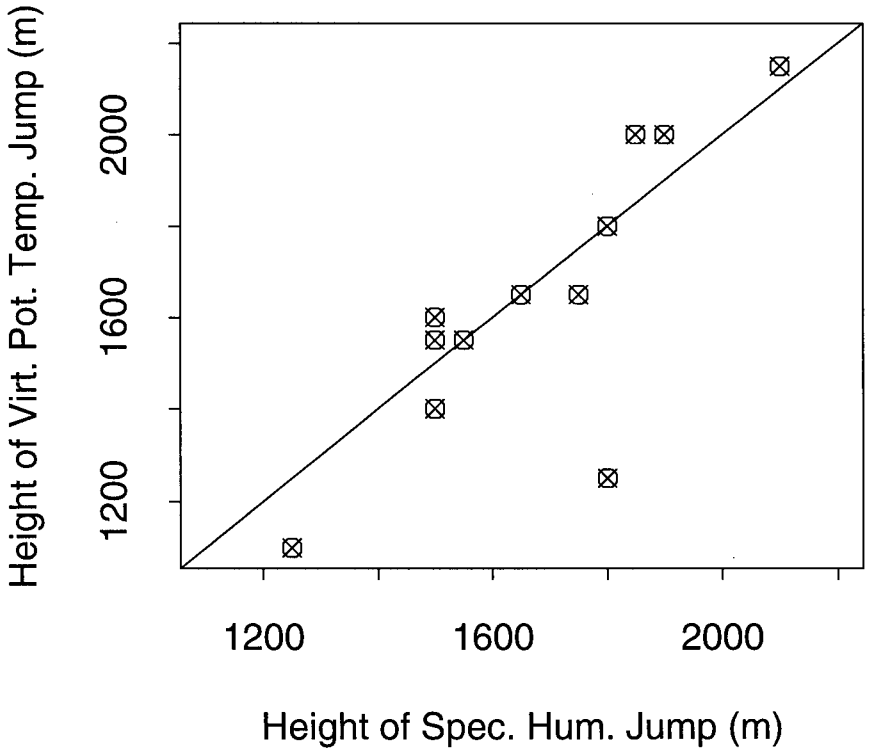

Figure 4.18: Scatterplot of heights at which humidity (q) and temperature (θ_v) profiles exhibit their first large gradients.

The southern profiles suggest the air is more moist there than it is to the north.

The moistest profile is P3B which also exhibits a very strong near surface gradient ($\approx$ 3 $\mathrm{g\,kg^{-1}/100\ m}$). The observed downwind humidity increase has been noted by others (Grossman and Betts, 1990; Brümmer *et al.*, 1992). It is due primarily to a downwind increase in Q_E but another contributor could be increased sea spray evaporation resulting from larger wind speeds over the open ocean.

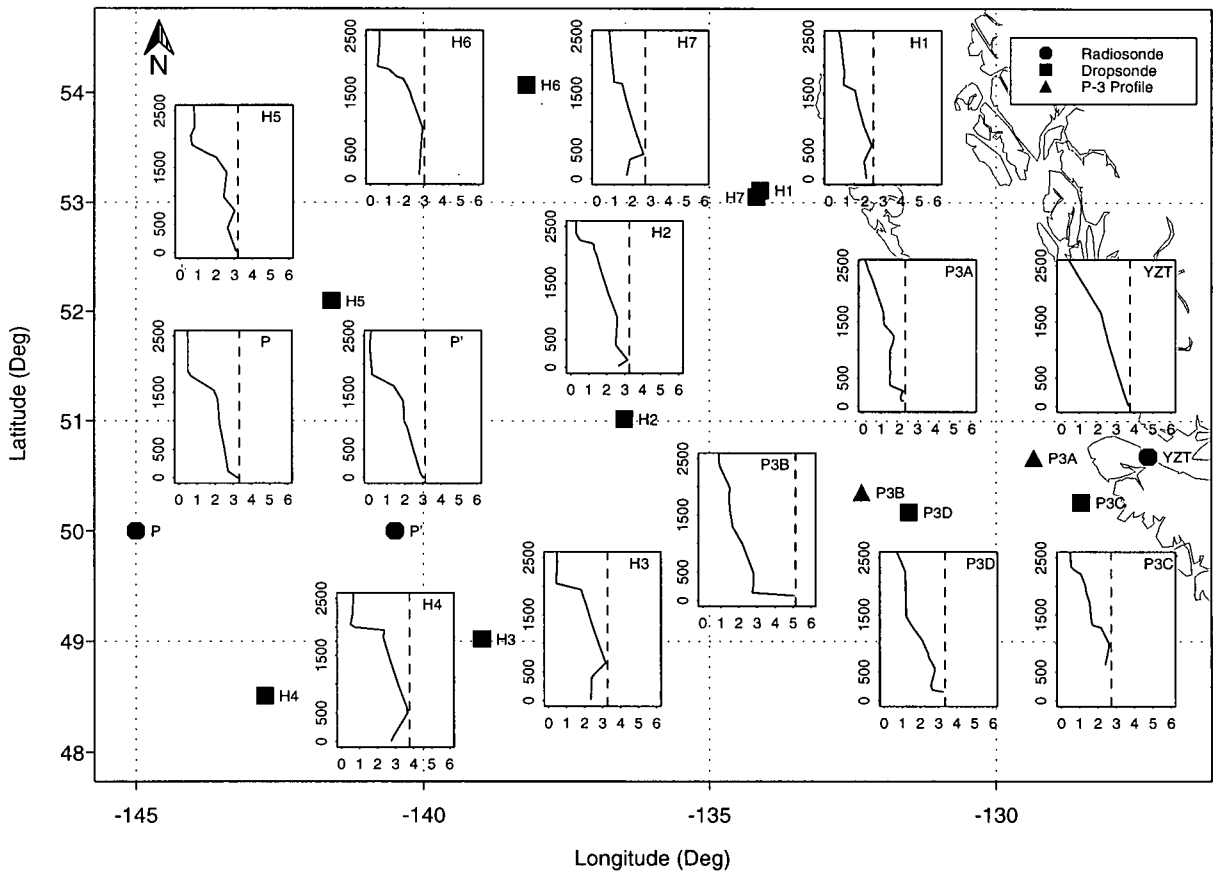

Figure 4.19: As in Figure 4.16 but for specific humidity. Vertical coordinate is height in meters and horizontal coordinate is specific humidity in $\mathrm{g\,kg^{-1}}$. Dashed lines show maximum q values.

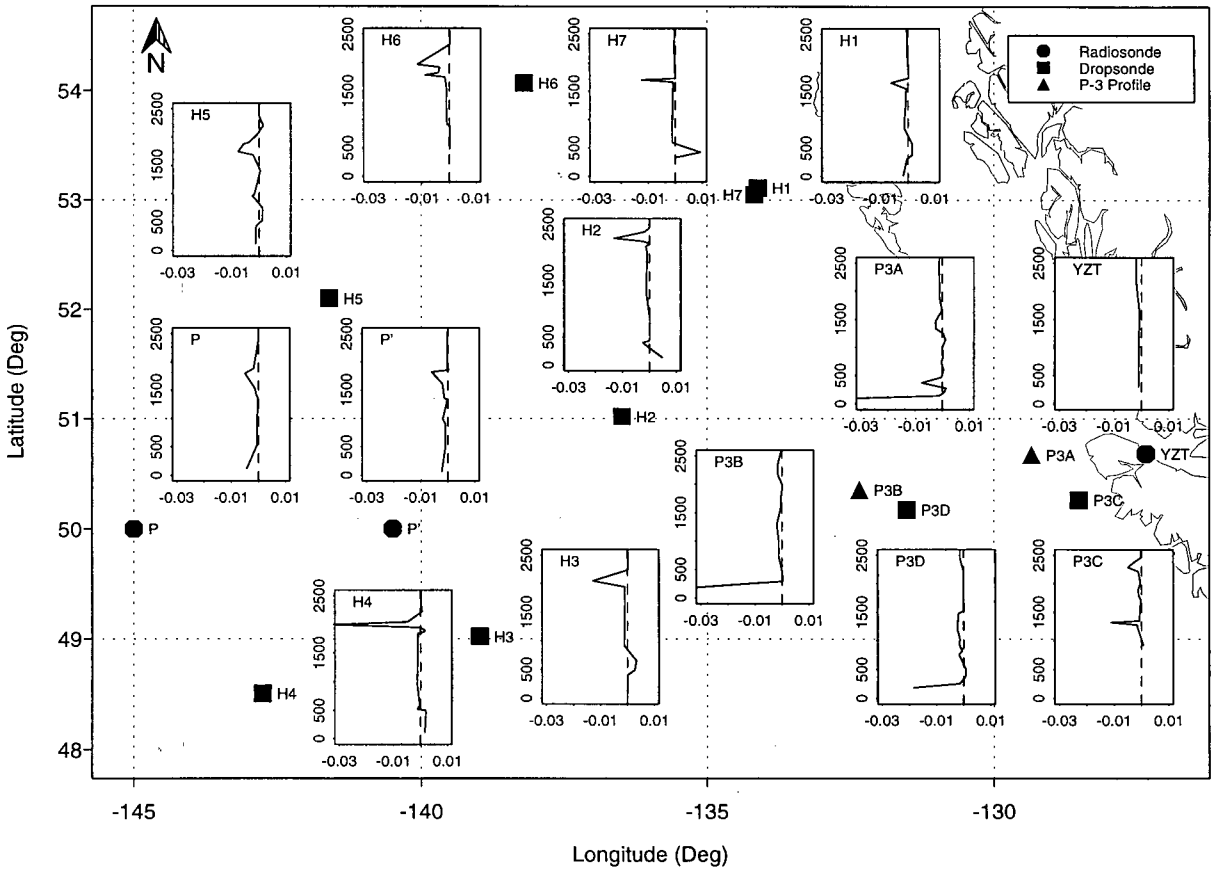

Figure 4.20: As in Figure 4.16 but for specific humidity gradients. Vertical coordinate is height in meters and horizontal coordinate is $(\frac{\partial q}{\partial z})$ in $\mathrm{g\,kg^{-1}m^{-1}}$. Dashed line corresponds to zero gradient.

4.3.1.3 Winds

Horizontal wind speed (solid line) and direction profiles are shown in Figure 4.21. There were significant data gaps in a number of the profiles and a simple linear interpolation scheme was used to calculate the missing values. The only complete profiles were provided by P-3 profiles and dropsondes. Significant uncertainty should therefore be ascribed to any fine scale variations as the interpolation should have smoothed out most of them. The data can however be interpreted in an average sense. Most of the profiles show an increase in wind speed with height. Only P3C and H4 do not. Wind speeds vary between 15 and 25 ms^{-1} in all of the profiles except for the four in the southeast corner of the domain exhibiting values between 5 and 15 ms^{-1}. Four of the profiles (H2, H5, H7 and P) show winds generally veering (vectors rotate clockwise looking down) with increasing height while three profiles (H3, H4, H6) show very little or no turning and 5 (P′, P3A, P3B, P3C and P3D) show winds backing (vectors rotate counter-clockwise looking down) with increasing height. Note that in H1 and P′ winds back at lower levels (0-1000 m). No data were available for YZT. In the northern Hemisphere, winds backing(veering) with height are associated with cold(warm) air advection according to the thermal wind equation (see Holton, 1979, eq. 3.33). This relationship is true when considering geostrophic winds only and therefore does not incorporate the effects of surface friction. It is possible that friction which would support veering(backing) winds with height during cold(warm) advection, is dominating the thermal wind while over land. Once the air moves over the water surface where friction forces are lower, an adjustment time may be required before baroclinicity becomes the dominant state. Other unquantifiable contributions from OLE circulations and nonlinear processes may also play a role.

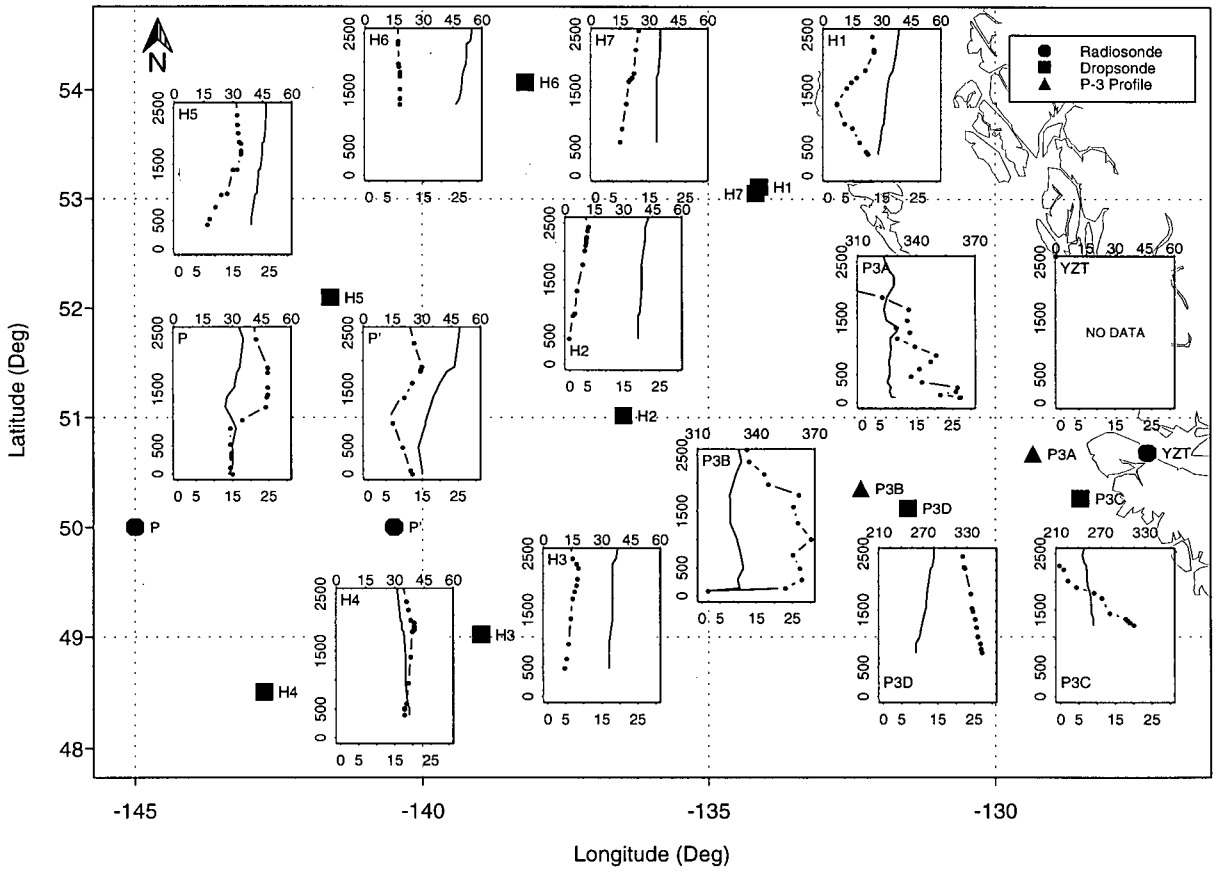

Figure 4.21: As in Figure 4.16 but for mean horizontal wind speeds. Vertical coordinate is height in meters. Lower horizontal coordinate is mean wind speed in ms^{-1} and upper horizontal coordinate is wind direction in degrees. Solid line is wind speed and dash-dot line is wind direction.

4.3.2 Mean Horizontal MABL Structure

In this section, horizontal moisture, temperature and wind characteristics at four predefined levels (surface, 50 m, 90 m, 150 m) are discussed. Contouring is based on an objective analysis scheme (LeTraon, 1990) outlined in Appendix A. Unless otherwise indicated, a smoothing radius of 90 km was used on each field.

Error estimates are also included in the form of contour plots which for most fields appear below the estimate of the variable in question. The error estimate is given in most instances as a relative value combining errors arising from both objective analysis and instrumentation (See Table 3.1). Interpolation errors can be broken down further into discrepancies between observed and estimated values and a further uncertainty due to "guessing" the mean field with the set of fundamental functions. An additional error ϵ of 10% of the interpolation error was added to the interpolation error to compensate for small unresolvable scales. Instrument error and interpolation error were summed together.

4.3.2.1 Temperature

Contour plots of θ_v at three levels (50 m, 90 m, 150 m) are shown in Figures 4.22 to 4.24. A downwind temperature increase can be seen at all levels. The temperature ranges from 271 K and 278 K over a distance of $\approx$ 800 km, corresponding to a temperature gradient of $\approx 0.9^o/100$ km. Brümmer *et al.* (1992) suggest a downstream increase in temperature is controlled by both sensible heat flux and longwave radiational cooling. However, in their study the SST gradient was orientated nearly parallel to the mean wind which would act to optimize downwind boundary layer modification and possibly obscure contributions from other variables.

Estimates of vertical θ_v variation were made by visual inspection of superimposed contour plots at any two levels. Between levels 1 and 2 ($\Delta z = 40$ m) temperature contours at level 1 exceed those at level 2 by .25 K implying weak unstable stratification. This amount is smaller than the error estimate for the region, however the consistent trend suggests that the observation is significant. It is difficult to draw the same conclusion for the vertical θ_v variation between levels 2 and 3 ($\Delta z = 60$ m). Most of the contours coincide with one another which corresponds to convective well mixed conditions. These results are subject to an error which increases substantially downwind. If it is assumed that these observations are characteristic of the lower levels in the boundary layer then it is apparent that the surface layer is thermally supporting vertical transport and is therefore contributing to the mean modification processes occurring within the entire layer. As further interaction occurs downwind, the region of negative $\partial\theta_v/\partial z$ should thicken and mixing of mass and heat should proceed higher in the boundary layer. The above observations serve further to complete the description of the MABL vertical temperature structure.

Instrument error contributes approximately 0.3 K for a typical θ_v of 275 K. The interpolation error is dependent upon the vicinity of an arbitrary point to an observed point so the relative contribution of interpolation error to that contributed by instrumentation will vary considerably over the region. In Figure 4.22 (level 1) the error is large to the northeast of the Queen Charlotte Islands and in the southern region. Similar error patterns occur for levels 2 and 3 however more confidence can be placed in downwind MABL structure at level 2 and in crosswind MABL structure at level 3. Errors are also significant in the northwest portions of the level 2 and level 3 domains.

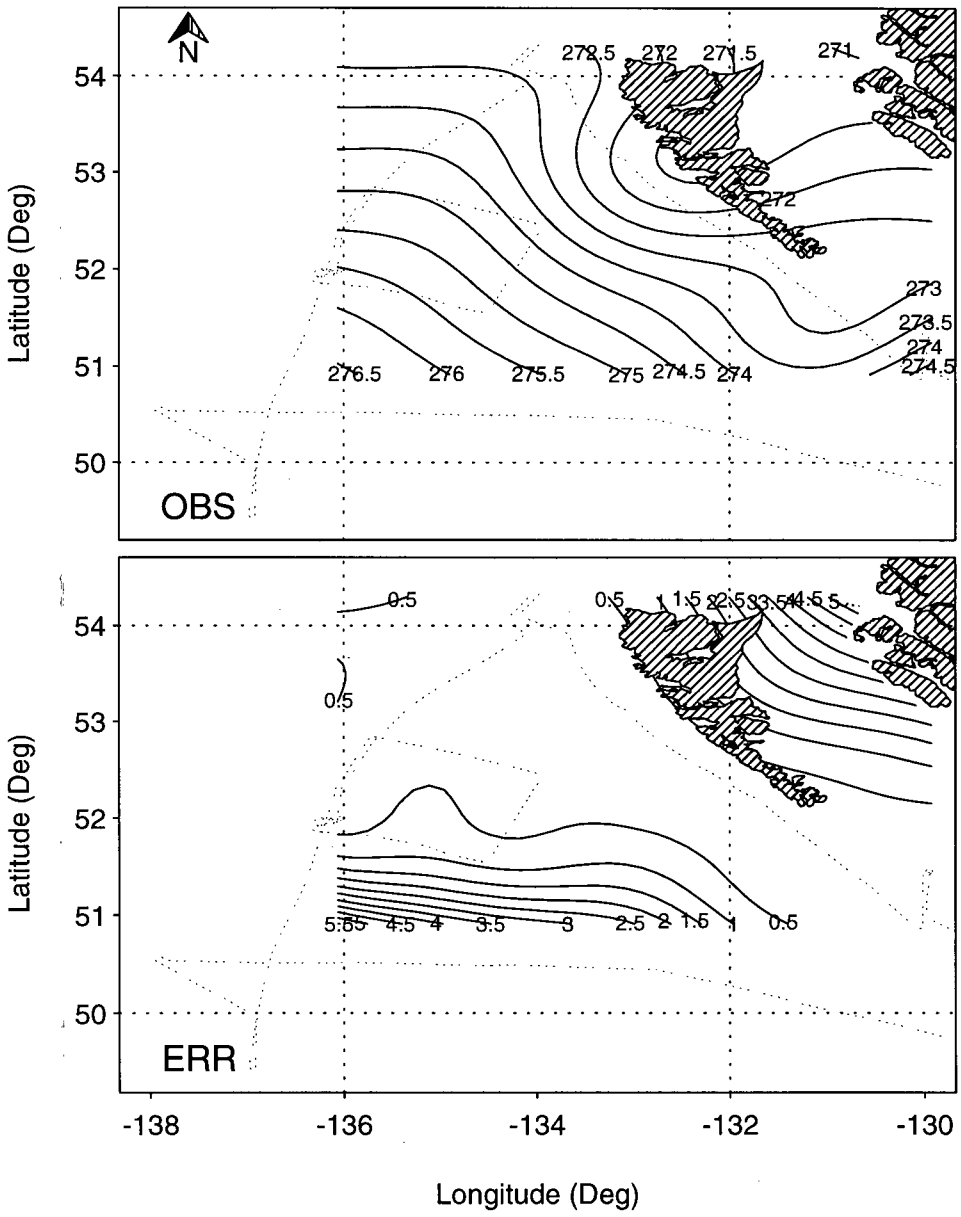

Figure 4.22: Interpolation estimates of virtual potential temperature θ_v (top panel) at level 1 (50 m) and error (bottom panel) arising from both interpolation and instrumentation. Units are in K and the contour interval is 0.5 K for both fields.

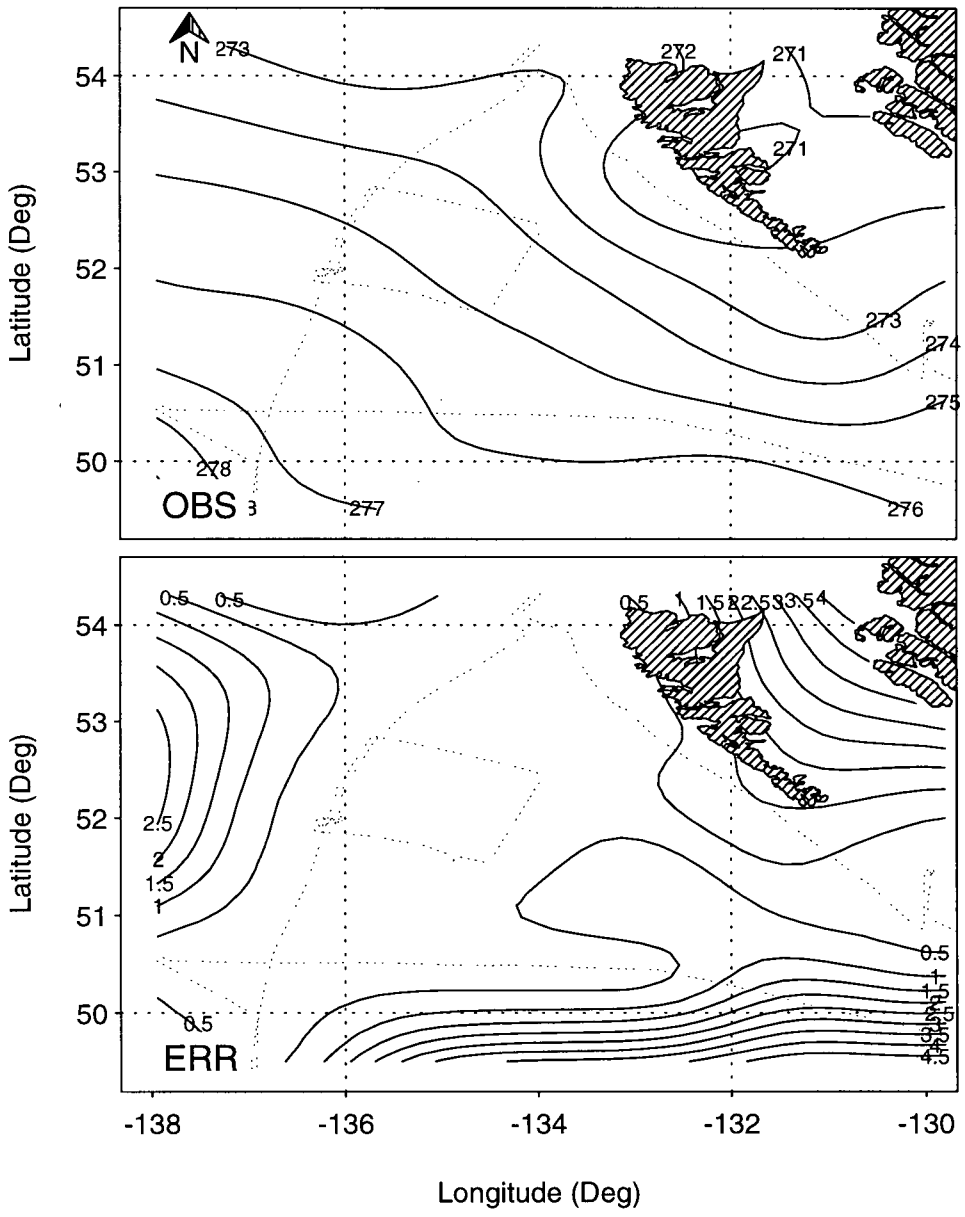

Figure 4.23: As in Figure 4.22 but for level 2 (90 m). Contour interval is 1 K for observations and 0.5 K for errors.

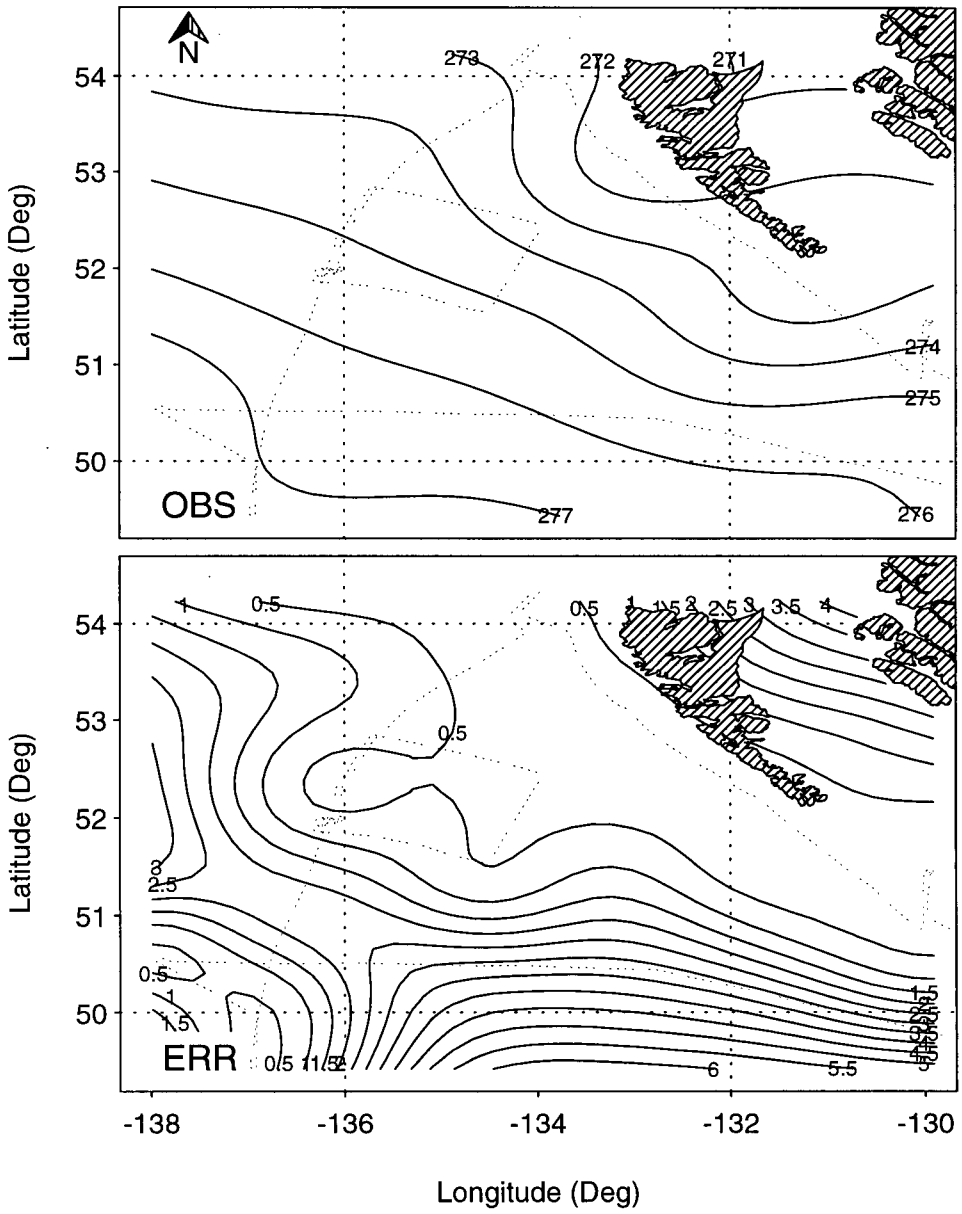

Figure 4.24: As in Figure 4.22 but for level 3 (150 m). Contour interval is 1 K for observations and 0.5 K for errors.

4.3.2.2 Moisture

Contour plots of specific humidity (q) (top panels) and error estimates (bottom panels) at levels 1 through 3 are shown in Figures 4.25 through 4.27. At each of the three heights, q increases downwind. Moisture at level 2 increases twofold (1.4 $g\,kg^{-1}$ to 2.8 $g\,kg^{-1}$) between -134W 54N and -136W 49N with similar gradients evident in both levels 1 and 3.

The circular contour pattern in the lower portion of the level 2 plot does not appear at level 1 but manifests itself to a lesser degree at level 3. Four distinct extrema appear at level 2 with center values ranging from 2.4 $g\,kg^{-1}$ to 2.8 $g\,kg^{-1}$. The maximum spatial scale of these features varies between 75 km and 150 km. They may correspond to MCC (i.e. high moisture content in regions of upward convective motion) but could also be an adjustment by the objective analysis to higher data density in the southwest region of the plot. Such a signature does not appear in the θ_v fields and therefore lends credence to the presence of MCC. Conversely there is positive correlation between the number of data points at any given level and the "strength" of the extrema, implying that the features are an artifact of the objective analysis. It is difficult to see the extrema at level 1 because the data was distributed over a smaller region, the southern boundary of which lies north of the locations of the features in question at the other two levels. At level 3, two extrema can be found at opposite sides of the plot. A high (> 2.6 $g\,kg^{-1}$) persists through all three levels, and can be found in the southeast region of the plot. This particular extremum could be a result of nonstationarity (see section 3.6).

Vertical variation in q is small. No discernible overall contour misalignment between levels exists, leading to the tentative conclusion that the vertical moisture gradient is essentially zero in the lower levels. The same conclusion cannot be drawn in the south where moisture characteristics vary significantly between each level.

Error estimates for q bear a similar pattern to those determined for θ_v. At level 1, error estimates exceed observed values in the northeast, northwest and south portions of the domain rendering results in those regions inconclusive. At levels 2 and 3, errors range from 0.5 $g\,kg^{-1}$ to 3.5 $g\,kg^{-1}$ with distributions similar to that at level 1.

4.3.2.3 Sea Surface Temperature

Contours of sea surface temperature (SST) are shown in Figure 4.28 (top panel) accompanied by error estimates (bottom panel). The field was calculated using objective interpolation of SST values obtained by the PRT-5 radiometer onboard the P-3.

The gradient is oriented SE-NW with a magnitude of $\approx 0.5°/100$ km. The total SST change over the domain is $\approx$ 2 degrees with the strongest gradient between 136W and 134W and north of 51N ($\approx 0.5°/100$ km). The maximum value of 284 K appears in the southeast corner of the domain and the minimum of 281 K appears in the northwest corner. The average value is 282.5 K. The oblique orientation of the SST gradient relative to the mean wind (and temperature gradient) direction would act to reduce the strength of sensible heat transfer at the sea surface. Observations over the Gulf Stream (Grossman and Betts, 1990) during the 28 Jan 1986 (GALE) CAO indicate very large total heat transfers coinciding with SST gradients parallelling the wind. Gradients oriented 180° to one another could result in negative sensible heat fluxes depending on the intensity of the CAO. It is expected that the SST distribution itself would be affected by two separate processes. The first is cooling resulting from equilibration of the vertical temperature difference near the surface. Sensible heat is transferred away from the ocean causing it to cool. The second process is cooling from evaporation at the surface as latent heat is transferred to the atmosphere by water vapor.

Error estimates of SST are shown in the bottom panel of Figure 4.28. A tongue of increased error can be seen between 51N and 52N and is wholly attributable to data

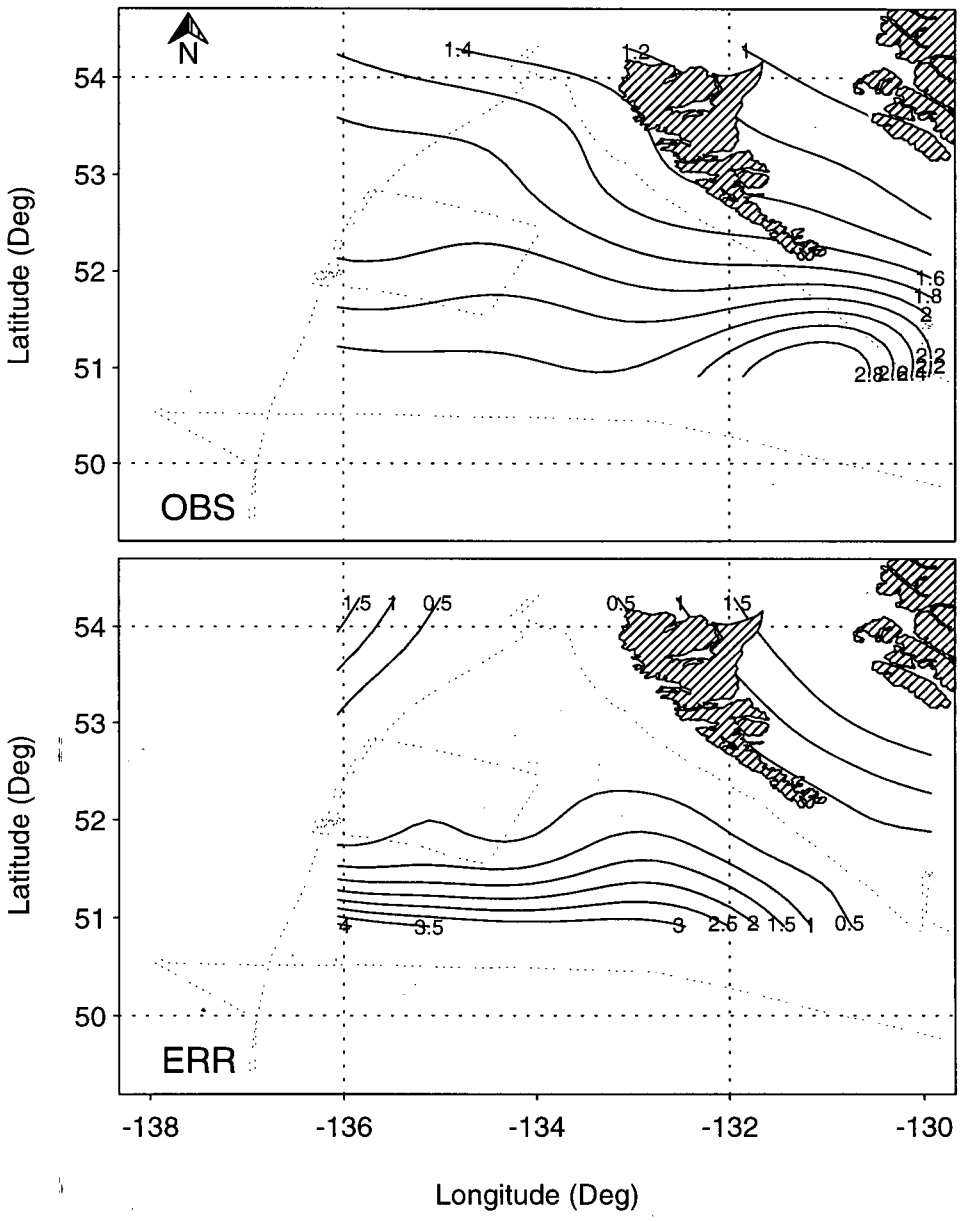

Figure 4.25: Interpolation estimates of specific humidity (top panel) at level 1 (50 m) and error (bottom panel) arising from both interpolation and instrumentation. Units are in $g\,kg^{-1}$, and the contour intervals are 0.2 $g\,kg^{-1}$ for observations and 0.5 $g\,kg^{-1}$ for errors.

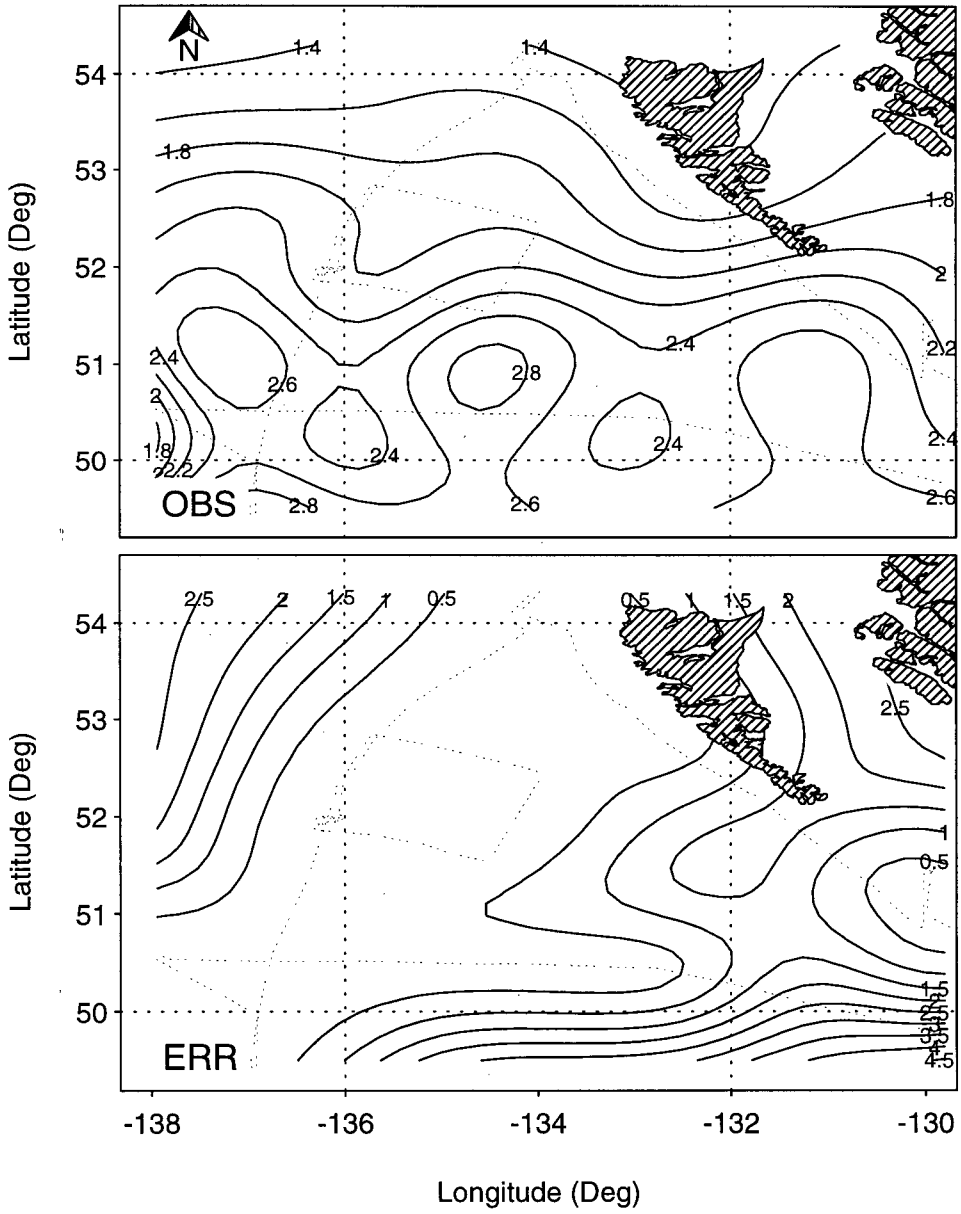

Figure 4.26: As in Figure 4.25 but for level 2 (90 m).

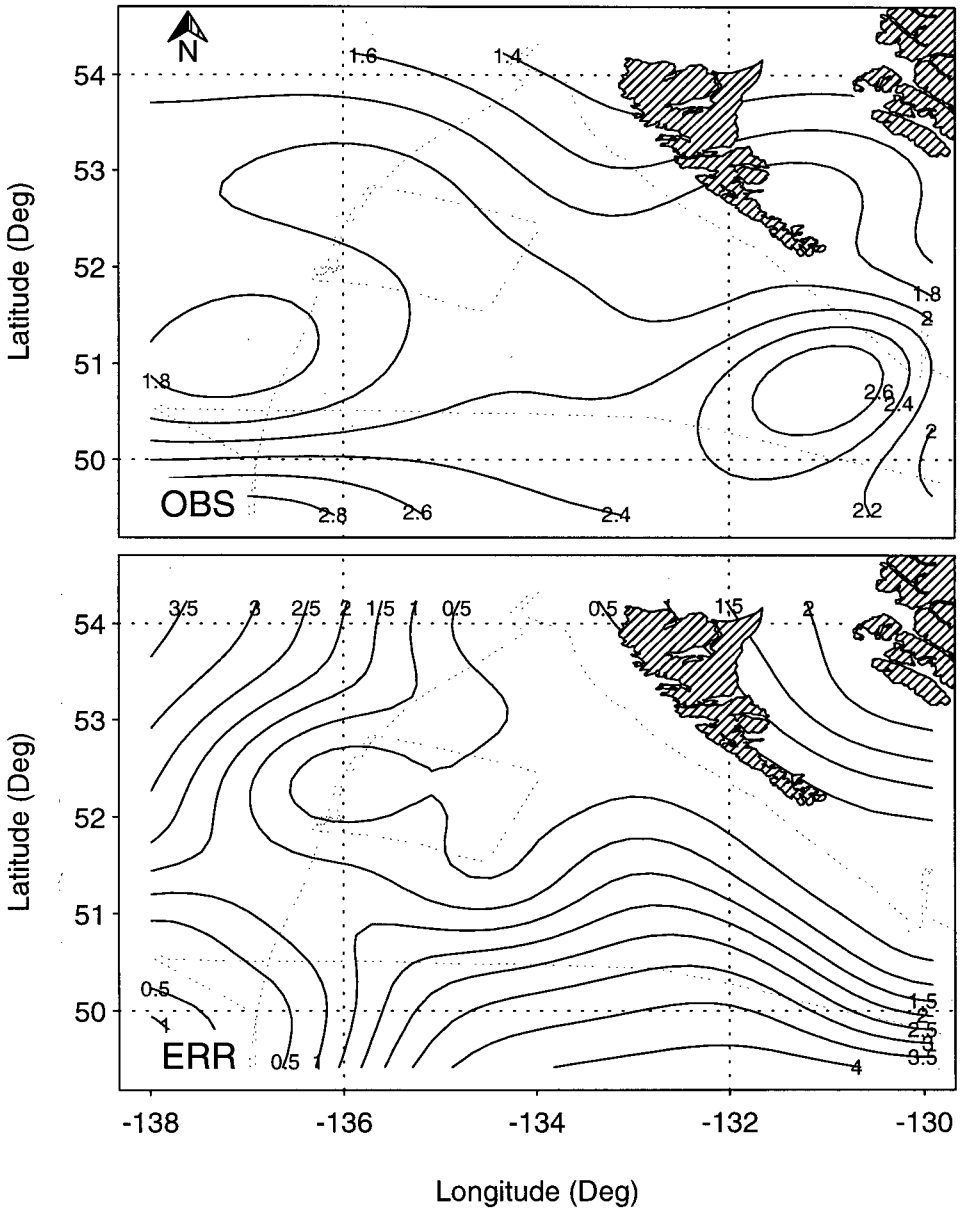

Figure 4.27: As in Figure 4.25 but for level 3 (150 m).

paucity. Elsewhere errors are large to the northwest and northeast.

4.3.2.4 Heat Fluxes

Plots of sensible heat flux (Q_H) and latent heat flux (Q_E) were based on an objective analysis of eddy correlation measurements obtained during the P-3 flight.

Q_H is shown in Figure 4.29. The largest values occur near the middle of the plot (≈ 90 Wm^{-2}) with a relative minimum (10 Wm^{-2}) located to the southeast of the maximum. Observed Q_H values range from 10 Wm^{-2} to just over 100 Wm^{-2}. Errors are highest near the maximum and in the domain corners (far from observations). The largest error is 60 Wm^{-2}. Interpolation errors account for approximately two thirds of the total.

Q_E is depicted in Figure 4.30. There is a minimum southwest of Moresby Island (80 Wm^{-2}) and a maximum (280 Wm^{-2}) southwest of the minimum. The maximum falls close to the Q_H maximum. Errors in the interpretable region of the domain range from 50 to 100 Wm^{-2} and towards the corners of the domain (northwest, northeast and southeast) errors are as high as 400 Wm^{-2}.

Total heat flux (Q_T) estimates are plotted in the top panel of fig 4.31. Because of the significantly larger contribution to Q_T by Q_E relative to Q_H (see Fig 4.32 below) the distribution more closely resembles that of Q_E. A maximum (340 Wm^{-2}) is situated in the south. The smallest value (100 Wm^{-2}) appears south of Moresby Is. Error estimates are plotted in the bottom panel of Figure 4.31. The largest error of 150 Wm^{-2} coincides with the Q_T maximum in the southern region of the domain. The validity of the maximum appearing in both the Q_E and Q_T plots is somewhat suspect due to the large error there, but there may be some correlation between SST and Q_T. Vukovich *et al.* (1991) observed a strong correlation between SST and surface heat flux. Overall Q_T increases downwind.

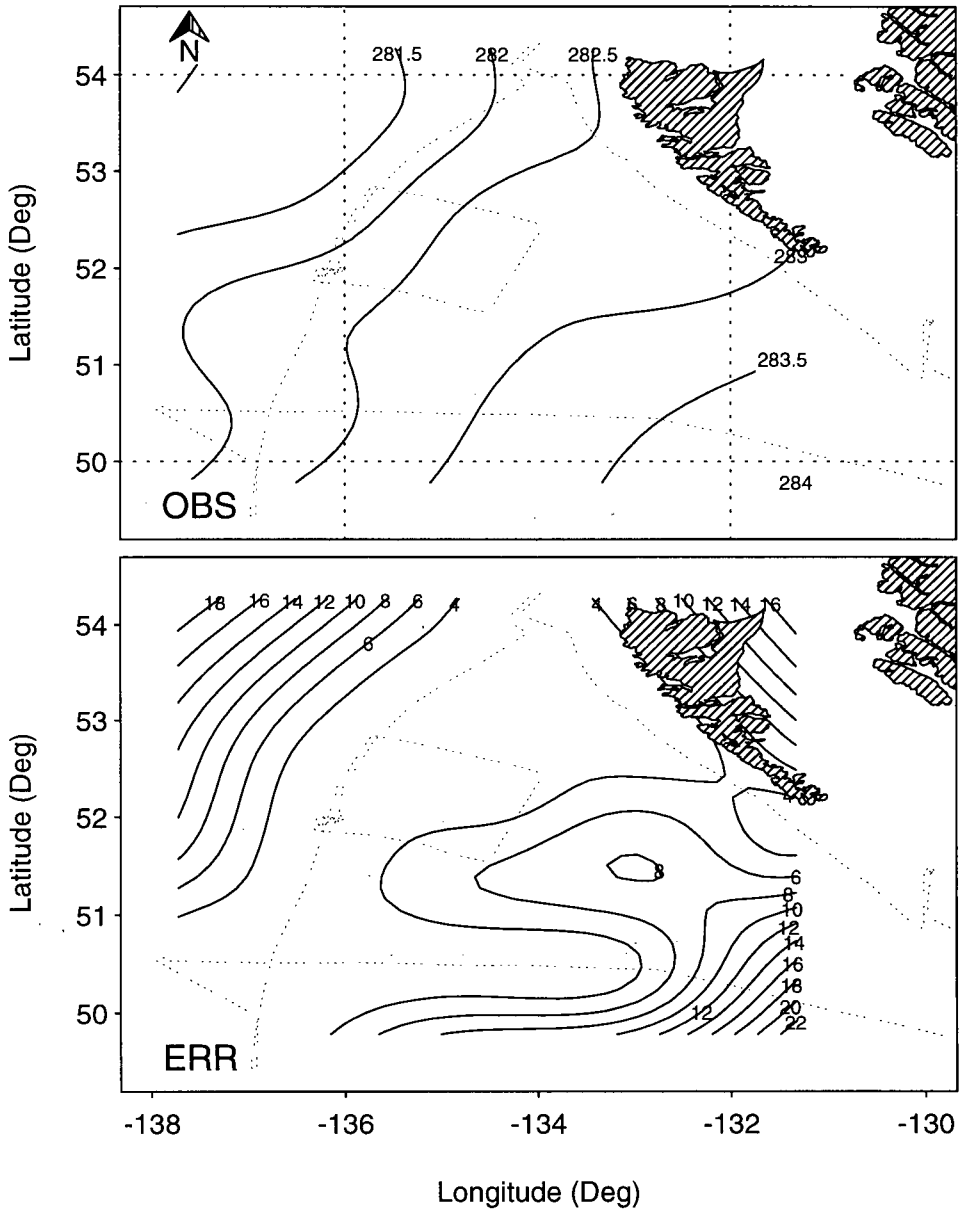

Figure 4.28: Interpolation estimates of potential sea surface temperature (θ_{SST}) (top panel) and error (bottom panel) arising from both interpolation and instrumentation. Units are in K and the contour intervals are 0.5 K for observations and 2 K for errors.

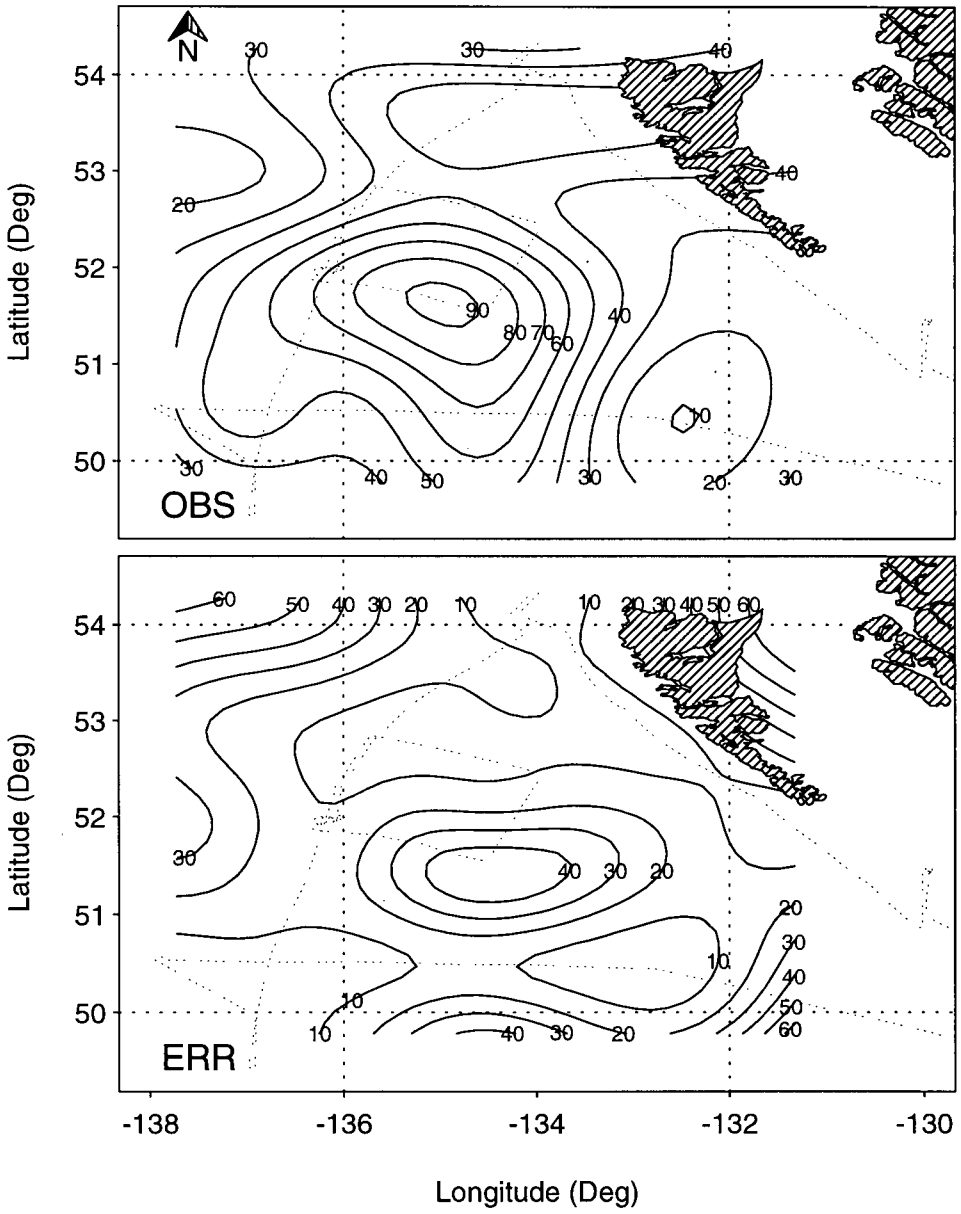

Figure 4.29: Interpolation estimates of surface sensible heat flux (Q_H) (top panel) and error (bottom panel) arising from both interpolation and instrumentation. Units are in Wm^{-2} and the contour interval is 10 Wm^{-2} for both fields.

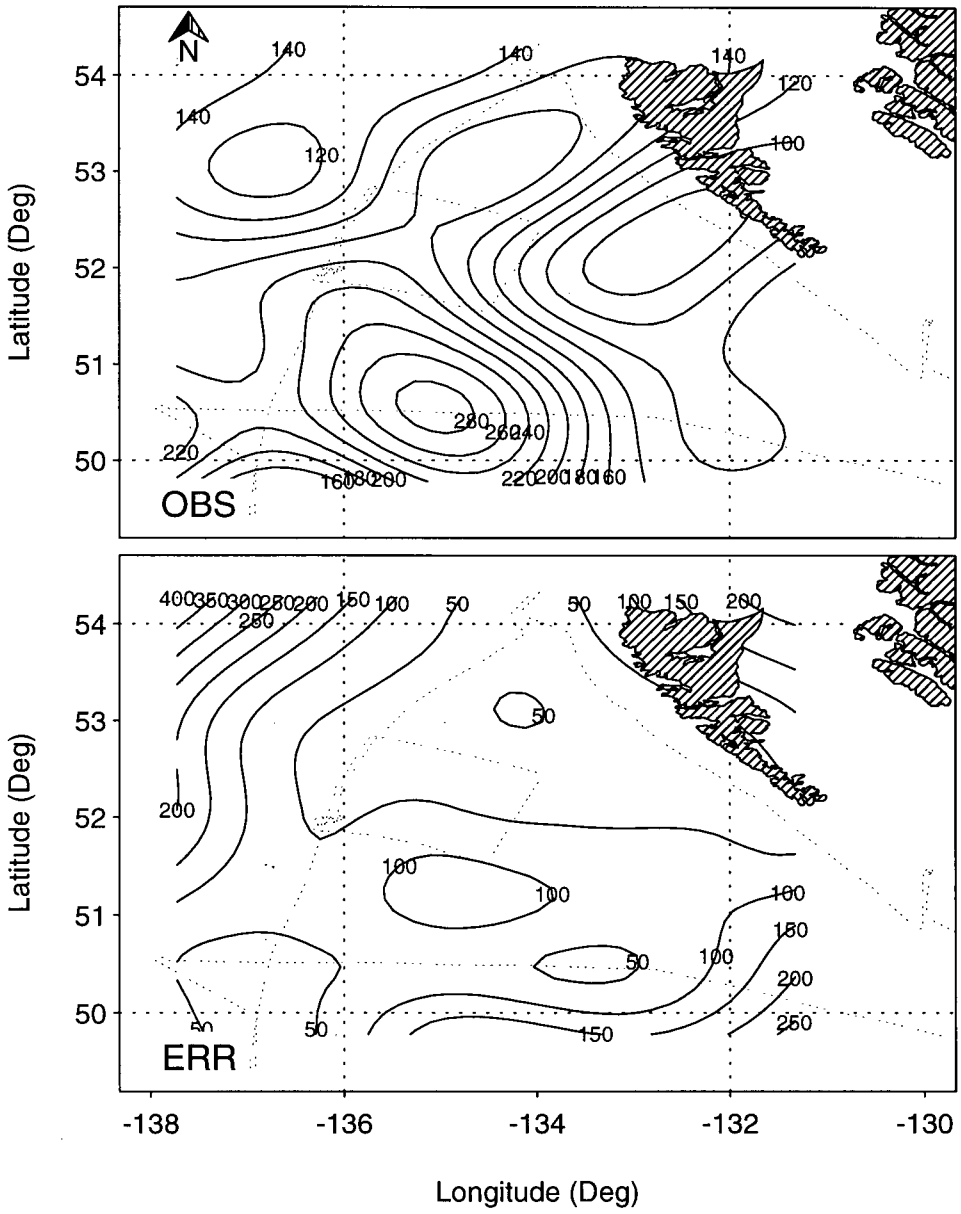

Figure 4.30: Interpolation estimates of surface latent heat flux (Q_E) (top panel) and error (bottom panel) arising from both interpolation and instrumentation. Units are in Wm^{-2} and the contour intervals are 20 Wm^{-2} for observations and 50 Wm^{-2} for errors.

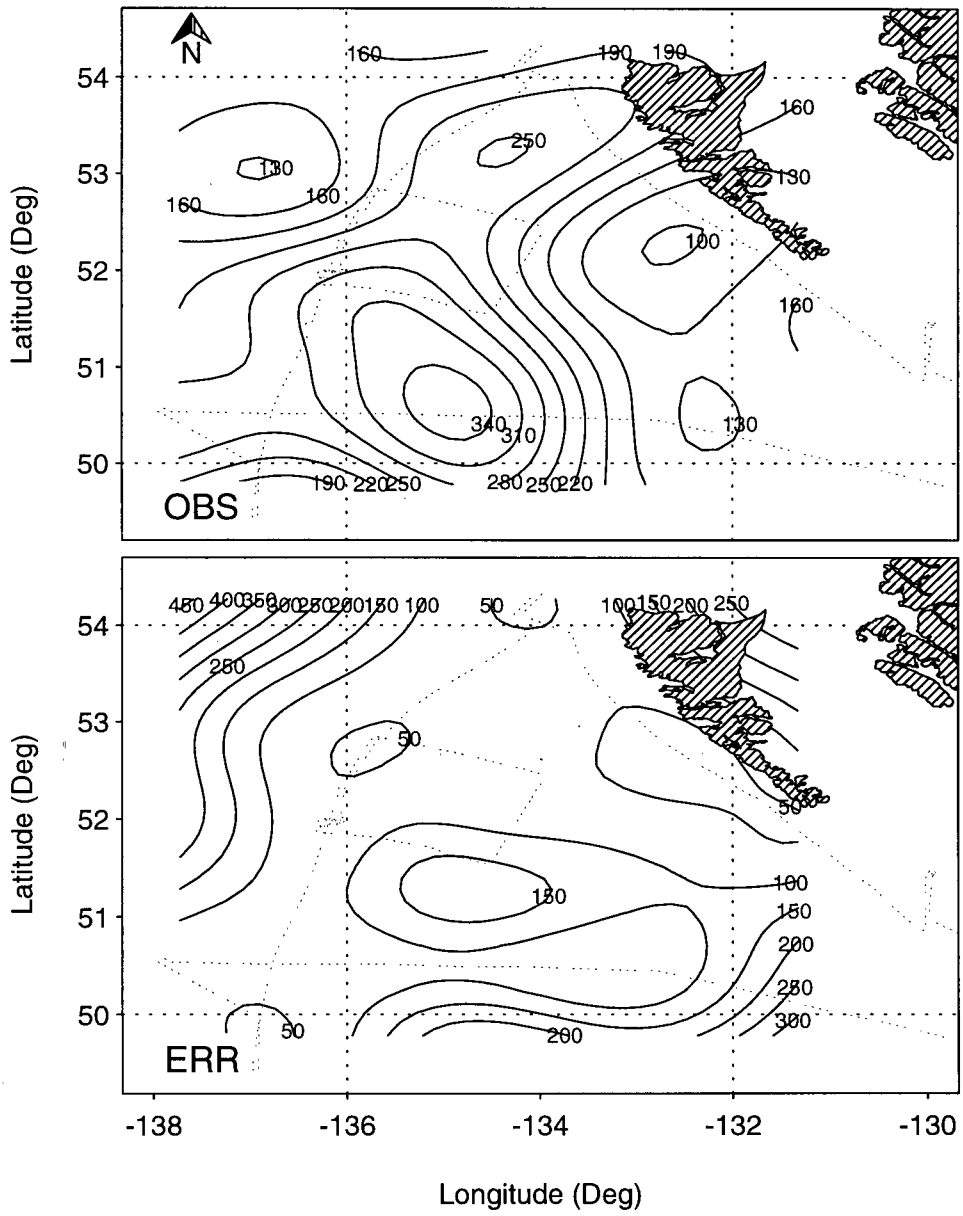

Figure 4.31: Interpolation estimates of surface total heat flux (Q_T) (top panel) and error (bottom panel) arising from interpolation and instrumentation. Units are in Wm^{-2} and the contour intervals are 30 Wm^{-2} for observations and 50 Wm^{-2} for errors.

4.3.2.5 Bowen Ratio

The ratio of sensible heat to latent heat (β) is plotted in Figure 4.32 (top panel). There is a maximum in the center of the domain (0.65). Most of the domain has β values between 0.2 and 0.4. Others (Vukovich *et al.*, 1991; Grossman and Betts, 1990) have observed similar values during CAOs. Errors (bottom panel) range from .05 to 0.5 with interpolation accounting for most of the error. It is unlikely that the large maximum is physical although the area in which it occurs is also one where large sea-air temperature differences are located.

4.3.2.6 Sea-Air Temperature Difference

Observed Sea-Air temperature differences (ΔT) and errors are plotted in Figure 4.33 (top and bottom panels respectively). Air temperatures obtained onboard the P-3 were adiabatically lowered to a reference level of 10 meters and then subtracted from SST values to obtain ΔT. Values decrease from NE to SW. Isotherms of ΔT are oriented obliquely to the mean wind and the gradient is fairly constant over the entire domain (1.5^{o}/100 km). Sea-Air temperature differences have been observed as high as 23 K (Hein and Brown, 1988; Grossman and Betts, 1990) under similar atmospheric conditions. Error values are between 4 and 6 °C over most of the domain. Values are large due both to considerable observation uncertainties in SST and to the subtraction of two large values from one another.

4.3.2.7 Boundary Layer Height

Boundary layer height (z_i) was estimated from temperature and temperature gradient profiles. The top of the boundary layer was equated with the start of either an inversion in the temperature profile or a large jump in the temperature gradient profile as one

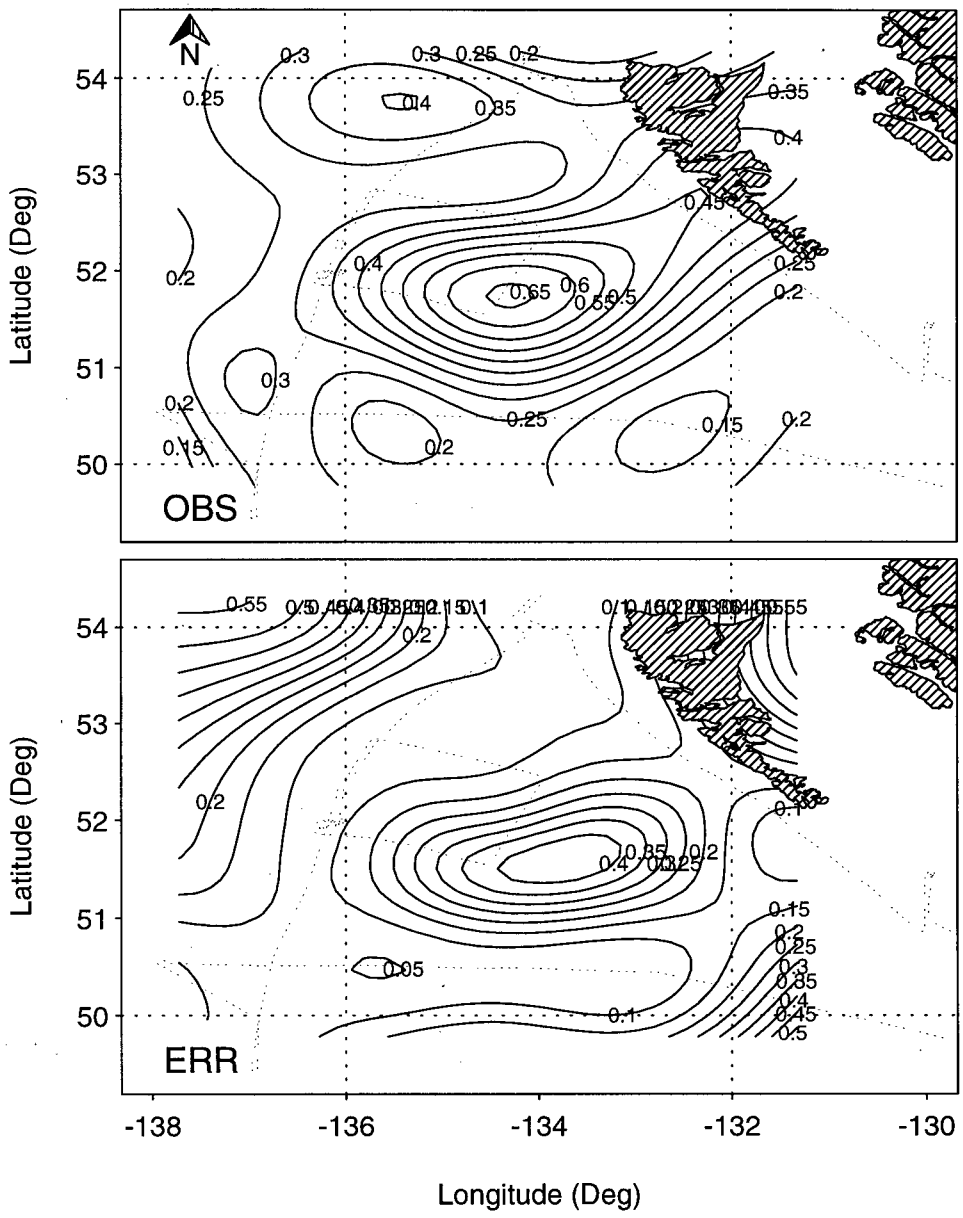

Figure 4.32: Interpolation estimates of the Bowen ratio (β) (top panel) and error (bottom panel) arising from both interpolation and instrumentation. Contour interval is 0.05 for both fields.

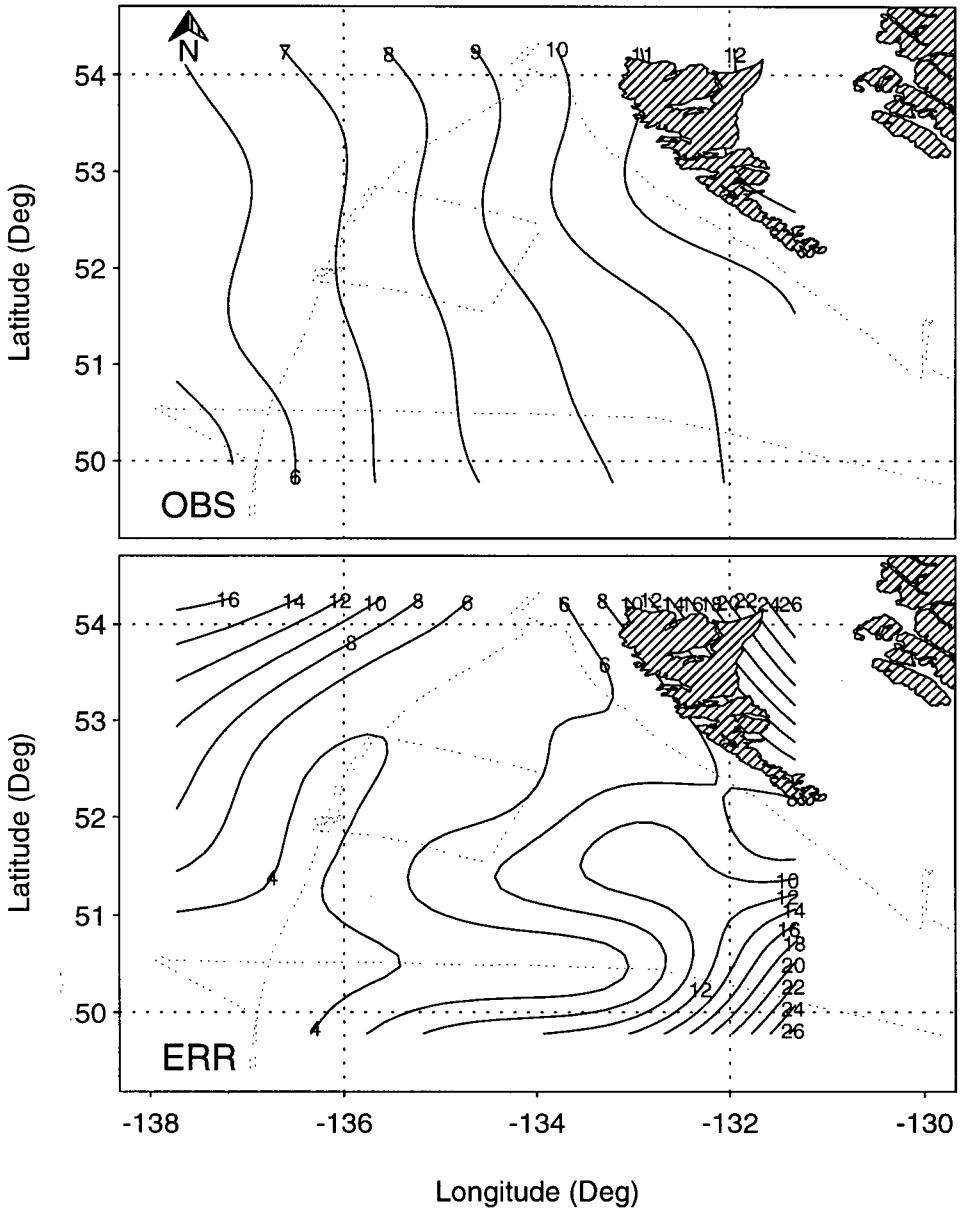

Figure 4.33: Interpolation estimates of sea-air potential temperature difference (top panel) and error (bottom panel) arising from both interpolation and instrumentation. Units are in °C and contour intervals are 1 °C for observations and 2 °C for errors.

moves upward. Because there were only 13 usable estimates of inversion base height, the interpolation grid resolution was reduced to 20×20 with a smoothing radius of 350 km. Figure 4.34 shows interpolation estimates of the inversion height. Heights increase from NW-SE with values reaching as high as 2400 m. Height contours run perpendicular to the mean wind in the upper center portion of the domain but then begin to parallel the wind further south. This observation is in contrast both to observations and to model predictions (Grossman and Betts, 1990; Vukovich *et al.*, 1991). Conversely Brümmer *et al.* (1992) observed that height isolines were *not* aligned perpendicular to the wind. They found that z_i was largest in the middle of the cloud field and decreased on either side. In this study the cloud cover decreased in the downwind direction which suggests that variable cloud distribution may be one of a number of processes contributing to a non-perpendicular orientation of the height gradient to the wind or that the interpolation is inadequately assessing the distribution. Other fields in which the gradient is predominantly SE-NW are SST and sensible heat flux which implies a correlation between Q_H and inversion height. The inversion height gradient is constant over the entire domain.

Error estimates of inversion base height appear in the bottom panel of Figure 4.34. Values are large to the northwest and southeast while values in the middle are significant but relatively smaller than on the domain outskirts. The instrumental error was somewhat arbitrary (10%) and it could be argued that an absolute error of $\approx$ 100 m would be more appropriate than a relative error which grows in proportion to the observation estimate.

4.3.2.8 Cloud

The role of cloud in the atmospheric boundary layer energy budget continues to be open to significant debate. Cess (1990) found that climate sensitivity variation between 19 GCMs was attributable to differing cloud feedback parameterizations. More

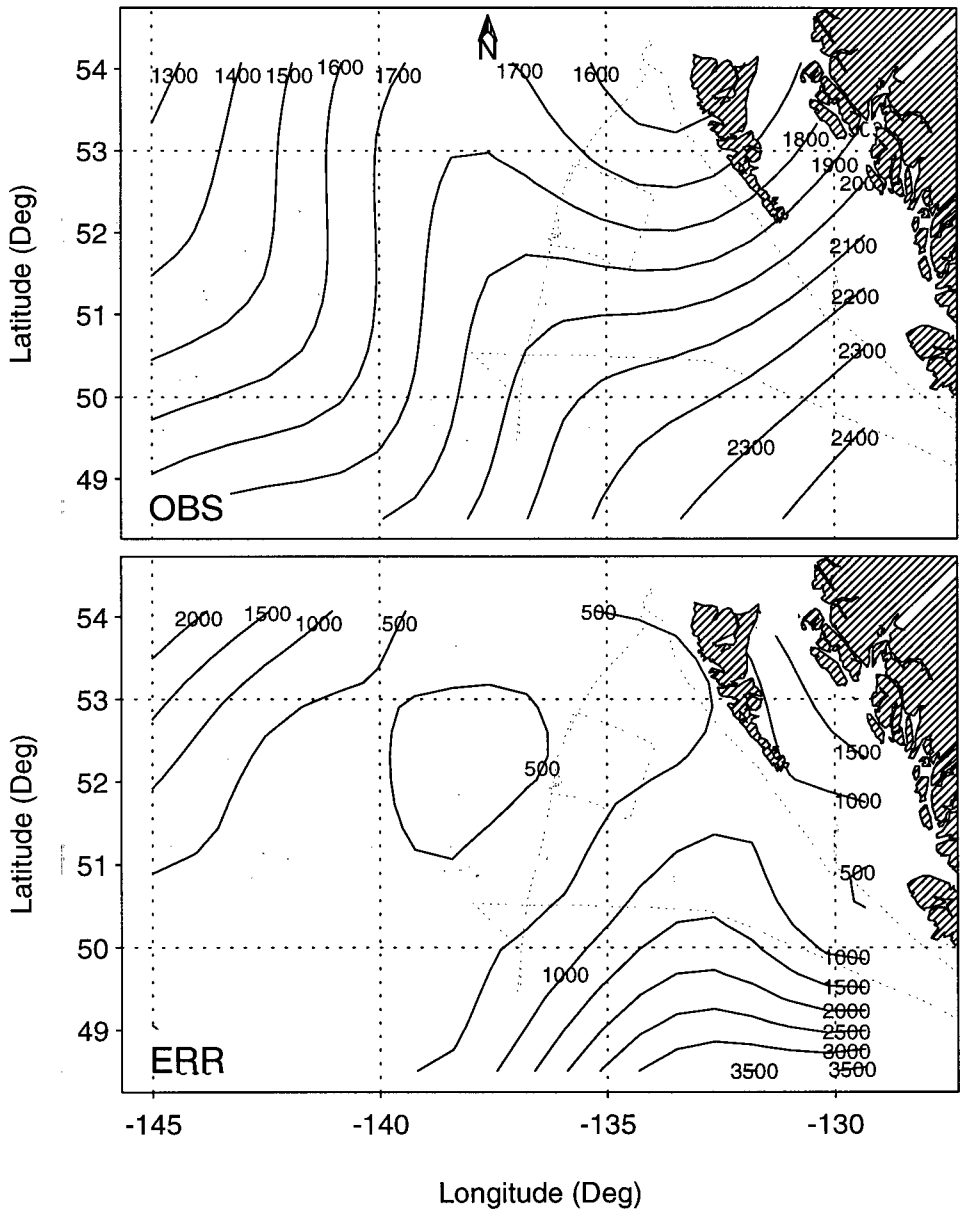

Figure 4.34: Interpolation estimates of inversion base height (top panel) and error (bottom panel) arising from both interpolation and instrumentation. Units are in metres and the contour intervals are 100 m for observations and 500 m for errors.

recently Randall *et al.* (1992) continued the model comparison and found that a change in the net surface energy budget equivalent to a uniform global 4°C increase in SST would be dominated by the change in the net surface latent heat flux rather than by cloud feedback effects. The ability of water vapor (in all phases and droplet size distributions) to reflect and absorb various wavelengths of radiation and to re-emit the energy to both the earth's surface and out to space, is inadequately quantified. Brümmer *et al.* (1992) postulated that the marine boundary layer energy balance is strongly influenced by the degree of cloud cover. For small amounts of cloud cover, incoming shortwave radiation ($S\downarrow$) dominates. During the 16 May 1988 CAO Brümmer *et al.* found that the ocean was heated in spite of large sensible and latent heat losses. However with increased cloud cover, outgoing longwave radiation ($L\uparrow$) dominated $S\downarrow$) and the ocean cooled. These observations were made during the daytime at different sun elevations. During the night or at small sun angles the role of clouds is reversed with radiative cooling dominating under clear skies and warming occurring under overcast skies. The effect of clouds during the 2 Dec 1980 CAO is unquantifiable since no radiation data were available.

4.3.2.9 Winds

Plots of boundary layer wind vectors are shown in Figures 4.35 to 4.37. Calculation of wind fields is based on an interpolation of the u (north-south) and v (east-west) fields separately. Pressure contours are superimposed over the vectors to show the relative contributions of geostrophy and ageostrophy to the mean flow. Observation level 1 indicates a downwind increase in wind speed and slight cyclonic curvature (i.e. winds backing downwind). The wind speed increase is likely a result of lower surface roughness over water than over land. In the northwestern part of the domain, cross-isobar angle is smallest, and ageostrophic flow is a minimum. In the southeastern portion of the domain, there is a significant ageostrophic component. Although surface friction is not the only influence

on ageostrophy it is a key aspect of lower boundary layer dynamics and increases the ageostrophic component as one moves towards the surface. Levels 2 and 3 exhibit similar characteristics to those at level 1 although the average wind speed at each successive level above the surface is slightly higher. Level 3 winds appear to increase through the center portion of the domain and then decrease to the south. This observation is suspect in view of the significantly larger errors in the south at level 3 than at level 2.

4.3.2.10 Surface Stress

Reynold's stress (τ) is plotted in the top panel of Figure 4.38 and is based on an interpolation of the momentum flux derived from the mean eddy correlation statistics ($\overline{u'w'}$) measured by the P-3 instrumentation. The largest values occur in the south (0.8 $\mathrm{kg\,m^{-1}s^{-2}}$) and decrease to the NE. The strongest gradient is in the northern part of the domain. There appears to be a weak negative correlation between τ and the ageostrophic wind component except in the SE corner of the domain where stress is relatively high and the wind is more ageostrophic.

Error estimates are plotted in the bottom panel of Figure 4.38. Most of the region is subject to an error of 0.1 $\mathrm{kg\,m^{-1}s^{-2}}$ with values increasing to the northwest and to the southeast.

Estimates of surface friction velocity are depicted in Figure 4.39. Values generally increase from north to south with a maximum (0.8 $\mathrm{ms^{-1}}$) occurring in the southwest. A minimum (0.35 $\mathrm{ms^{-1}}$) is located in the center of the domain with values increasing to the south more than they do to the north.

Over most of the domain, errors (bottom panel of Figure 4.39) do not exceed 0.2 $\mathrm{ms^{-1}}$. Largest values occur to the southeast and to the northwest.

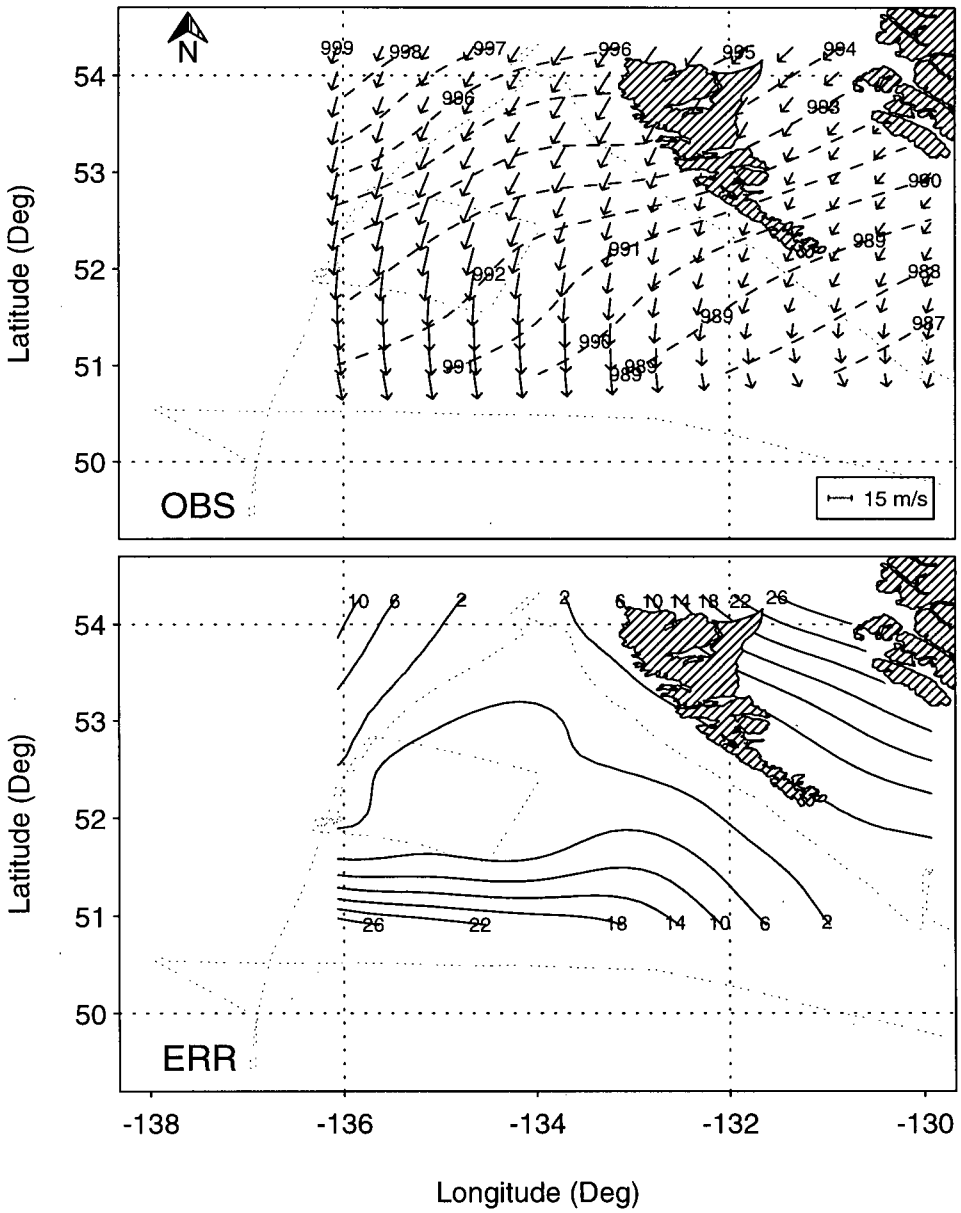

Figure 4.35: Interpolation estimates of wind vectors superimposed on pressure contours (top panel) at level 1 (50 m). Bottom panel depicts wind speed error estimates arising from both interpolation and instrumentation. Error estimates of pressure are not included. Contour intervals are 1 hPa in top panel and 4 ms^{-1} in bottom panel.

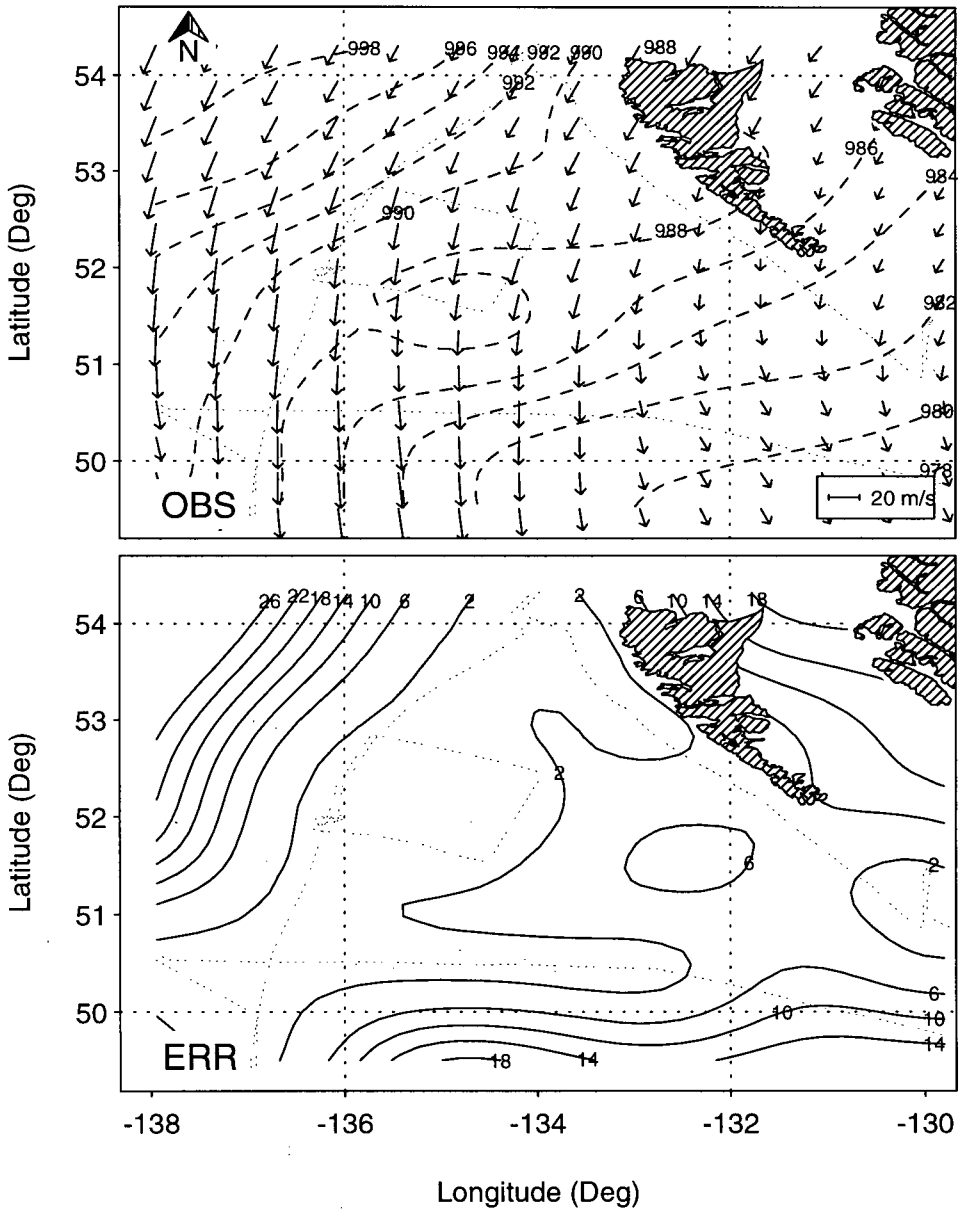

Figure 4.36: As in Figure 4.35 but for level 2 (90 m). Contour intervals are 2 hPa for pressure (top panel) and 4 ms^{-1} for wind speed error (bottom panel).

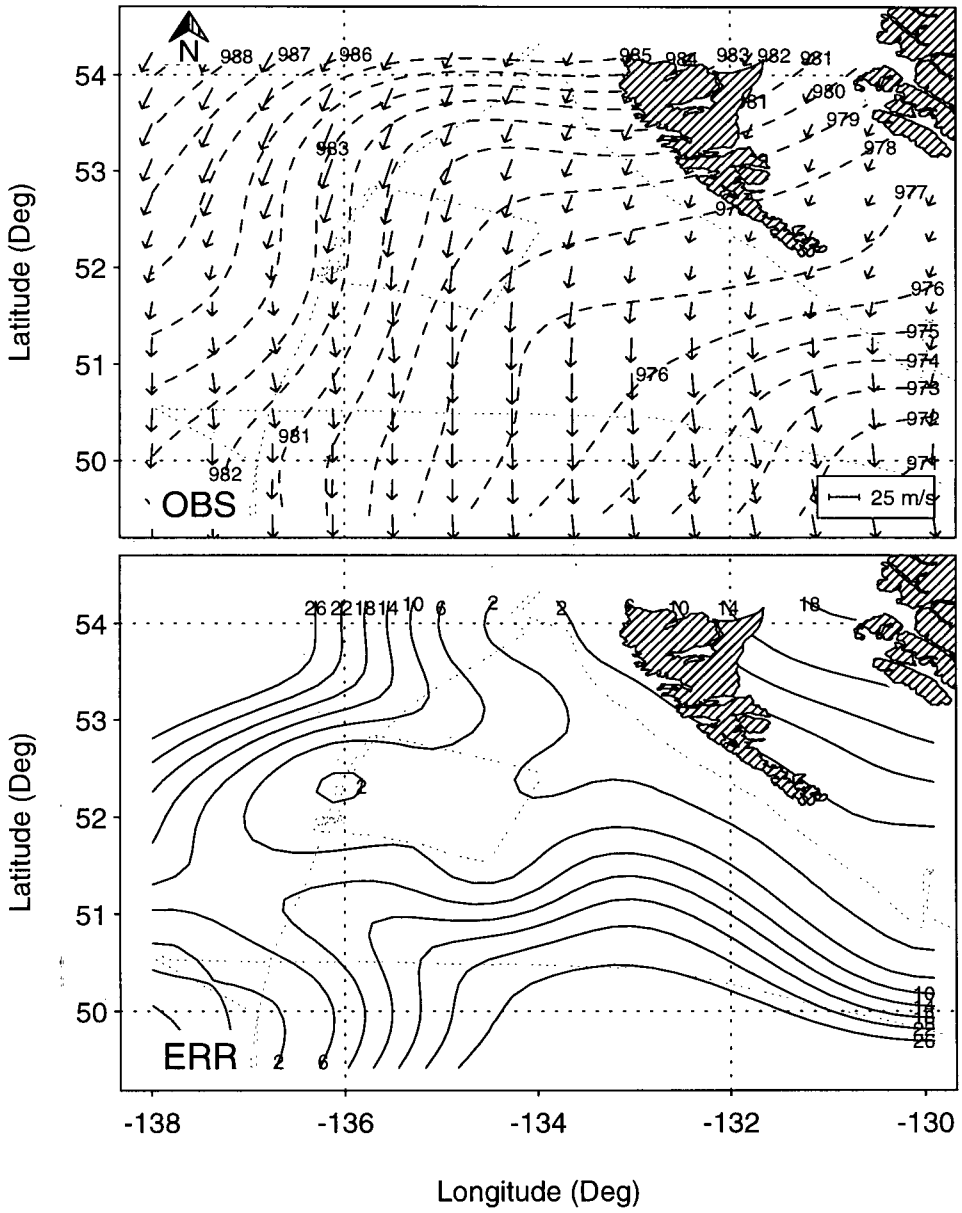

Figure 4.37: As in Figure 4.35 but for level 3 (150 m). Contour intervals are 1 hPa for pressure (top panel) and 4 ms^{-1} for wind speed error (bottom panel).

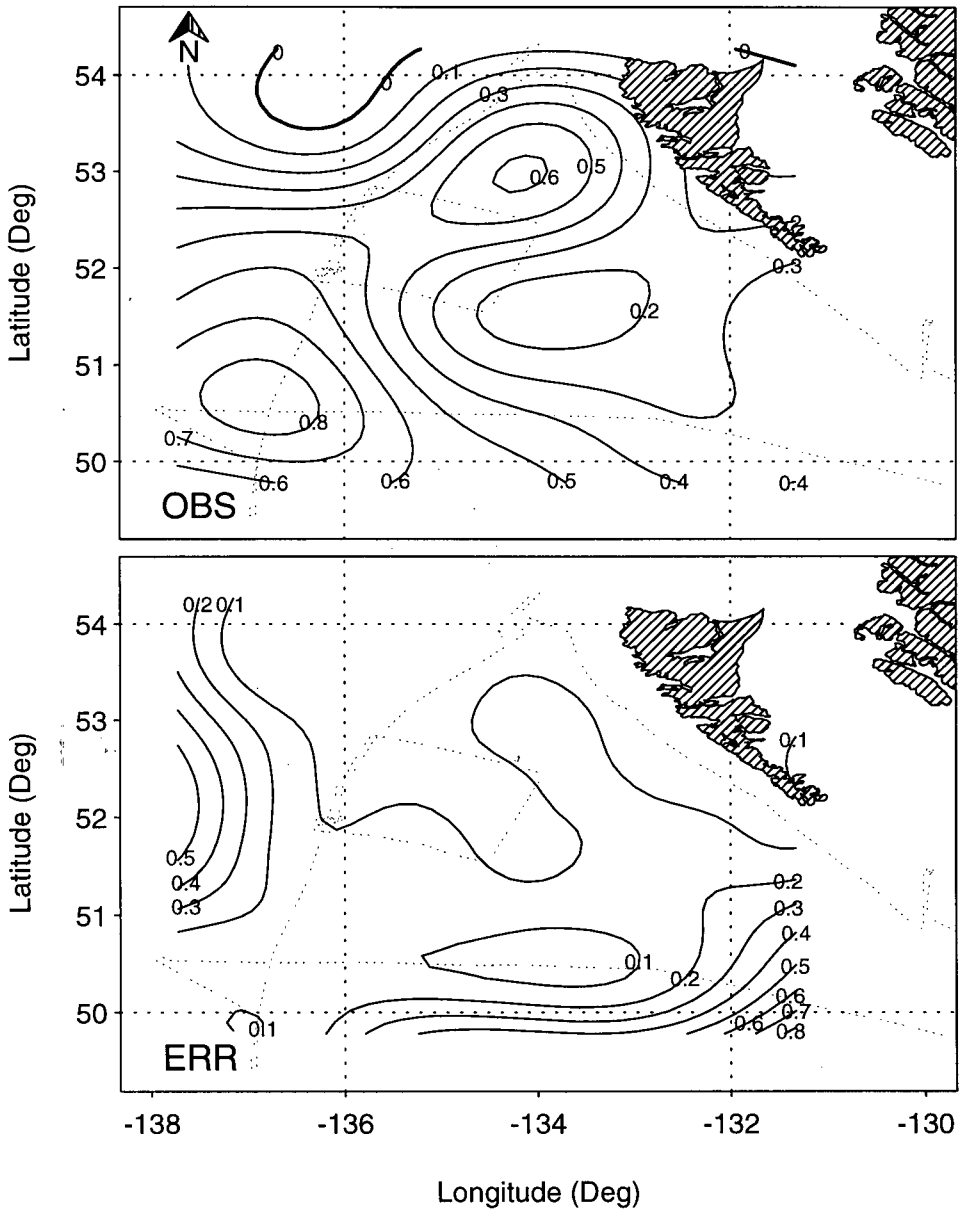

Figure 4.38: Interpolation estimates of surface Reynolds Stress (top panel) and error (bottom panel) arising from both interpolation and instrumentation. Units are in $\mathrm{kg\,m^{-1}s^{-2}}$ and the contour interval is 0.1 for both fields. Zero line in the top panel is darkened.

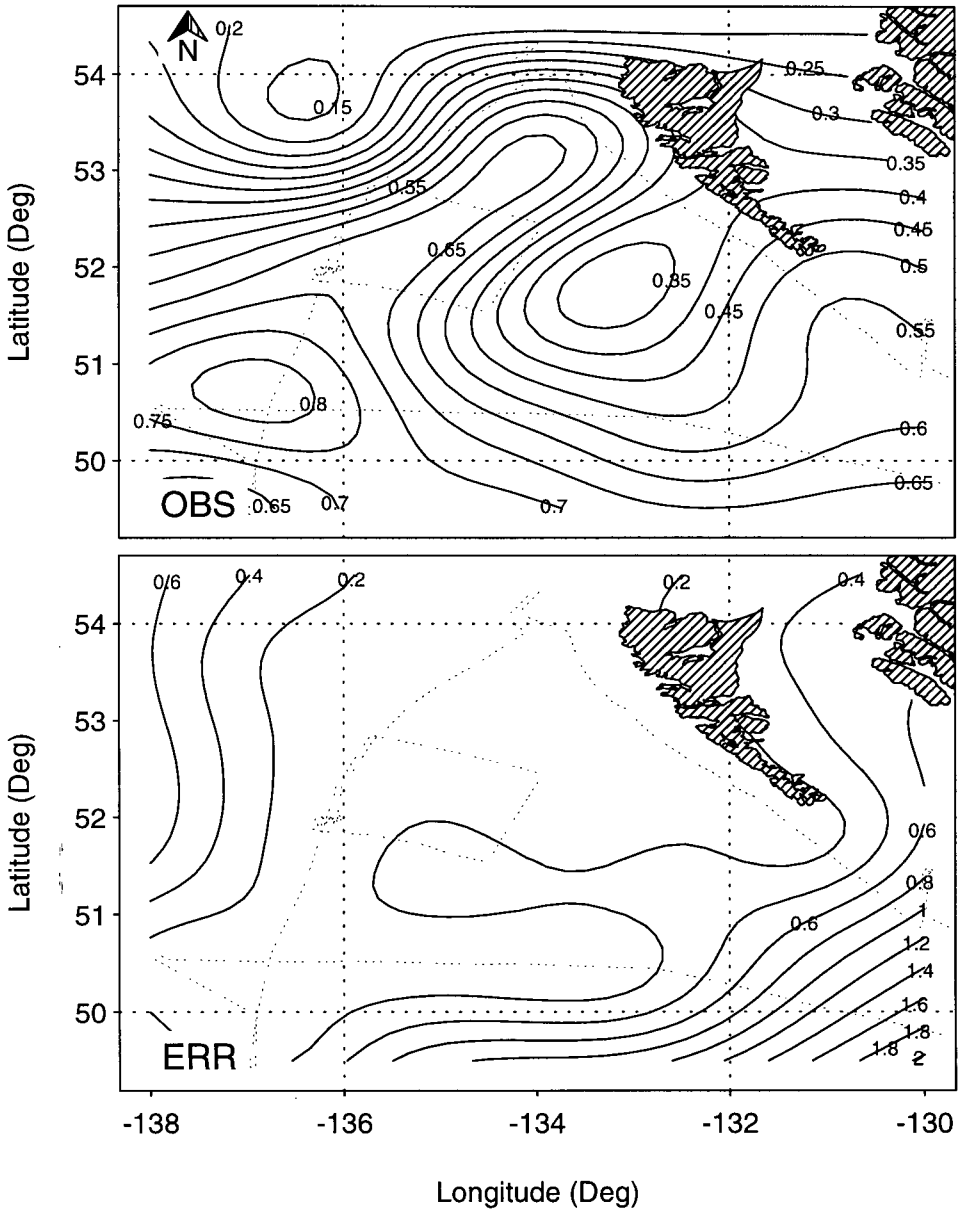

Figure 4.39: Interpolation estimates of surface friction velocity (top panel) and error (bottom panel) arising from both interpolation and instrumentation. Units are in ms^{-1} and the contour interval is 0.2 ms^{-1}.

4.4 Eddy Correlation vs. Bulk Determined Fluxes

During mission #6 the P-3 onboard instrumentation provided turbulence statistics of water vapor density (ρ_v), horizontal and vertical winds, and air temperature. Surface stress, and latent and sensible fluxes of heat were calculated based on averages of the covariance fluctuations. The biggest advantage of the eddy correlation method over other techniques is the direct nature of the measurements. The high cost of obtaining eddy correlation measurements however, often compels experimenters to use bulk methods.

A bulk scheme is used here to calculate surface sensible and latent heat fluxes, Reynolds stress and the Monin-Obukhov stability parameter in dimensional and non-dimensional form (L and z/L respectively). Estimates of z_i/L are also presented to allow for speculation on the existence of OLE and to permit comparison with other published results. Calculating observed bulk fluxes serves as a check for modelled bulk heat fluxes presented in Chapter 5. Results are then compared with previously determined eddy correlation values.

$Q_{H,E}$ and τ were calculated using the bulk equations in section 3.7. In order to determine values at a reference height of 10 m it was assumed that the wind profile was logarithmic. Using wind speeds and friction velocities obtained by the P-3 the log wind law was solved for z_o. The calculated z_o values were then substituted back into the same equation and the winds at 10 m were estimated. Although the surface layer appears to be slightly convective (see section 4.3.2) no buoyancy corrections to the profile (using $\Psi(\zeta)$) were made.

Estimates of surface sensible heat flux as determined by both eddy correlation (top panel) and bulk (bottom panel) methods are shown in Figure 4.40. Bulk values of Q_H are significantly larger than eddy correlation values. In the southeast region bulk values exceed eddy correlation values by up to a factor of 10 but in most other instances

eddy correlation values are exceeded by a factor of 3-4. The patterns exhibited by both schemes are similar in that an elongated ridge runs perpendicular to Moresby Island and is accompanied by a weak low to the southeast.

In Figure 4.41 eddy correlation (top panel) and bulk (bottom panel) estimates of Q_E are shown. Fewer similarities exist between observed patterns save the order of 3-4 difference in magnitude between the schemes. A maximum of 400 $\mathrm{Wm^{-2}}$ in the southwest region of the bulk panel coincides closely with a maximum of 260 $\mathrm{Wm^{-2}}$ in the eddy correlation panel. The eddy correlation maximum occurs just southeast of the bulk one. A relatively strong gradient runs perpendicular to the Queen Charlotte Islands in the bulk panel while a similar gradient occurs in the eddy panel but starts further to the northwest (perpendicular to Graham Island) and in the center of the domain. It then jogs south and aligns itself closely with the bulk gradient. A minimum of 80 $\mathrm{Wm^{-2}}$ occurs in the eddy panel just southwest of Moresby Island but a similar minimum is not found in the bulk panel.

Reynolds stress (τ) is shown in the top panel (eddy correlation) and bottom panel (bulk) of Figure 4.42. Horizontal distributions for both methods exhibit some comparable features. The relative maximum (0.8 $\mathrm{kg\,m^{-1}s^{-2}}$) in the top panel corresponds in the bulk panel to a maximum (0.55 $\mathrm{kg\,m^{-1}s^{-2}}$) just to the north. Also, two minima (0.6 $\mathrm{kg\,m^{-1}s^{-2}}$ (eddy),0.35 $\mathrm{kg\,m^{-1}s^{-2}}$ (bulk)) coincide closely just southwest of Graham Island. Bulk estimated values are smaller than eddy estimates by about a factor of 2 over most of the domain.

The large differences between eddy and bulk determined surface fluxes of heat and momentum may in part be due to the calculation of the roughness length using the log law. Using wind speeds measured by the P-3, z_o values were determined assuming neutrality. Based on this assumption, calculated z_o values had an average magnitude of 0.1-1 cm. Using Charnock's relation for z_o resulted in similar values as did applying a

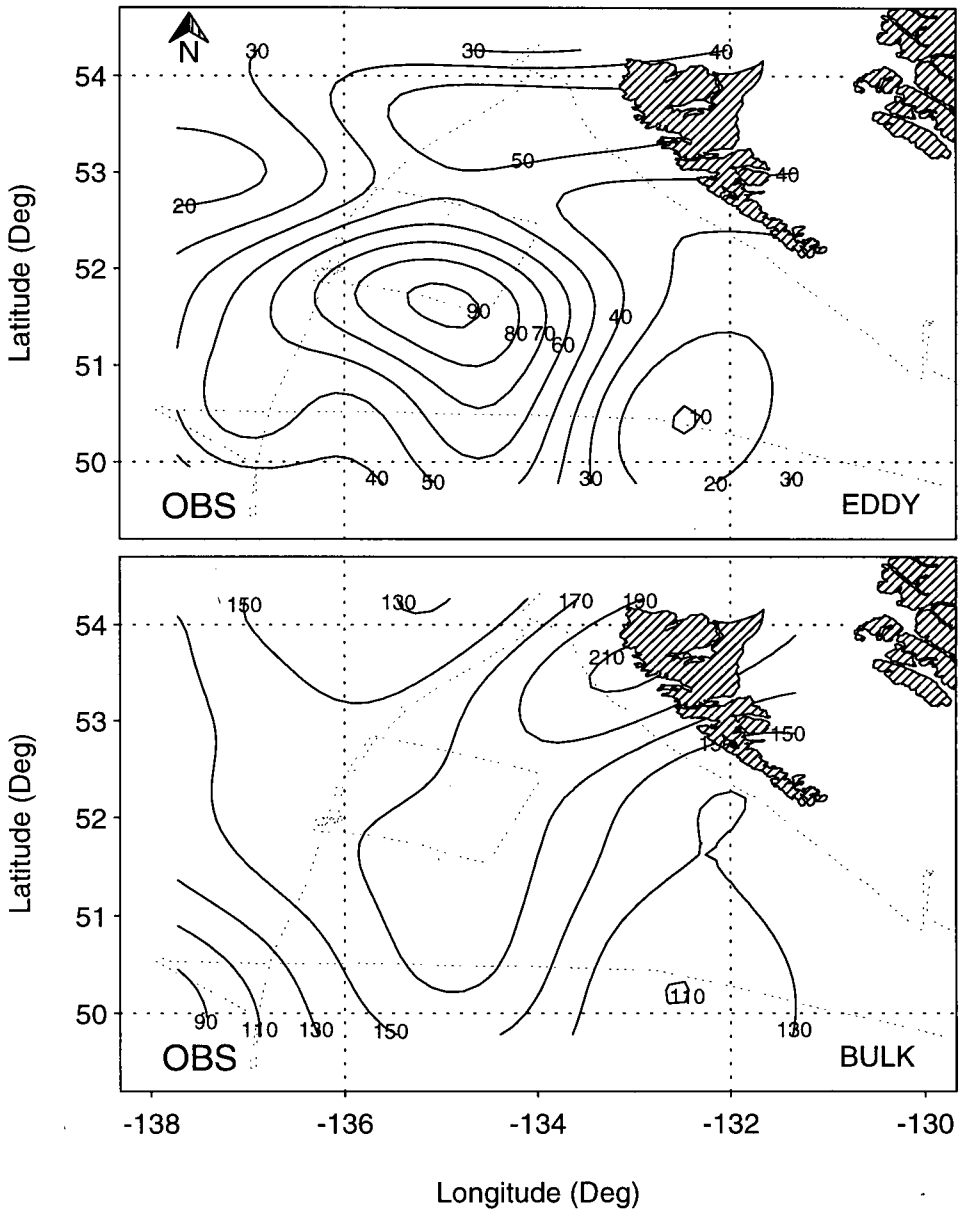

Figure 4.40: Interpolation estimates Q_H calculated using both eddy correlation statistics (top panel) and a bulk aerodynamic model (bottom panel). Contour intervals are 10 Wm^{-2} in the top panel and 20 Wm^{-2} in the bottom panel.

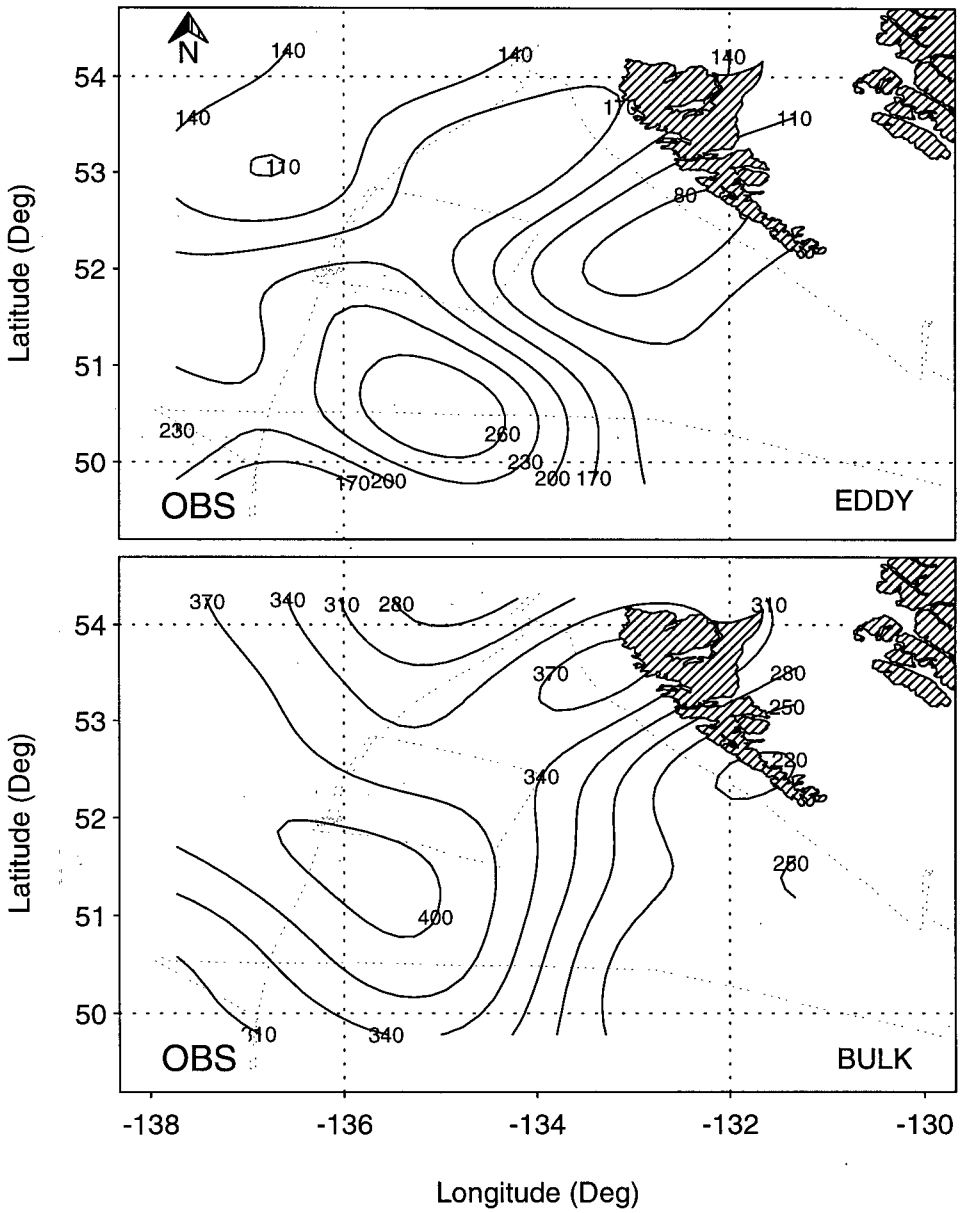

Figure 4.41: Interpolation estimates of Q_E calculated using both eddy correlation statistics (top panel) and a bulk aerodynamic model (bottom panel). Contour interval is 30 Wm^{-2} for both fields.

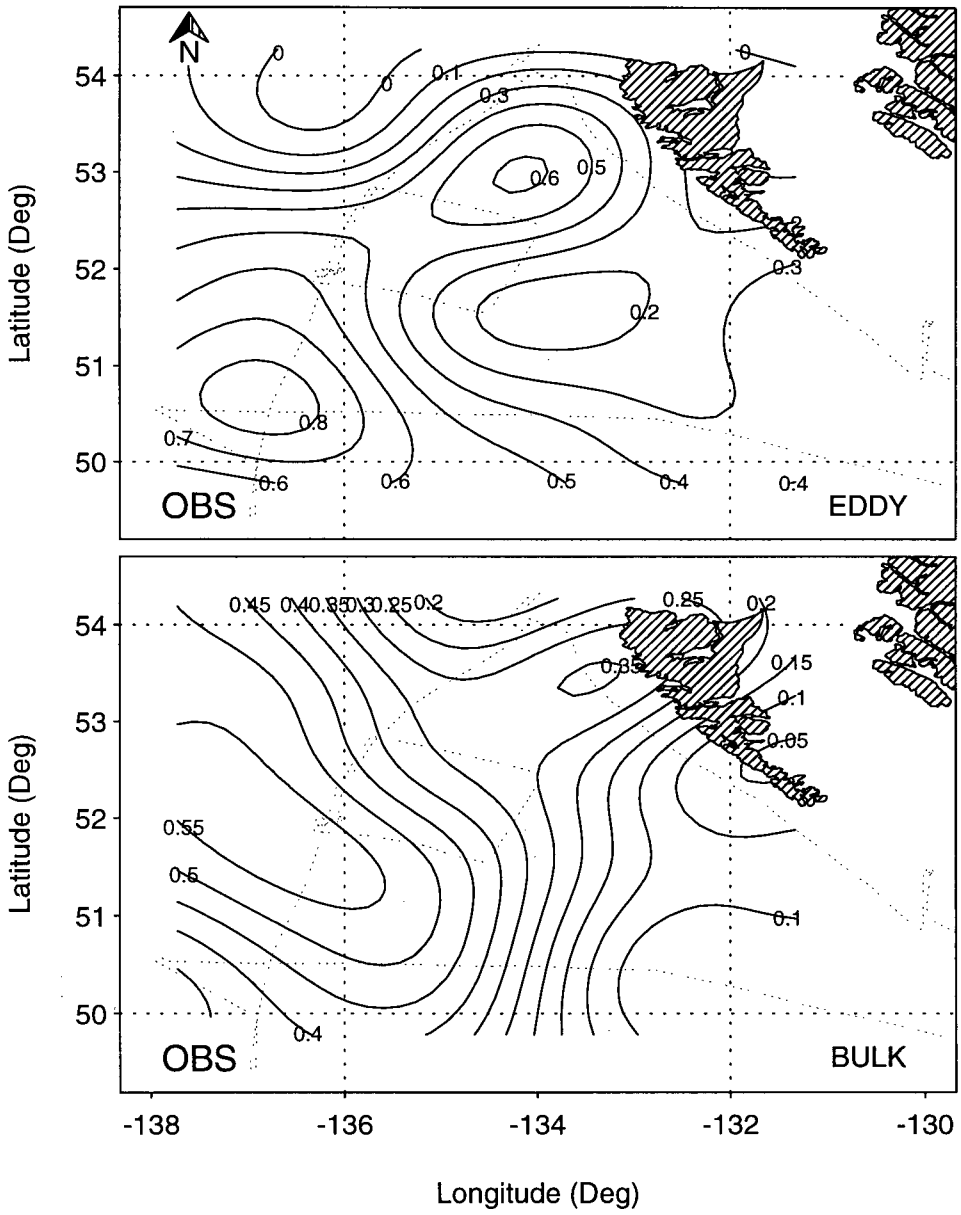

Figure 4.42: Interpolation estimates of τ calculated using both eddy correlation statistics (top panel) and a bulk aerodynamic model (bottom panel). Contour intervals are 0.1 $\mathrm{kg\,m^{-1}s^{-2}}$ in the top panel and 0.05 $\mathrm{kg\,m^{-1}s^{-2}}$ in the bottom panel.

buoyancy correction. Chou (1993) compared four bulk schemes with eddy correlation fluxes measured at the 50 m flight level over the western Atlantic ocean during cold air outbreaks. He found that the fluxes estimated by the four bulk schemes were in fairly good agreement with those of the eddy correlation method. All of the schemes used stability dependent transfer coefficients and employed the viscous interfacial-sublayer model of Liu *et al.* (1979). It remains unclear what is causing the large discrepancy between heat fluxes determined using the two parameterizations.

Eddy and bulk estimates of L are shown in the top and bottom panels of Figure 4.43 respectively. Smoothing radii (see Appendix B) of 330 km and 280 km were applied to eddy and bulk fields respectively. Eddy correlation estimates are larger than bulk estimates by a factor of 3 over most of the domain. Values in both panels increase from northeast to southwest ranging from -100 to -1300 meters (eddy) and from -50 to -450 meters (bulk).

Plots of eddy correlation and bulk z/L (z=10 m) are shown in the top and bottom panels of Figure 4.44 respectively. Fields of both eddy and bulk z/L were determined from interpolated L values.

Eddy correlation values range from -0.1 in the northeast and southeast portions of the domain to -0.02 in the southwest region. The gradient is oriented SW-NE in the north and becomes W-E in the south. The distribution suggests increasing stability to the south and southwest.

The bulk model (bottom panel) reveals a somewhat similar z/L pattern. Values range from -0.2 in the northeast to -0.04 in the southwest. The gradient is oriented SW-NE over much of the domain. Gradients in the bulk panel are strongest in the north and ease considerably to the southwest. Gradients are also moderately weaker than eddy correlation gradients. Bulk values are generally smaller than eddy values by a factor of 2. Both plots suggest increasing stability to the south and southwest, but the entire region

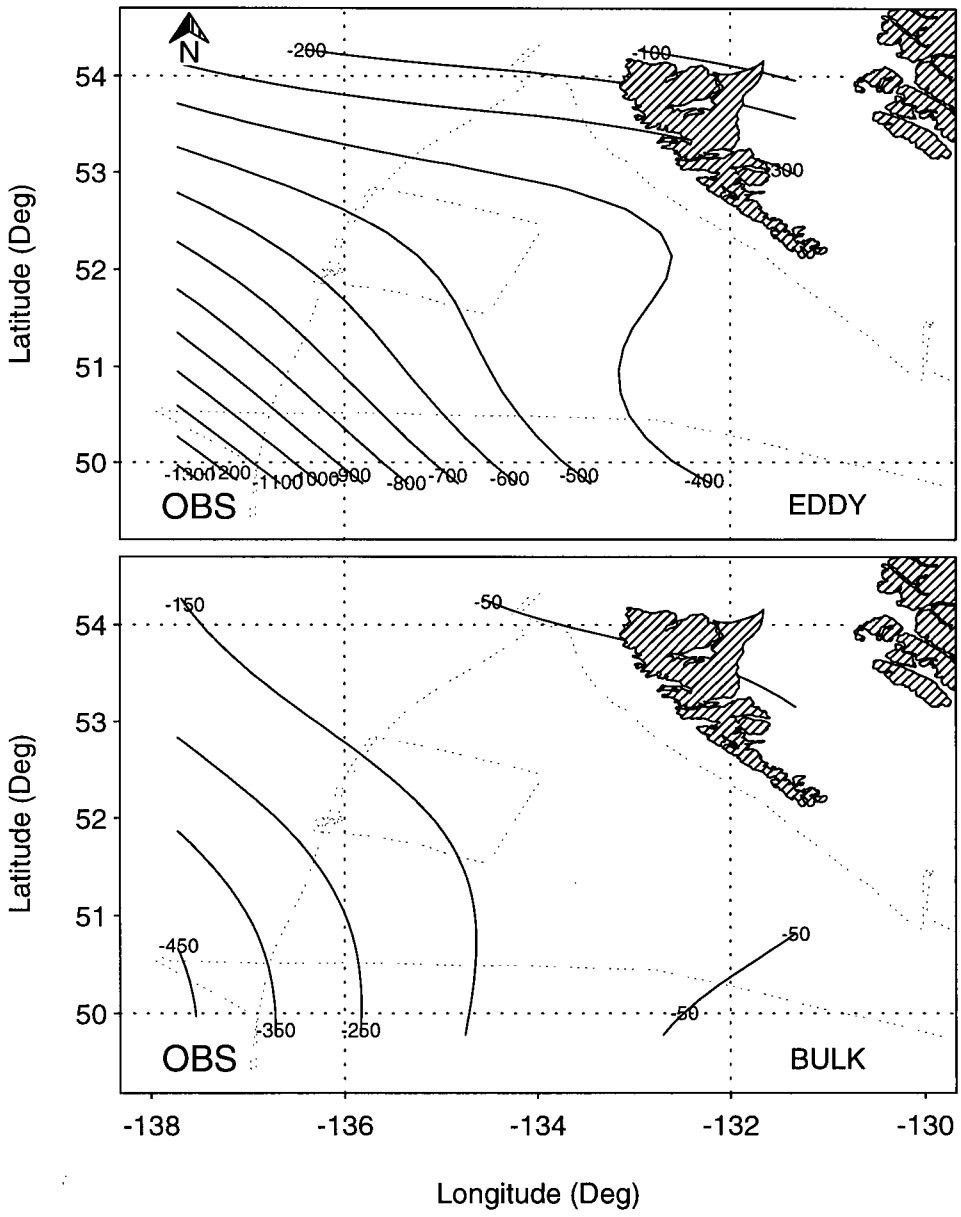

Figure 4.43: Interpolation estimates of Monin-Obukhov length (L) calculated using both eddy correlation statistics (top panel) and a bulk aerodynamic model (bottom panel). Contour interval is 100 m.

is characterized by unstable stratification at lower levels.

A downwind stability increase at lower levels may not be supported by the temperature profiles in section 4.3.1 but upper level temperature profiles did show increasing stability downwind. Miura (1986) found that during a number of CAOs the atmosphere was unstable from the surface up to the level of 200–300 m and neutral or slightly stable in the upper layer up to the inversion base. He also observed that temperature profiles downstream were more stable than those in the upstream region. The results of this study corroborate the findings of Miura.

In the initial stages (just offshore) of MABL modification, sea-air temperatures are large, thus promoting an unstable convective surface layer and large vertical transfers of sensible heat. As one proceeds downwind, sensible heat fluxes will decrease as sea-air temperature differences decrease (assuming that wind speeds also decrease or at least remain constant) and the surface layer will reach neutral or even slightly stable stratification. Upper boundary layer stability will be influenced by OLE and by the near surface energy exchanges, however the point at which the upper MABL becomes modified to the same extent as the surface layer does, will be further downstream. As surface layer modification proceeds downwind, the influence of convective overturning is propagated to higher levels in the boundary layer. The presence of OLE should expediate the transformation.

4.5 Variance and Turbulence Kinetic Energy

The velocity variance components ($\sigma_{u,v,w}$) can confirm or deny similarity predictions and elucidate the horizontal turbulence structure in the surface layer. If MOST scaling is correct the nondimensional variances formed by using u_*, θ_* and q_* should be universal functions of ζ. In neutral conditions they should be constants independent of height.

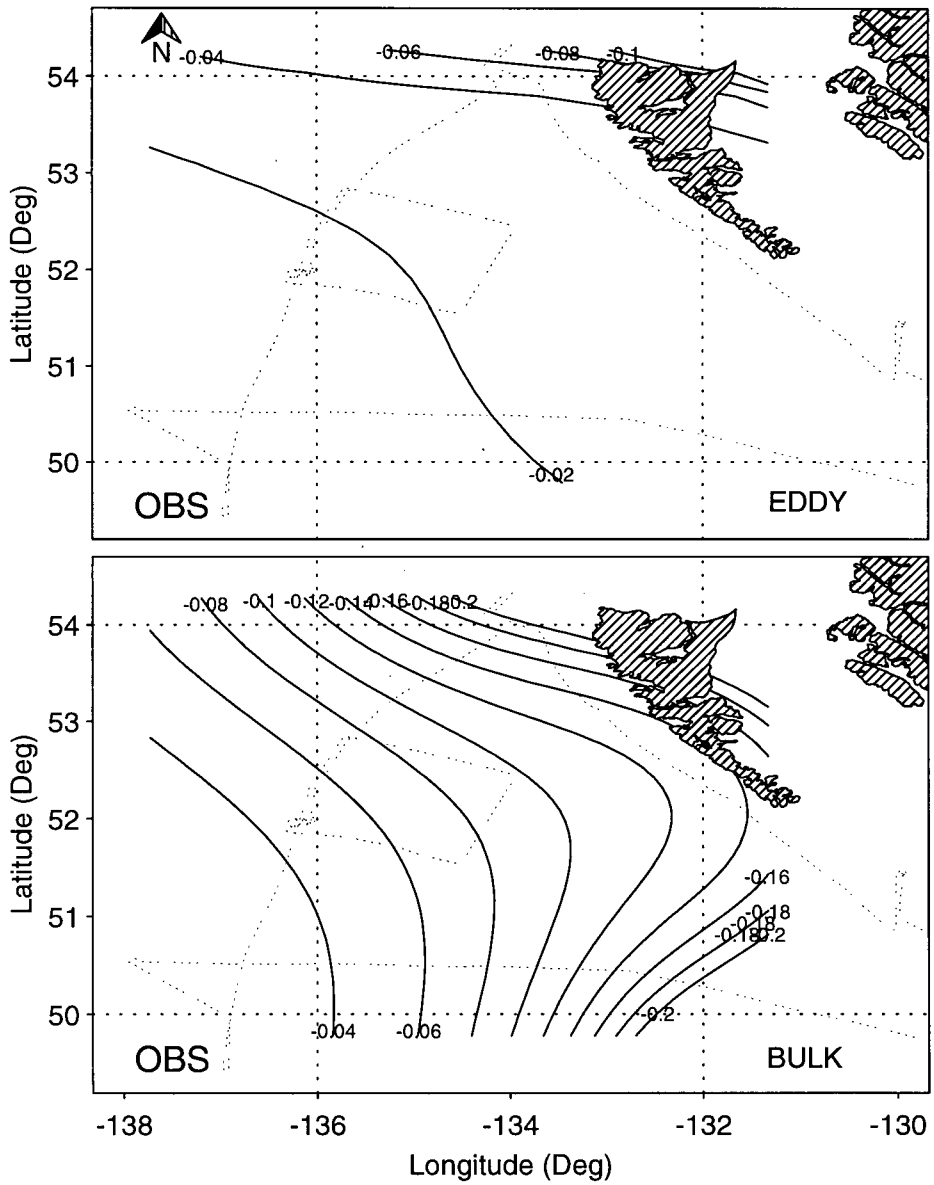

Figure 4.44: Interpolation estimates of z/L calculated using both eddy correlation statistics (top panel) and a bulk aerodynamic model (bottom panel). Contour interval is 0.02.

Values of the velocity ratios ($\sigma_{u,v,w}/u_*$) over flat terrain and under neutral conditions are typically 2.4, 1.9 and 1.25 for u, v and w respectively (Garratt, 1994). Average values observed in this study were 2.6, 2.5 and 2.0. Differences between the horizontal components and the vertical component are not as large as those between the Garratt values. Surface layer turbulence during the 2 Dec CAO was therefore less anisotropic than is typically observed. Wayland and Raman (1994) noted similar characteristics in two Atlantic CAOs. In their study they attributed the difference between neutral and non-neutral conditions to stronger convection and baroclinicity. Concomitantly the surface layer in this study is slightly unstable and one would expect that return-to-isotropy would be proportional to the degree of instability in some fashion.

Panofsky *et al.* (1977) proposed the following relationship for σ_w/u_*:

$$\sigma_w/u_* = (1.95 - 5.85\zeta)^{1/3} \tag{4.28}$$

A better fit to the STREX data is:

$$\sigma_w/u_* = (1.37 - 15.6\zeta)^{1/3} \tag{4.29}$$

based on a visual fit. The above relationships (4.28 and 4.29) are shown in Figure 4.45 accompanied by σ_w/u_* data.

The STREX relationship is steeper thus implying a more sensitive dependence of velocity variance on boundary layer stability.

Observations by others (e.g. Arya, 1988) reveal that $\sigma_{u,v}$ often do not follow MOST scaling. A proposed cause is the influence of low-frequency eddies, either through boundary layer shear instabilities or through convection. This explanation holds additional merit for CAO MABLs which have a propensity to contain large scale eddy circulations. A more appropriate scaling height for horizontal wind variances is boundary layer top z_i.

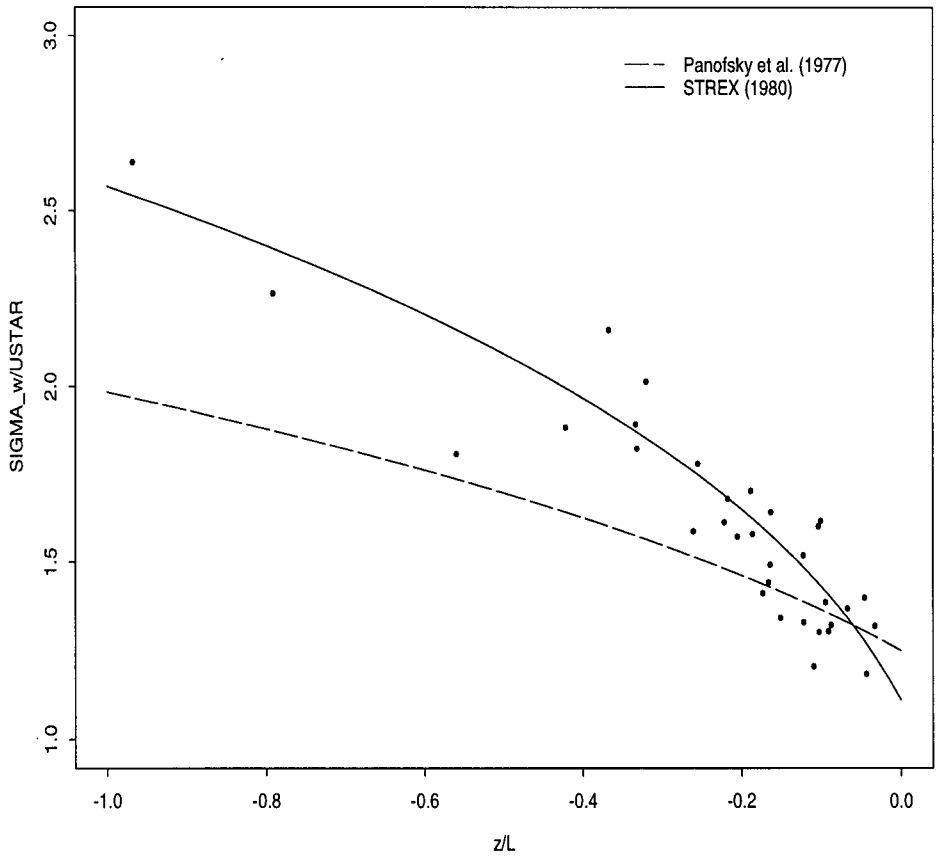

Figure 4.45: Normalized σ_w as a function of ζ. Dashed line is relationship found by Panofsky *et al.* (1977) and solid line is based on STREX mission #6 data.

Panofsky *et al.* (1977) derived the following relationship for the horizontal components in unstable conditions:

$$\sigma_u/u_* \approx \sigma_v/u_* = (12 - .5z_i/L)^{1/3} \tag{4.30}$$

Data from this study appears in Figure 4.46. Three outlying points were not included in the figure. The relationship of Panofsky *et al.* (1977) is shown by the dashed line. A better fit to the data shown by the solid line is:

$$\sigma_u/u_* \approx \sigma_v/u_* = (1 - 2.2z_i/L)^{1/3} \tag{4.31}$$

Again the STREX relationship is steeper. Discrepancies between the data here and the relationship of Panofsky *et al.* (1977) may be real but could also be due to inaccurate estimates of boundary layer height. Overall the scaling is acceptable.

An investigation of the horizontal distribution of velocity variance ratios (σ_u/σ_v, σ_u/σ_w, σ_v/σ_w should elucidate any downwind trends in turbulence anisotropy. The study domain was divided into three sections, with the first (North) encompassing the 8 most northerly of the 36 turbulence data points, the next (Middle) spanning 9 of the data points in the middle of the domain and the last (South) covering the remaining points furthest south.

The points within each region were averaged for each of the three ratios and compiled into a table of values shown in table 4.2.

The largest ratios are found in σ_u^2/σ_w^2 although there is no significant downwind variation. Values remain near 2 in all three regions. The smallest ratios are in σ_u^2/σ_v^2 with values ranging from 1.42 to 1.14. σ_v^2/σ_w^2 values are intermediate between the other two ratios but are closer to σ_u^2/σ_w^2 values than those of σ_u^2/σ_v^2. An average calculated in any one region did not differentiate between crosswind and downwind variations that

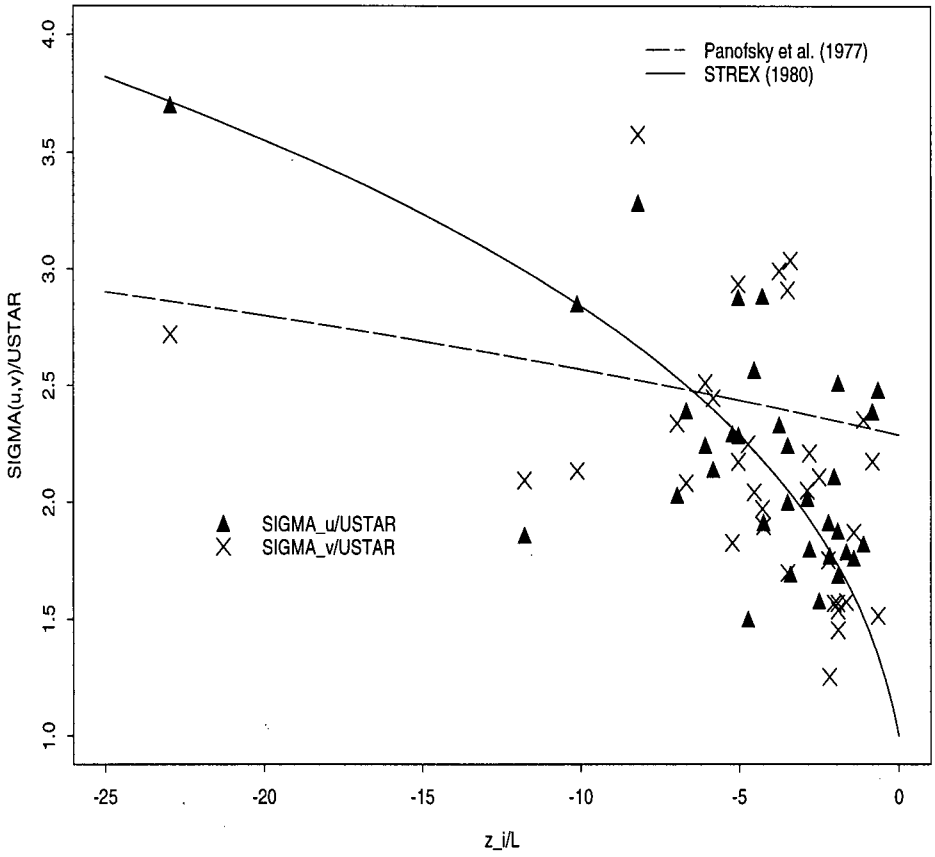

Figure 4.46: Normalized $\sigma_{u,v}$ as a function of z_i/L. Dashed line is relationship found by Panofsky *et al.* (1977) and solid line is relationship determined from STREX data.

SECTION	σ_u^2/σ_v^2	σ_u^2/σ_w^2	σ_v^2/σ_w^2
North	1.26	2.05	1.87
Middle	1.42	2.16	1.73
South	1.14	1.94	1.95

Table 4.2: Table of ratios of the three velocity variances for the three regions described in the text.

coexisted within that region. It is possible but not likely that this treatment would result in the disguising of a downwind increase or decrease in variance.

Turbulence kinetic energy per unit mass $\overline{e}$ (TKE/mass) was calculated using the following equation:

$$\overline{e} = \frac{1}{2}(\overline{u'^2} + \overline{v'^2} + \overline{w'^2}) \tag{4.32}$$

Estimated values of $\overline{e}$ are shown in Figure 4.47. There is a systematic downwind increase in $\overline{e}$ on the western side of the domain. Values increase from 3 Jkg^{-1} (North) to a maximum of 10 Jkg^{-1} (Southwest corner). Further east, conditions are reversed with values decreasing downwind. Based on the data distribution, more confidence should be placed on a downwind increase which is also consistent with increasing windspeeds downwind. Diurnal variations in TKE produce a peak at $\approx$ 2 pm local time (see Stull, 1988, pg. 46). This time variation may be contributing weakly to the W-E $\overline{e}$ decrease in the southern portion of the domain since the flight was nearing its conclusion in the afternoon and $\overline{e}$ values were presumably decreasing.

4.6 Spectral Analysis

Roll vortices in the MABL can often be revealed through spectral analysis (Hein and Brown, 1988). A roll manifests itself as a spike in the energy spectrum of the velocity, and possibly the moisture and temperature records at the roll frequency. Vortex streets are typically aligned parallel to the mean flow with a 0 to 15 degree offset to the left or right depending on the stability (see Section 2.4.2). The structures are observed in the crosswind component of the record and require a transect of the velocity field in the crosswind direction. The averaging time (T) must be much less than λ/V, where λ is the eddy wavelength and V is the aircraft speed. For λ = 10 km, T << 100 sec. The

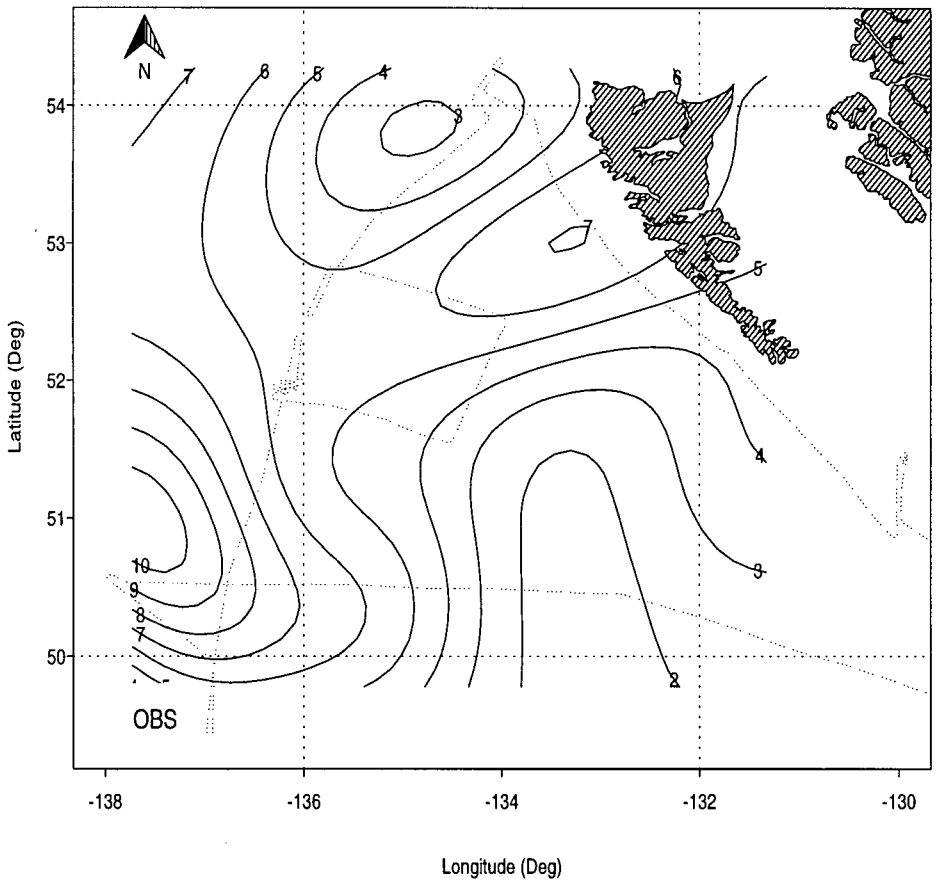

Figure 4.47: Interpolation estimates of TKE. Units are J Kg^{-1} and contour interval is 1 J Kg^{-1}.

averaging time for the aircraft data used here is 20 sec which should be small enough. Another stipulation is that the leg length $l >> \lambda$. In this study, the P-3 flew a total of 4 crosswind legs and 3 alongwind legs as shown in Figure 4.48. Only 4 legs were analysed (1 [423 km], 4 [342 km], 5 [168 km] and 6 [230 km]) due to the inadequate length of the others. Two of the alongwind legs (5 and 6) are long enough to allow for confident interpretation of features at small λ but features at $\lambda > 50$ km should be viewed with caution. Legs 5 and 6 were analysed to determine if energy peaks or significant features were present in the alongwind direction.

Confidence intervals (C.I.) were determined, based on the degrees of freedom associated with a χ^2 approximation of the spectral density estimate at each Fourier frequency. With no smoothing, padding or tapering of the time series there are $\nu = 2$ degrees of freedom. The degrees of freedom increases with the amount of smoothing. The smoothing used here was a running average (Daniell Window) run twice using the two points on either side of the point being averaged. The associated degrees of freedom is $\nu = 11$. Based on a table of the limits of a χ^2 distribution, the 95% C.I.:

$$\chi^2_{0.975;11.35968} = 4.23 \qquad \chi^2_{0.025;11.35968} = 22.8292$$

If $S(f)$ is the spectral value then the 95% C.I. is:

$$\frac{DF}{\chi^2_{.025}} * S(f) \leq S(f) \leq \frac{DF}{\chi^2_{.975}} * S(f) \tag{4.33}$$

It is assumed implicitly that the distribution is both Gaussian and white (no correlation). Each time series was detrended by subtracting a least squares regression line from it. Tapering was done using a half cosine of 10% on each end of the series.

The spectrum is determined as follows. Let n be the length of the time series with or without padding. Let Δ be the sampling interval $= 1/freq$. An estimate of the power spectrum at discrete Fourier frequencies $f_k = k/n\Delta$ is found by forming the periodogram:

$$\tilde{S}(f_k) = \frac{1}{n} \mid \sum_{t=1}^{n} \tilde{x}_t \exp(-2\pi i f_k t) \mid^2 = \frac{n\Delta}{2}(A_k^2 + B_k^2), k = 0, 1, ..., n/2 \qquad (4.34)$$

where,

$\tilde{S}(f_k)$ = the spectral density at the Fourier frequency (f_k).

$\tilde{x}_t$ = the detrended and tapered time series.

A_k and B_k are the Fourier coefficients.

The discrete Fourier transform (DFT) sum in (4.34) is computed using a mixed radix Fast Fourier Transform (FFT) algorithm.

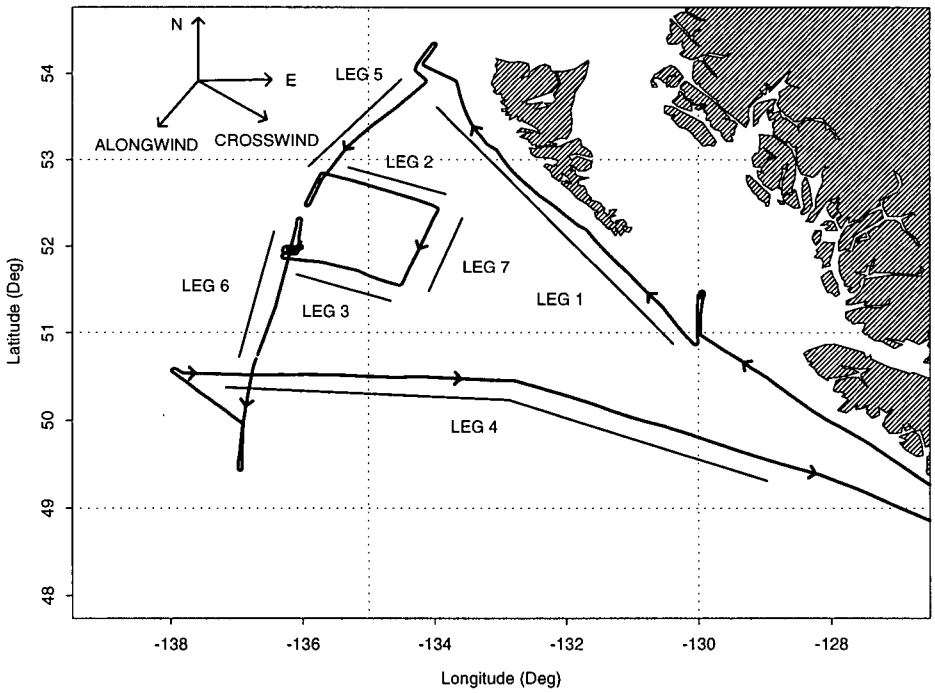

Figure 4.48: P-3 flight path and its partitioning into 7 distinct legs.

The data averaging time of 20 sec combined with the aircraft speed of 104 ms^{-1} correspond to a resolvable wavelength of 2 km. The time series data all fall within the

height range 50–150 m. For any one variable the abscissa limits were held constant so as to allow consistent comparison of spectra for all analysed legs.

Figures 4.49 to 4.52 show the spectra for the 4 analysed legs; 1 and 4 are crosswind while 5 and 6 are alongwind. In the leg 1 u spectrum, one peak appears at $\lambda \approx 9$ km with a secondary maximum at 7.5 km. Both of these wavelengths are absent in the v spectrum which exhibits a small peak near 15 km. The temperature spectrum is flat but q shows minor peaks at $\lambda \approx 17$ km and 7 km. Note that the upper wavelength axis limit for both leg 1 T_v and q corresponds to a leg length of only 260 km. Temperature and humidity records were truncated because of missing data values near the end of the leg. Leg 4 v and q spectra both exhibit strong peaks at 14 km, while the T_v spectrum is relatively smooth. Both leg 4 u and v components show a signal at $\lambda \approx 25$ km. This is a larger wavelength than observed in leg 1; however, if inversion base height is assumed to correspond to MABL height then the aspect ratios of rolls in legs 1 and 4 are 7.9 and 12.2 respectively. These observations agree with those by Miura (1986) of a downwind increase in roll aspect ratio during a CAO. Leg 5 u and v spectra show minor peaks at 9 km and 6 km respectively. The v peak may indicate the presence of mesoscale cellular convection that has been organized into rolls. There were a number of missing values in the leg 5 temperature and humidity records and therefore no spectra of these variables were computed. The leg 6 u spectrum shows a peak near 12 km while the v spectrum peaks at 18 km. There is also a strong peak in the q spectrum at 20 km while the T_v spectrum is flat. The peak at $\lambda = 20$ km in the leg 6 q spectrum may signify MCC.

Some evidence of rolls may be present in the satellite picture in Figure 4.53. The time of the image is 18Z 3 Dec 1980 which is 15 hours after the time of mission #6. The image was extracted from a photograph which covered much of the north Pacific ocean. A zooming procedure resulted in a larger image at the expense of limited resolution. Lineal patterns appear to be embedded in the solid stratocumulus cloud deck to the southwest

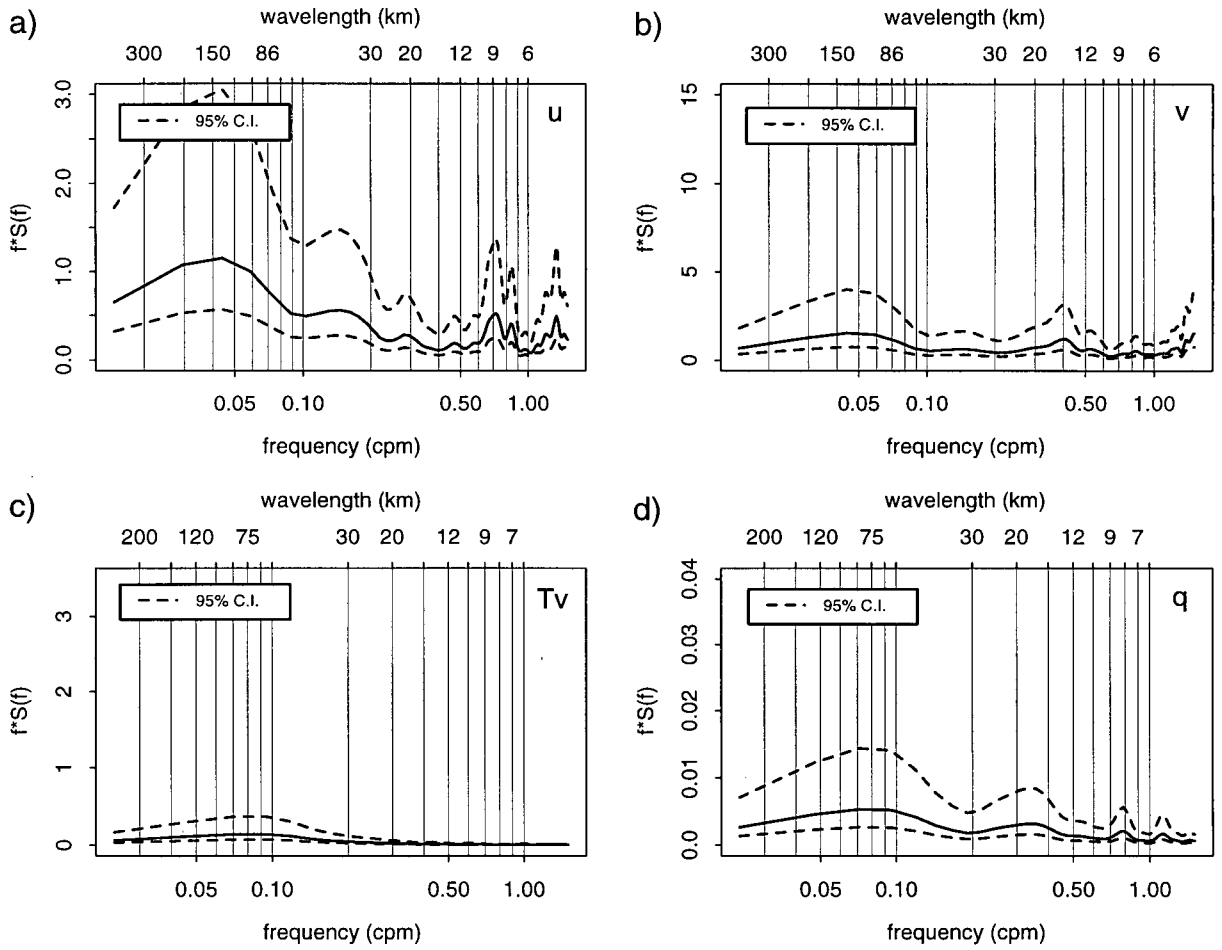

Figure 4.49: Leg 1 (crosswind) spectra of u, v, T_v and q. Vertical coordinate is normalized power multiplied by frequency. The upper horizontal coordinate is wavelength in km and the lower coordinate is frequency in cycles per minute. 95% confidence intervals are indicated in each plot by two dashed curves, above and below the solid spectral curve.

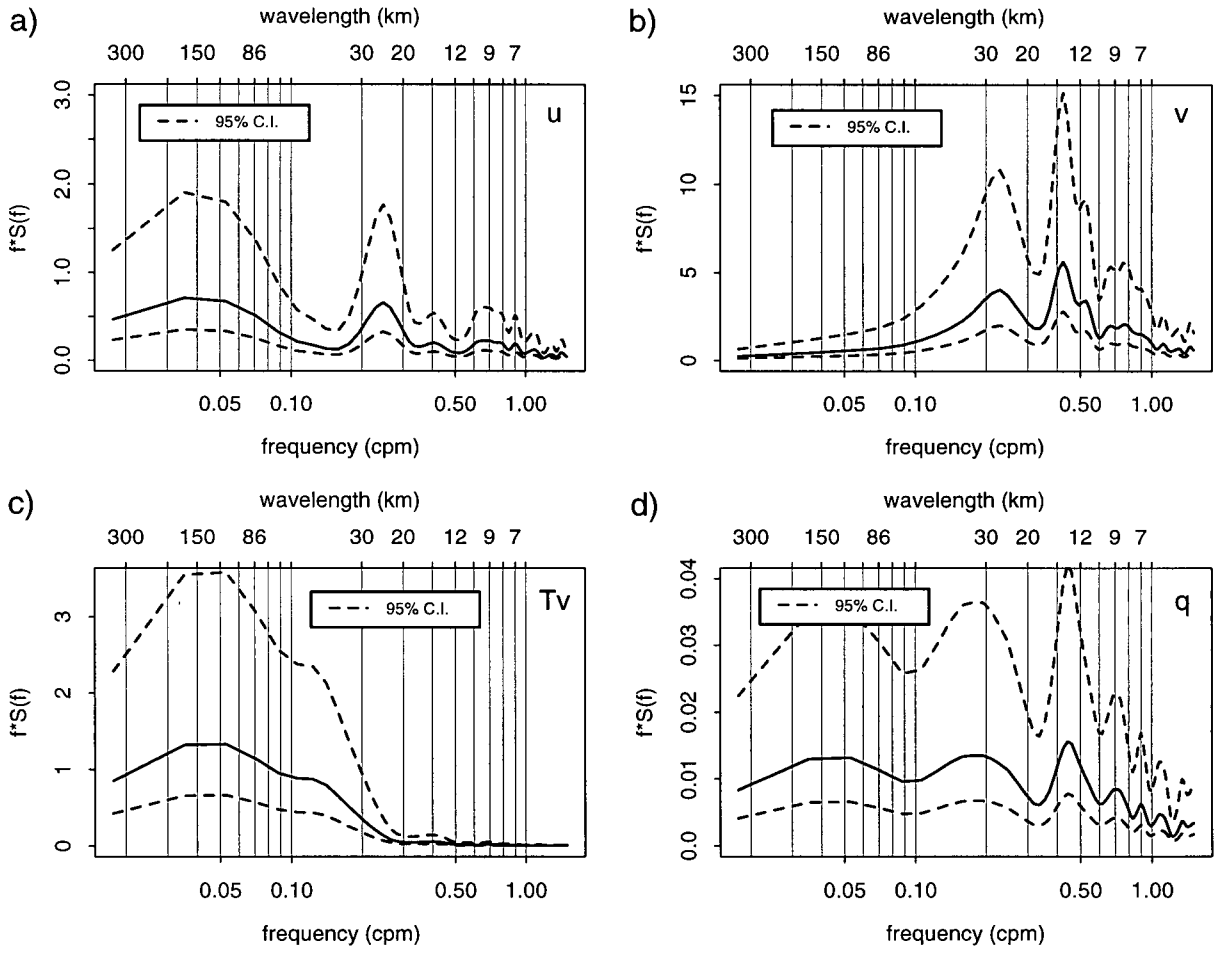

Figure 4.50: As in Figure 4.49 but for Leg 4 (crosswind).

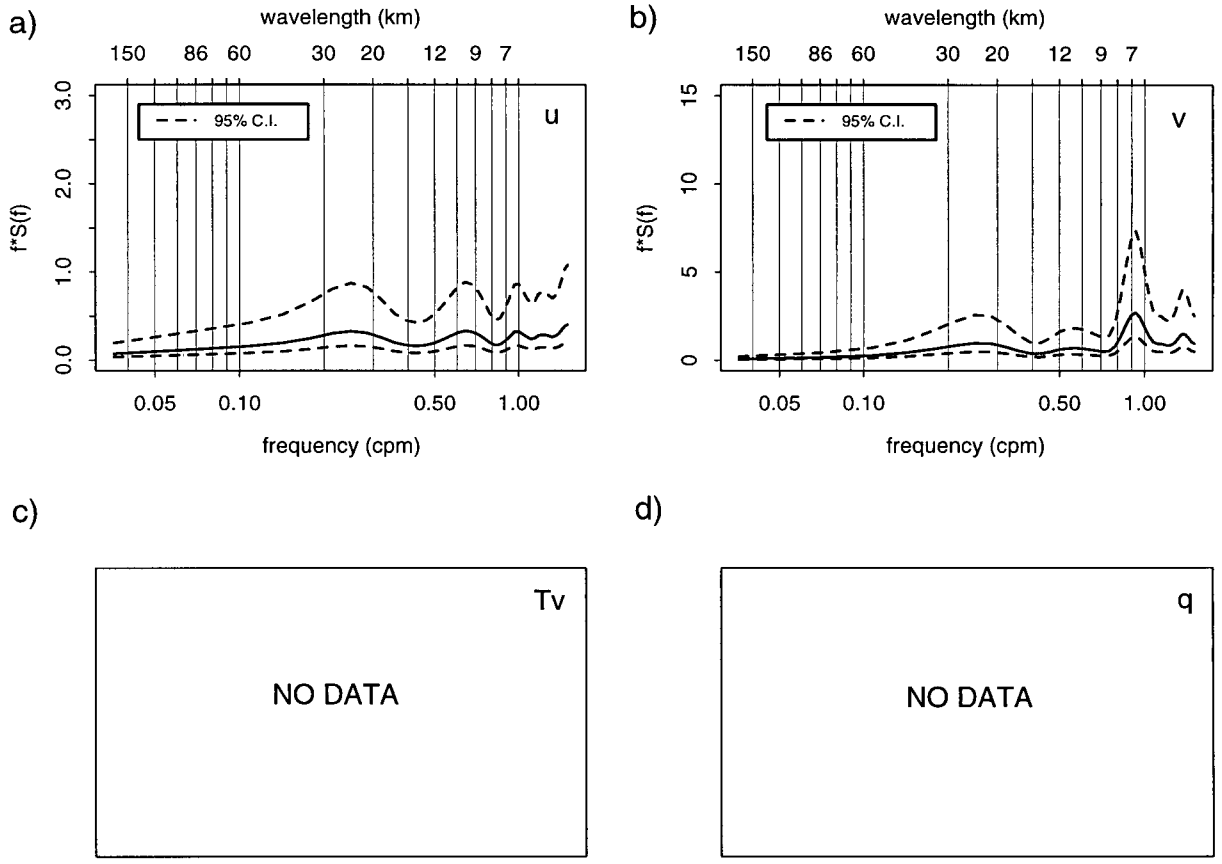

Figure 4.51: As in Figure 4.49 but for Leg 5 (alongwind).

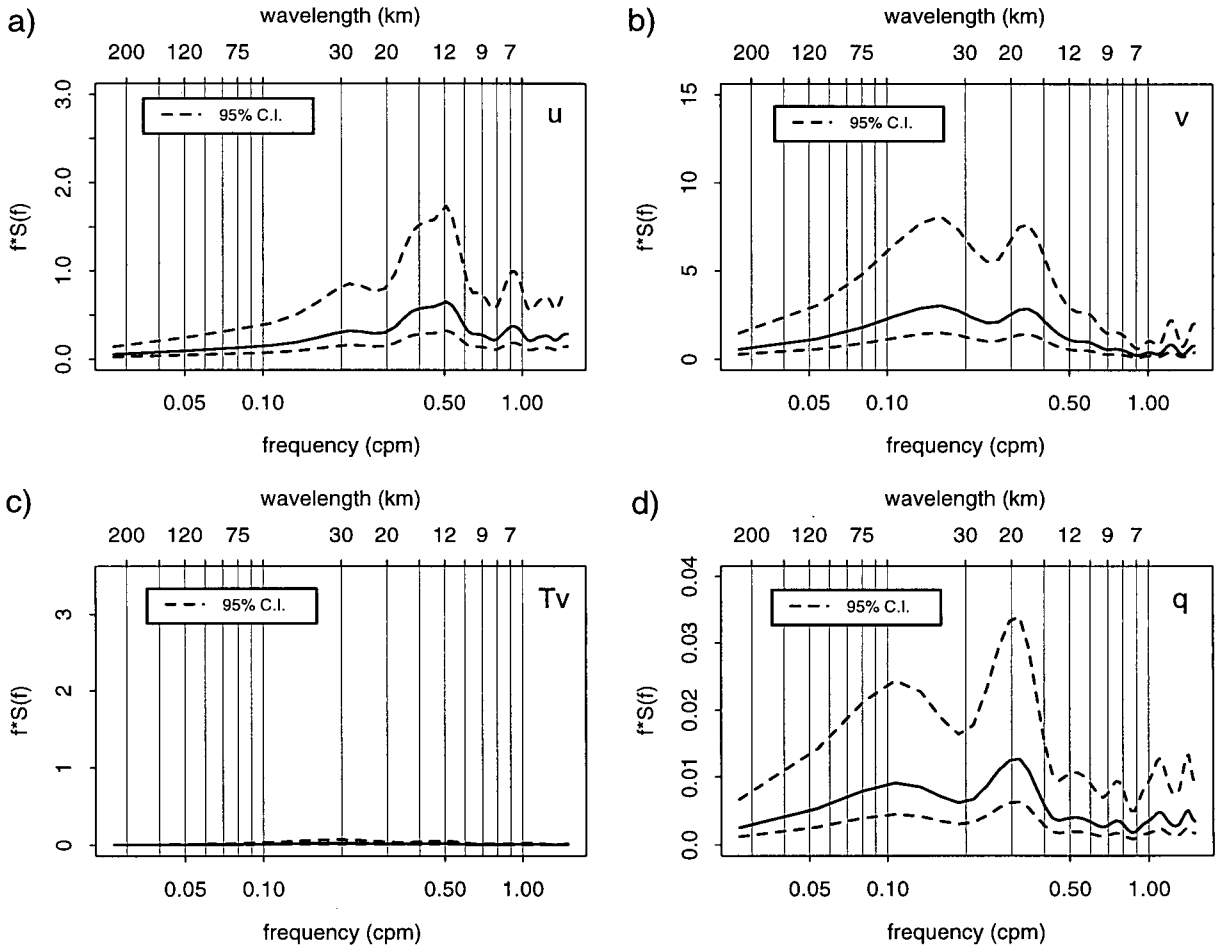

Figure 4.52: As in Figure 4.49 but for Leg 6 (along wind).

of the Queen Charlotte Islands. The roll scale of $\approx$ 100 km is considerably larger than the commonly observed scale of 5-20 km, but is similar in magnitude to the λ observed when "symmetric" instability is the driving mechanism for roll development (see section 2.4.2).

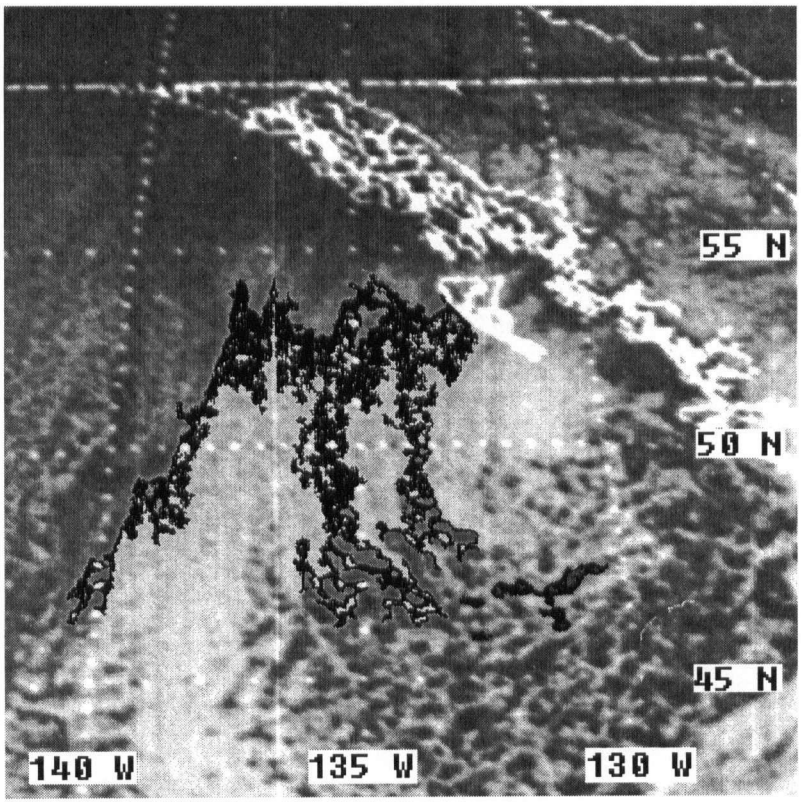

Figure 4.53: Enhanced GOES satellite image showing clouds over the STREX mission #6 study region at 18Z 3 Dec 1980. From AES satellite archives.

The area of transition from rolls to cellular convection is poorly defined. It is therefore possible that convective cells exist within the stratocumulus cloud deck but may be obscured by the prevailing cloud cover. There is a region of strong curvature in the lower central portion of the image where MCC is the primary feature. The observed cloud distribution suggests that convective processes are increasingly dominant in the downwind direction as stratus and stratocumulus cloud (relatively stable stratification)

have given way to convective cumulus cloud (unstable stratification).

4.7 The Role of Rolls

A number of studies have revealed that the presence of large eddy circulations in the MABL can be detected from atmospheric stability characteristics estimated using MOST (Deardorff, 1972; Grossman, 1982). In section 2.4.2 it was noted that moderately unstable conditions ($-25 < z_i/L < -5$) are conducive to roll development. Figure 4.54 shows estimates of ζ_i where z_is are the interpolated inversion heights shown in Figure 4.34 and L values are based on eddy covariances (top panel of Figure 4.43). Most of the study area contains ζ_i values between -24 and -3 with the gradient oriented SW-NE. The pattern is very similar to the one calculated for eddy covariance z/L, and the range of values lends support to the hypothesis that rolls exist within the study domain. Still, the roll development mechanism is unclear.

A necessary condition for the generation of inflection-point instability is an inflection point in both the u and v wind profiles (Brümmer *et al.*, 1992). There are no inflection points in the profiles in Figure 4.21 however the poor data quality makes such an observation inconclusive.

To determine conclusively what the driving instability mechanism is, it would also be necessary to obtain continuous vertical flux profiles. Again, profile information is inadequate or absent and no conclusions can be drawn. It is hypothesized that due to strong low level winds (20–25 ms^{-1}) and strong turbulent surface heat fluxes, both vertical wind shear (IPI) and thermal convection (CI) are acting together and to varying degrees to produce roll type circulations.

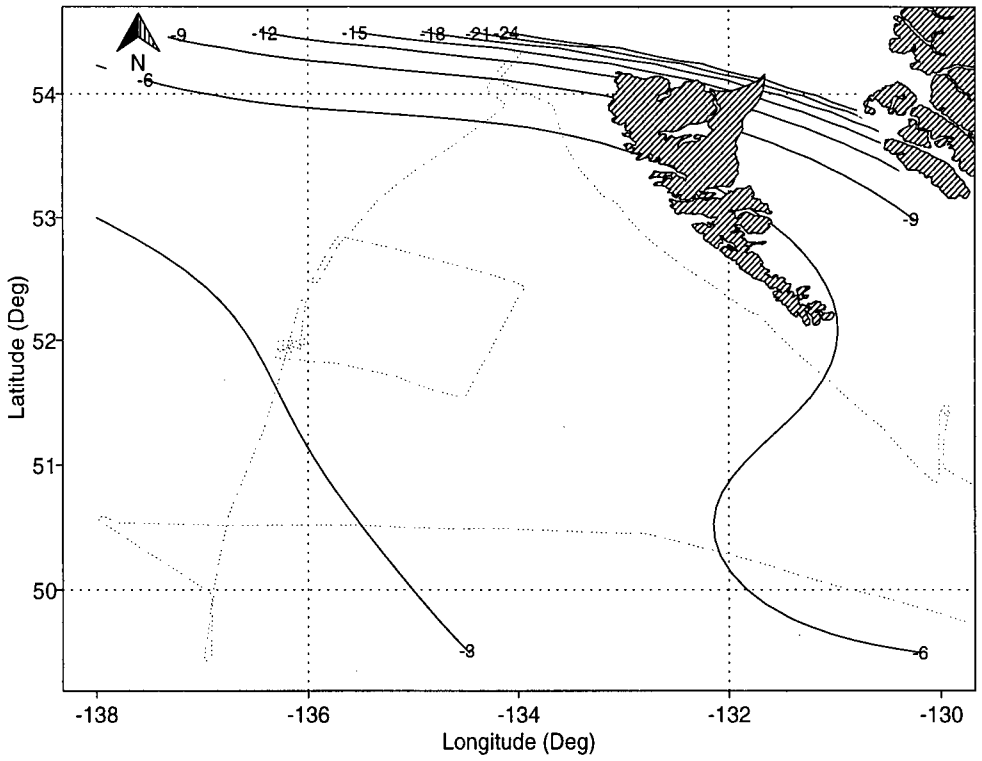

Figure 4.54: Interpolation estimates of ζ_i using eddy correlation L values. Contour interval is 3.

Chapter 5

Model Results

5.1 Introduction

This chapter complements the previous one with an analysis of model output calculated from observed fields. The first section details the model gridding process and clarifies the methods by which the input fields were determined. The next section presents model results. The second to last section describes conclusions drawn from a term analysis of the horizontal momentum equation used to obtain the analytic solution on which the model iterates. In the final section model inadequacies are discussed with reference to the output fields.

5.2 Model Grid

A 40×40 grid bounded by 138W and 130W longitude and 54.5N and 49.5N latitude was used. The N-S grid point spacing is therefore approximately half of the E-W grid point spacing. All input fields were obtained by interpolating observed values onto the model grid. Near surface air temperatures were obtained by adiabatically lowering observation level 2 (90 m) virtual air temperatures to 10 m and then interpolating the adjusted values onto the grid. Mean sea level pressures ($MSLP$) were reduced hydrostatically from 150 m (Level 3) to the surface and interpolated. SST was interpolated from radiometer derived estimates obtained on-board the P-3. Model input fields and parameters are summarized in further detail in Appendix B. Model results are presented in the next

section.

Gradients were calculated using centered fourth order differencing if the grid points were at a location greater than two points from the border and centered second order differencing at grid points located one point from the outer boundary. Gradients on the boundary were obtained by linearly interpolating from the nearest adjacent grid point.

5.3 Model Performance

Out of 1444 points (boundary excluded), at 9 points (0.6%) and 3 points (0.2%), inner and outer loop convergences respectively (see Section 2.5.3) were only 10%, at 4 points (0.3%) the horizontal temperature gradient was reduced to half of its original value and at 8 points (0.3%) the model was unable to converge to a solution. Model failure can be attributed to either domination of OLE by the thermal wind or to a failure of the molecular sub-layer parameterization of Liu *et al.* (1979).

5.4 Model Output

The model run incorporated thermal wind (baroclinicity), secondary flow (OLE) and stratification corrections. Surface air velocity ($\vec{U}$), sensible heat flux (Q_H), stability (z/L) and friction velocity (u_*) were analysed and then compared with observations made in section 4.3.2.

5.4.1 Winds

The top and bottom panels of Figure 5.2 depict modelled and observed level 2 (90 m) wind vectors respectively. Modelled air velocities are predominantly northeasterly in the far northern section of the domain and then turn sharply about a northwest-southeast oriented axis to become northerly over much of the southern half of the domain. A

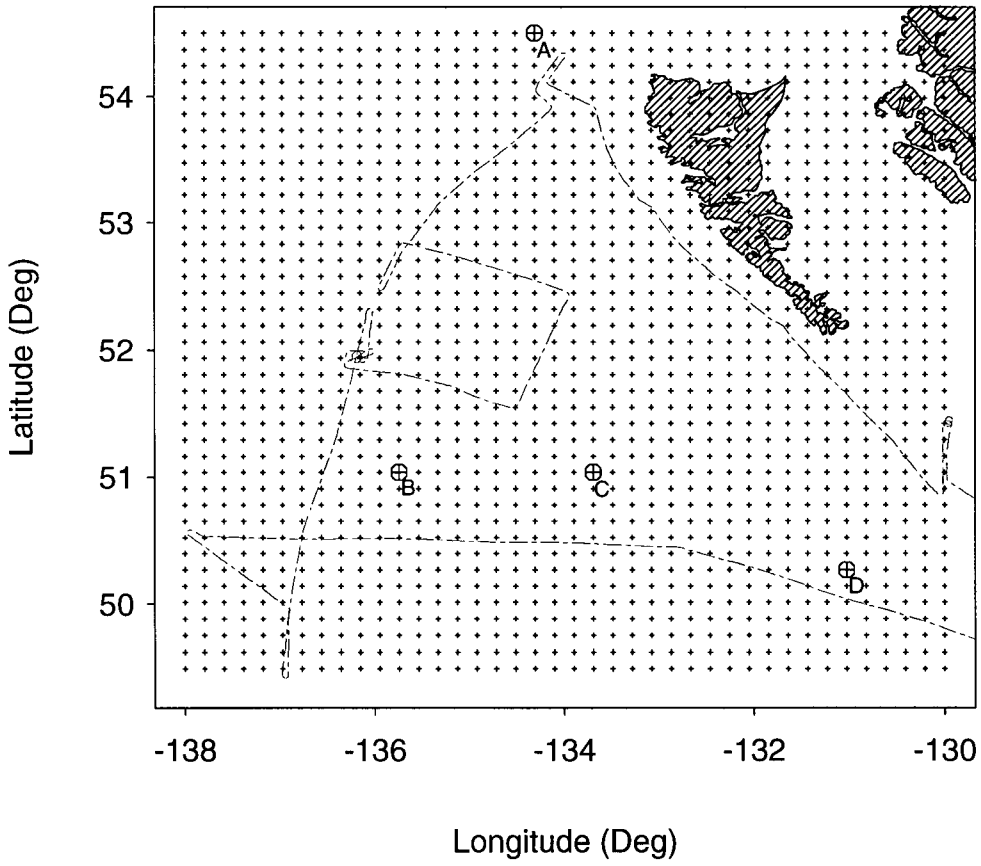

Figure 5.1: Schematic of 40×40 model grid. Grid points are indicated by a + and the 4 points at which term analysis was carried out are shown with a ⊕. Dashed line is aircraft flight track.

northeasterly component persists over most of the north-south extent of the eastern section of the domain. Strongest modelled wind speeds ($\approx$ 40 ms^{-1}) occur furthest north with the weakest values ($\approx$ 10 ms^{-1}) located near 52N 132W. Wind speeds decrease downwind along a corridor bounded by 134W and 137W but increase downwind between 132W and 134W. Speeds are considerably less in the 132W, 134W band than those in the 134W, 137W band. The mean modelled wind speed over the domain is $\approx$ 23 ms^{-1}.

Comparison of modelled air velocities with observed air velocities reveals a generally similar direction pattern. The largest differences exist in the northern middle section (between 132W and 136W) and in the southeast corner. In both regions modelled winds are veered (turned clockwise) with respect to observed winds. The large discrepancies can be attributed partially to the model initialization fields which are not well determined in those regions. Nonstationarity may also be affecting results in the southeast quadrant. Modelled and observed wind speeds compare best in the southwest quadrant which is also data rich (see Figure 3.2). Mean observed speeds are $\approx$ 16 ms^{-1}. The largest speed differences are in the same two regions noted for large direction differences. The differences are seen most easily by overlaying modelled winds with observed winds as shown in Figure 5.3. In the northern portion of the domain, modelled wind speeds exceed observed magnitudes by a factor of 2 in some instances. Modelled winds are also moderately higher than observed winds in the southeast corner. Higher model wind speeds would lead to higher model bulk heat flux values. That is the likely cause of large discrepancies between modelled and observed sensible heat fluxes in the northeast quadrant of Figure 5.4.

5.4.2 Sensible Heat Flux

Figure 5.4 shows contours of both modelled (top panel) and observed (bottom panel) bulk sensible heat flux (Q_H) estimated from values at 10 m. Modelled values are between 100

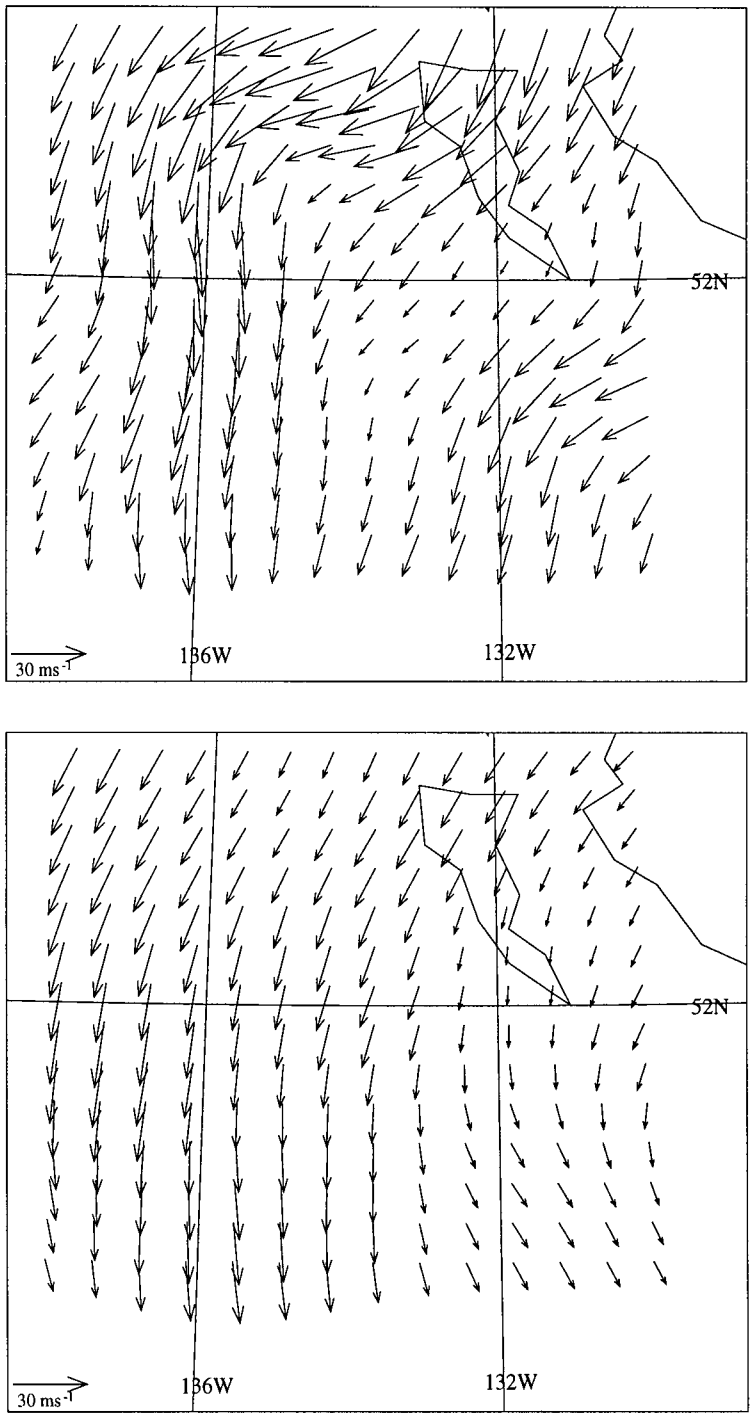

Figure 5.2: Modelled (top panel) and observed (bottom panel) estimates of horizontal near surface air velocities (90 m).

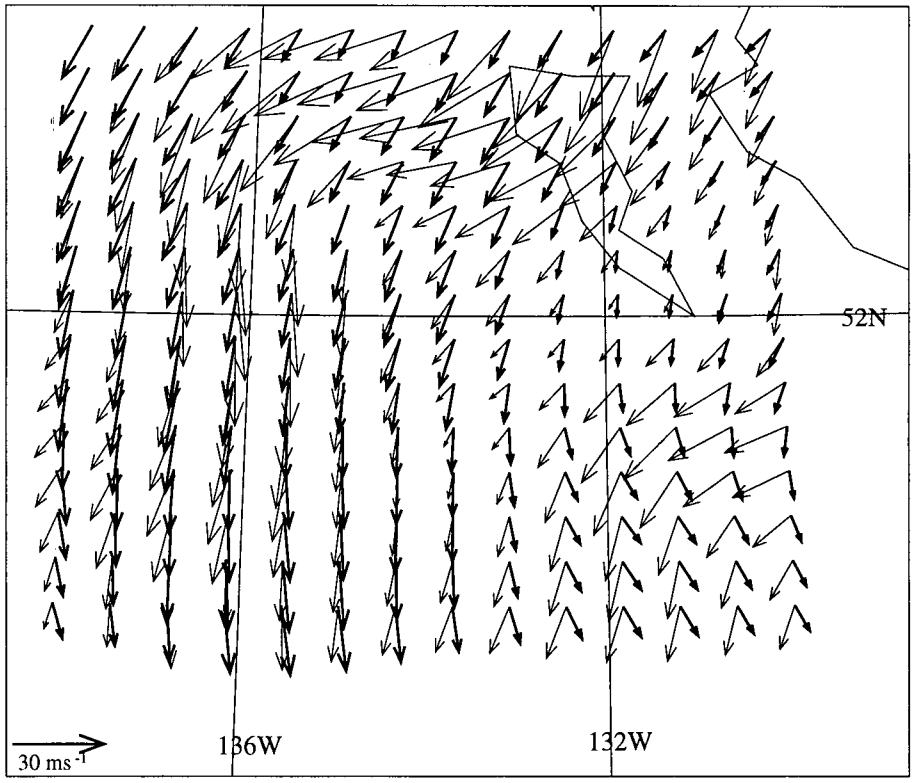

Figure 5.3: Modelled and observed estimates of near surface horizontal air velocities (90 m). Thick arrows depict observed velocities while thin arrows indicate modelled velocities.

and 500 Wm^{-2}. The mean gradient is oriented E-W with a number of extrema located in the centre. A high ($\approx$ 250 Wm^{-2}) lies just southeast of 52N 136W, and is accompanied by a low ($\approx$ 125 Wm^{-2}) to the east. Gradients become increasingly steeper to the north and east. A maximum Q_H of $\approx$ 500 Wm^{-2} occurs in the northeast corner of the domain which is also the location of the largest sea-air temperature differences ($\approx$ 13 K). South of the high are relatively smaller values which culminate in a low ($\approx$ 270 Wm^{-2}) in the southeast corner. A blank region appears in the model plot just southwest of the Queen Charlotte Ils. and corresponds to a cluster of 8 points where the model failed to converge to a solution. Model derived bulk estimates of Q_H are systematically larger than observed eddy correlation values by a factor of 2-3.

When compared with observed bulk estimates some similarities exist particularly in the western section of the study region. There, observed Q_H tends to match modelled Q_H as do respective gradients. An observed high ($\approx$ 180 Wm^{-2}) is situated just south of the $\approx$ 250 Wm^{-2} modelled high at 52N 136W. There is also correspondence between an observed low of $\approx$ 110 Wm^{-2} in the south (130W) and the modelled low of $\approx$ 125 Wm^{-2}. Another observed high ($\approx$ 215 Wm^{-2}) straddles both the shore and mainland of Graham Is. It is close to the modelled high appearing in the northeast corner (top panel of Figure 5.4) but is lower than the modelled high by more than a factor of 2. Overall, observed Q_H gradients are not as sharp as modelled gradients and modelled maximum Q_H is larger than observed maximum bulk Q_H by a factor of 2.

5.4.3 Stability

Figure 5.5 shows modelled (top panel) and observed (bottom panel) bulk estimates of the Monin Obukhov stability parameter (z/L). There are no predominant trends in the model field which is instead punctuated by a number of highs and lows. The blanked region southwest of the Queen Charlottes is evident as are two lows, one to

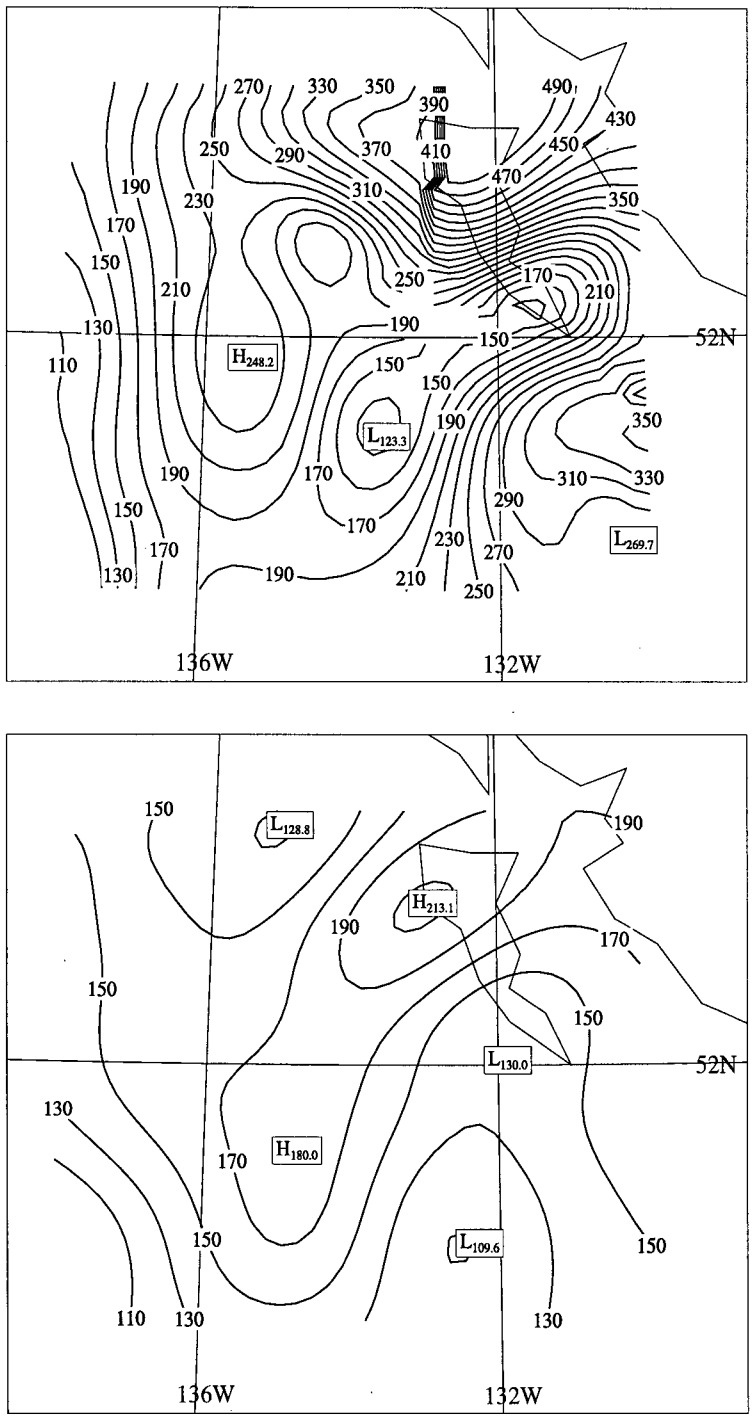

Figure 5.4: Modelled (top panel) and observed (bottom panel) horizontal distribution of surface sensible heat flux. Units are Wm^{-2} and contour interval is 20 Wm^{-2}.

the south and one to the east of the "failure" region. Modelled gradients are sharp near the "failure" region, while observed gradients are weaker. Over the entire domain modelled values lie within a -.01 to -2.5 range while observed values increase from -.42 to -.02 from the northeast to the southwest. Observed gradients are very sharp in the north and the southeast but they ease in the middle and southwest regions. Although modelled values exhibit a larger variation than do observed values, there is the suggestion in both fields of unstable stratification at low levels over the entire domain. Observed z/L values are more uniform than modelled values. Strong winds act to suppress z/L while low wind speeds tend to increase it. Modelled wind speeds are considerably larger than observed magnitudes in both the north and the southeast reaches of the domain and are likely moderating modelled z/L in those regions. Conversely, the region of relatively large z/L in the model field can be attributed to modelled wind speeds that are weaker than observed values. Further smoothing of the model field may result in more moderate gradients near the model "failure" region however it is unlikely that the two fields (observed and modelled) would be more comparable.

5.4.4 Surface Friction Velocity

Values of model derived and observed bulk u_* are shown in Figure 5.6. Overall, modelled quantities are higher than those observed. Modelled values range from 0.2 ms^{-1} to 1.5 ms^{-1} with an average value of 0.74 ms^{-1}. The range of observed values is 0.13 to 0.83 ms^{-1} with an average of 0.49 ms^{-1}. A high ($\approx$ 1.5 ms^{-1}) in the northern central portion of the model field lies near an observed high ($\approx$ 0.7 ms^{-1}) to the south although an unmarked modelled low corresponds more closely to the observed high. There is good correspondence between a modelled low and an observed low of approximately the same magnitude ($\approx$ 0.3 ms^{-1}) located just south of the "failure" region. Other extrema are two modelled highs of 1.1 ms^{-1} and 0.9 ms^{-1} located at 52N 136W and 51N 131W respectively.

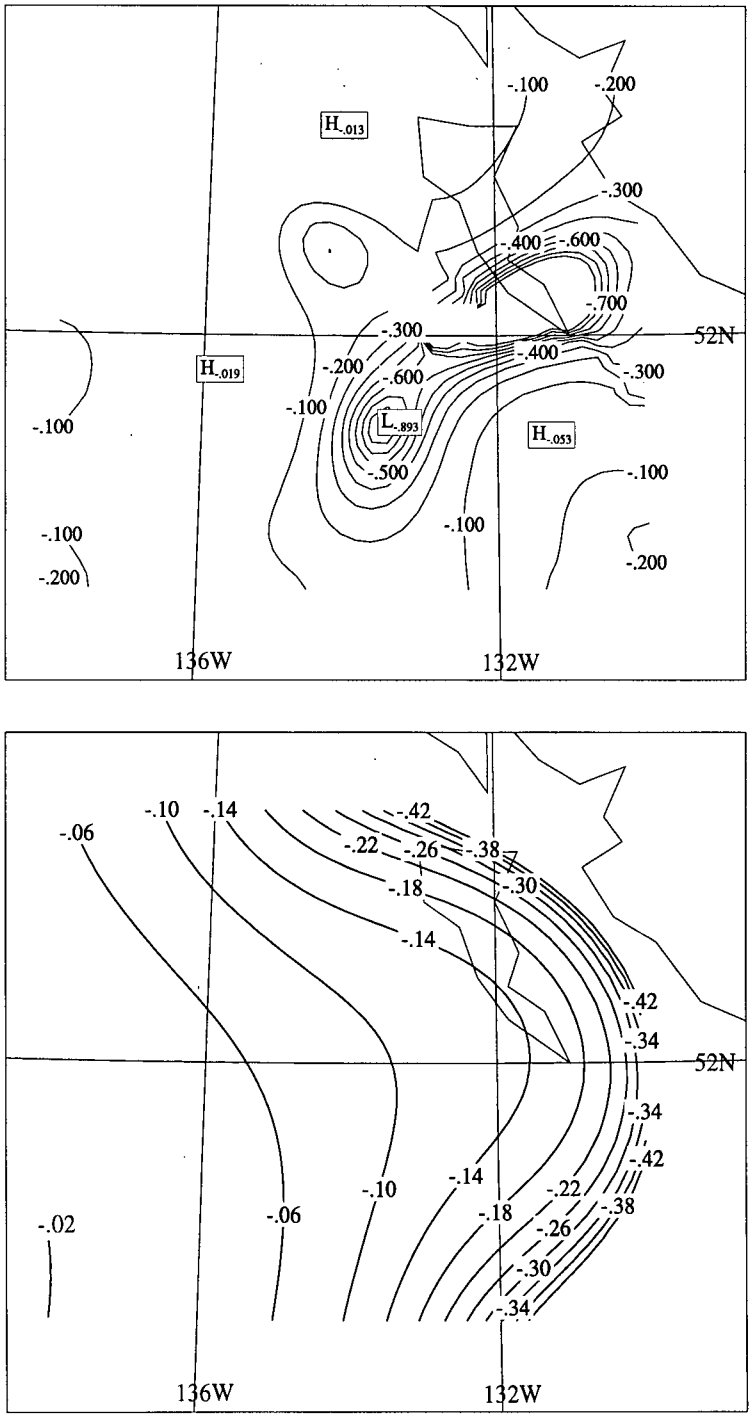

Figure 5.5: Modelled (top panel) and observed (bottom panel) bulk z/L (z=10 m). Contour interval is .1 in the top panel and .04 in the bottom panel.

In the observed field a high (0.8 ms^{-1}) at 51N 137W and a low (0.1 ms^{-1}) at 54N 136W can not be found in the modelled field. Gradients are sharper in the modelled field than in the observed field but there is no preferred gradient direction on a domain-size scale in the modelled field. Observed u_* values increase downwind on average. Overall, modelled and observed u_* fields are not identical but share some similarities.

5.5 Term Analysis

5.5.1 Introduction

By employing a term analysis of the momentum equation from which the analytic model solution was derived, one can quantify the dominant forces driving the model. The solution by Brown (1970) of an Ekman type regime in equilibrium with nonlinear forcing was for the equation,

$$\underbrace{f\mathbf{k}\times\mathbf{U}}_{1}-\underbrace{\partial^2 K_e\mathbf{U}/\partial z^2}_{2}+\underbrace{\nabla P/\rho}_{3}=\underbrace{(\mathbf{u}'_\mathbf{r}\cdot\nabla)\mathbf{u}'_\mathbf{r}}_{4} \tag{5.35}$$

where,

1 ≡ Coriolis acceleration due to use of a noninertial reference frame.

2 ≡ acceleration due to eddy viscosity.

3 ≡ acceleration due to pressure gradients.

4 ≡ acceleration due to organized large eddy perturbation (Reynold's stress divergence).

The velocity consists of three parts,

$$\mathbf{U}=\mathbf{U_m}+\mathbf{u}'_\mathbf{r}+\mathbf{u}''$$

Here, $\mathbf{U_m}$ is the mean velocity, $\mathbf{u}'_\mathbf{r}$ is that part of the turbulence which has been organized into OLE and $\mathbf{u}''$ is small-scale turbulence. It is thought that $\mathbf{u}'_\mathbf{r}$ contains

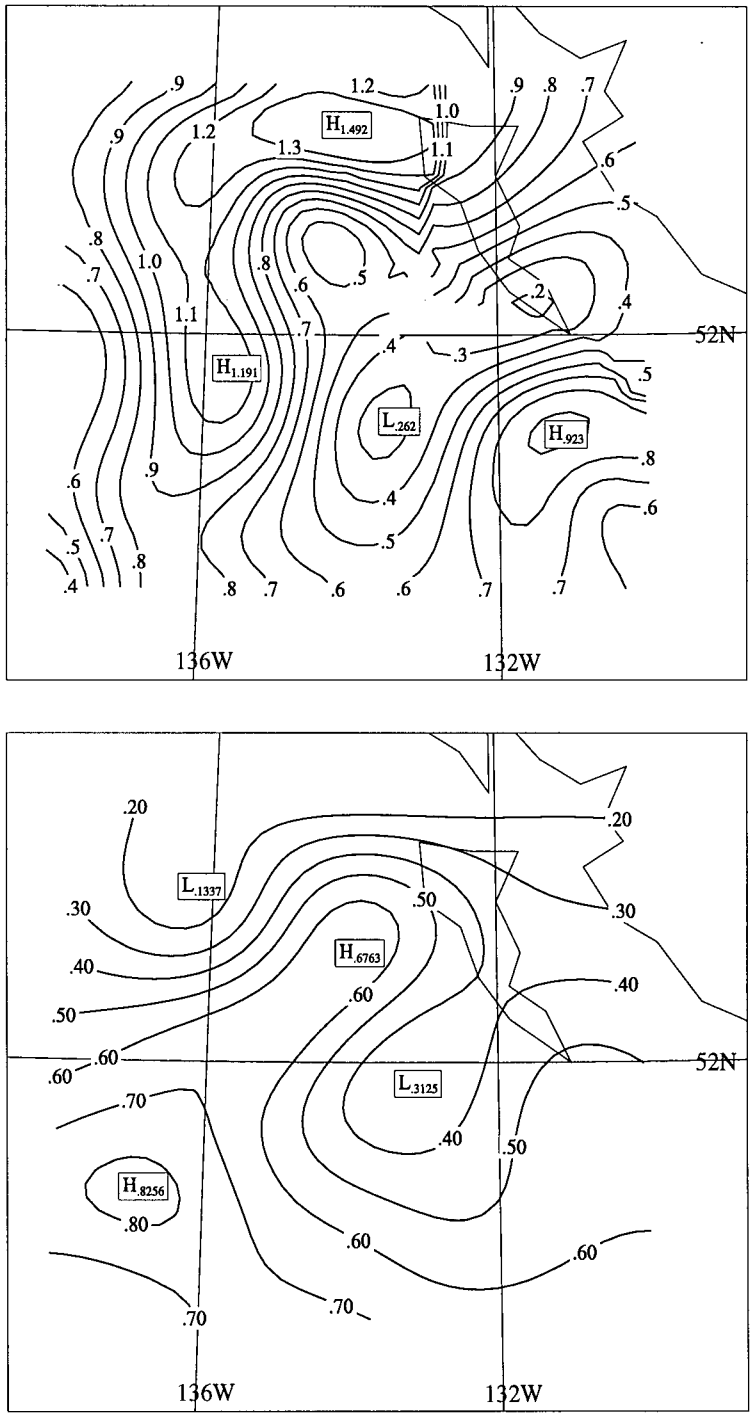

Figure 5.6: Modelled (top panel) and observed (bottom panel) bulk u_*. Units are ms^{-1} and contour interval is .1 ms^{-1}.

most of the turbulence energy. The mean flow $\mathbf{U_m}$ can be partitioned into two parts: $\mathbf{U_m} = \mathbf{U_E} + \mathbf{U_2}$ where $\mathbf{U_E}$ is the Ekman solution and $\mathbf{U_2}$, the secondary flow correction to $\mathbf{U_E}$. Presumably the eddy perturbation acts on the the lateral velocity component (v) only. A representative analysis of the x-momentum equation was done in each of the two model levels (Ekman and surface layers, 600 m and 10 m respectively) by choosing 4 points on the model grid. The points selected are shown in Figure 5.1 and their specific locations in both grid (i, j) and earth (lat, lon) coordinates are summarized in Table 5.3. It was desirable to choose locations that were either near observational data points (see Figure 5.1) (to minimize any error during the interpolation process) or in the vicinity of regions where modelled and observed air velocities were considerably different from one another. Points B and C were chosen to lie near observed data. Point A was chosen to lie on the domain boundary and in an area which also coincides with poorly correlated model wind velocity estimates. Point D was also located in a region where modelled and observed air velocities exhibited poor agreement with one another.

The coordinate system is defined with x and y in the along wind and cross wind directions (for the near surface wind) respectively. Appropriate coordinate rotations were performed on terms 1 and 3 of 5.35.

Point	(i,j)	(lat,lon)
A	(19,40)	(54.50,-134.31)
B	(12,13)	(51.04,-135.74)
C	(22,13)	(51.04,-133.69)
D	(35,7)	(50.27,-131.03)

Table 5.3: Table summarizing locations of points at which term analysis was carried out. Point name is given in the first column followed by grid and earth coordinates in columns 2 and 3 respectively. Grid origin (i=1, j=1) is located at the bottom left corner of grid (Figure 5.1).

Ekman Layer K_e was assumed to be both constant and unaffected by stratification. The value was calculated at the patching height, h_p, defined in section 2.5.3.

$$K_e = kh_p u_* \tag{5.36}$$

The shear gradient was derived as,

$$\frac{\partial^2 U}{\partial z^2} = \Lambda \cos(\gamma_e z + \pi/4) \tag{5.37}$$

where,

$$\Lambda = \sqrt{8}\gamma_e^2 G \exp(-\gamma_e z) \tag{5.38}$$

$$\gamma_e = [f/(2K_e)]^{1/2} \tag{5.39}$$

G in 5.38 is the geostrophic wind speed from the model. The analysis height was chosen to be 600 m which should be far enough above the surface layer to validate Ekman layer assumptions. Terms 1 and 3 were extracted directly from the model at the analysis height. Term 1 was obtained by combining the v wind component with the Coriolis parameter (f) while term 3 was calculated by multiplying the Coriolis parameter by the v geostrophic wind component. Term 4 was determined as a residual and should equal zero in the u component force balance. A characteristic boundary layer patching height (h_p) is 200 m and a characteristic K_e value is 40 $m^2 s^{-1}$.

Surface Layer In the surface layer term 3 can be estimated directly. The choice of coordinates requires that term 1 be zero and with the assumption of constant u_*^2, term 2 is also zero (independent of coordinates). In fact u_*^2 does decrease slowly with height and the balance of term 2 with term 3 allows estimation of the thickness of the constant stress layer.

5.5.2 Results

Table 5.4 summarizes term magnitudes at each of the 4 points and at both heights (10 m and 600 m) for the u wind component.

Point	Coriolis	Viscosity	Pres. Grad.	Residual
SURFACE LAYER (10 m)				
A	0	0	4.1	–
B	0	0	.01	–
C	0	0	.6	–
D	0	0	1.6	–
EKMAN LAYER (600 m)				
A	.9	.8	4.1	5.8
B	.7	.4	.01	1.11
C	.2	-.1	.6	.7
D	.4	-.03	1.6	1.97

Table 5.4: Summary of term magnitudes ($\times 10^{-3}$) at the 4 points chosen for term analysis. Units are ms^{-2}.

In the Ekman layer term 1 values range from .2 $\times 10^{-3}$ ms^{-2} at C to .9 $\times 10^{-3}$ ms^{-2} at A. Viscosity (term 2) ranges from .8$\times 10^{-3}$ to -.1$\times 10^{-3}$ ms^{-2}. One should recall that Ekman layer calculations were carried out with no stratification correction. The shear gradient (and hence term 2) becomes smaller with increasing stability; therefore term 2 values calculated here can be considered an upper bound to the values that would likely be found in the mission #6 MABL. Term 3 values do not change between the surface layer and Ekman layer (barotropic assumption). Due to the small variation among terms at any one location in the Ekman layer, terms 1 to 3 contribute non-trivially to term 4 which exhibits values between 1.1 $\times 10^{-3}$ and 5.8 $\times 10^{-3}$ ms^{-2}. The highest term 4 value is at A and the lowest value is at B. Term 4 values are generally of the same order of magnitude as terms 1 and 3, and these three terms dominate in the Ekman layer.

5.6 Discussion

To facilitate comparison of observed and modelled quantities a geographic coordinate system is now adopted. The x (u component) and y (v component) axis directions are defined by the North and East compass directions respectively.

Points A and D mark locations where modelled and observed wind velocities were markedly different while at B and C, modelled and observed velocities were more comparable. Table 5.5 summarizes observed and modelled wind magnitudes and the angle between the two at points A through D. At A, the modelled wind speed exceeds the observed speed by a factor of almost 2.5 (modelled $\approx$ 30.6 ms^{-1}, observed $\approx$ 11 ms^{-1}) and there is a 47° difference between wind directions. The largest direction mismatch (57°) is at D, but the largest magnitude difference is at A. The smallest wind direction difference (6°) is at B which also exhibits the closest wind speed agreement. Reasons for the discrepancies are discussed in the next section.

Point	$\|\vec{U}\|_{mod}$ (ms^{-1})	$\|\vec{U}\|_{obs}$ (ms^{-1})	Angle Diff. (°)
A	35.6	10.8	47
B	30.6	17.9	6
C	6.8	14.7	24
D	18.7	10.5	53

Table 5.5: Comparative summary of modelled and observed wind velocities at the 4 term analysis points. Fourth column shows the angle difference between observed and modelled wind velocities (OBS – MOD).

Observed and modelled wind velocities (Figure 5.2) differ most from one another in the north-central and southeast reaches of the domain. As mentioned previously the input $MSLP$ field (see Appendix B) may be a poor representation of the actual pressure field. To establish a qualitative relationship between the input pressure field and output 90 m

winds, both $\frac{\partial MSLP}{\partial x}$ and $\frac{\partial MSLP}{\partial y}$ were compared with corresponding modelled surface wind (90 m) components (u, v) at the four term analysis locations. Results are summarized in Table 5.6. At A, $\frac{\partial MSLP}{\partial y}$ is more than 15 times $\frac{\partial MSLP}{\partial x}$ and exceeds the value of any gradient at the other points. Similarly the velocity component (u) corresponding to $\frac{\partial MSLP}{\partial y}$ has the largest magnitude of any of the others including v. At B, $\frac{\partial MSLP}{\partial x}$ is considerably larger than $\frac{\partial MSLP}{\partial y}$ as is v in comparison to u. Point C exhibits the weakest gradients and concomitantly the lowest surface air speeds. Gradients at D are moderate as are respective wind speeds. In summary there is a strong relationship between modelled wind velocities and surface pressure gradients and modelled air velocities are highly sensitive to the shape of the input $MSLP$ field. Further investigation of the NMC analysis of $MSLP$ at 0z 3 Dec (Figure 4.4) reveals a sharp turning of pressure contours from a N-S to E-W orientation just north of the study area. Although the boundary layer model is executed on a grid point by grid point basis the pressure gradient is determined using adjacent grid points. Adjacent points will influence one another to an extent determined by the smoothing parameters used in the objective analysis (see Appendix A). The input $MSLP$ field does exhibit some turning, possibly too much. Ultimately, more regular and finer spatial resolution data sampling may serve to bring modelled and observed air velocities into closer agreement.

Point	$\partial MSLP/\partial x$ (Pa m^{-1})	v (ms^{-1})	$\partial MSLP/\partial y$ (Pa m^{-1})	u (ms^{-1})
A	3.9×10^{-4}	-9.4	60.0×10^{-4}	-34.3
B	-40.4×10^{-4}	-30.1	12.2×10^{-4}	-5.2
C	-7.4×10^{-4}	-6.1	4.6×10^{-4}	-3.0
D	-18.9×10^{-4}	-17.0	12.7×10^{-4}	-7.7

Table 5.6: Table showing pressure gradients and corresponding modelled 90 m wind components at the four term analysis locations.

There was moderate variation in the shape of pressure fields between levels 1 through 3. Level 3 was chosen because it most closely resembled NMC and AES analyses despite sparser data at that level than at level 2. Nevertheless the interpolation method was validated with a comparison of pressure fields obtained from various sources (see Section 3.4) and it is likely that other exacerbating factors contribute to discrepancies between model and observations.

The model predicts larger heat fluxes than observed eddy correlation fluxes because of its use of a bulk flux parameterization. However, model derived bulk estimates are reasonably consistent with observed bulk flux magnitudes in the region where the data are adequate.

Poor correspondence between modelled and observed air velocities in the vicinity of point D (Figure 5.1) can be attributed to two factors. The first is based on data paucity. Lack of SST data in the southeast region (Figure 3.2) of the model domain would contribute to errant stratification corrections there and could lead to poor determination of surface winds. A second factor is nonstationarity, the effects of which would be most noticeable in the southeast portion of the domain.

One known model inadequacy is the lack of a cloud parameterization. The MABL surface energy balance is dependent upon contributions from absorption, emission and reflection of radiation by clouds. By assuming the atmosphere is cloud free and that all longwave radiation is emitted to space, the surface energy balance would be in error should clouds exist. This factor would have been more influential in the Northern half of the mission #6 study domain than in the Southern half where cloud cover was less continuous (see Figure 4.53).

Chapter 6

Summary and Discussion

6.1 Summary

The mean vertical and surface layer horizontal structure of the marine atmospheric boundary layer (MABL) has been investigated during a cold air outbreak (CAO) over the northeast Pacific ocean in wintertime. Strong pressure gradients ($\approx 55 \times 10^{-3}$ hPa km^{-1}) across interior British Columbia facilitated strong outflow of frigid air (850 hPa average temperature of -10 °C) over a relatively warm ocean surface. Profile data were collected by radiosondes and dropsondes released during mission #6 of the Storm Transfer and Response Experiment (STREX). Irregularly distributed data collected principally by a NOAA P-3 aircraft were interpolated onto a regular 40×40 horizontal grid using the objective analysis scheme of LeTraon (1990) and Davis (1985).

Profiles of potential temperature indicated a downwind increase in upper boundary layer stability while in the surface layer, the boundary layer was consistently unstable over the entire domain. Humidity profiles exhibited a gradual humidity decrease with height and increasing moisture downwind. A downwind upper layer stability increase contradicts other literature but may be a result of diurnal cycle influence and a negative downwind trend in cloud cover.

An investigation of horizontal distributions of air and sea temperatures, humidity, surface fluxes, wind speed and stability revealed significant variations of some quantities and moderately strong air-sea interaction. Surface layer potential air temperatures

(θ_v) at the 3 analysis heights (50 m, 90 m, 150 m above sea level) exhibited downwind increases corresponding to an average gradient of $\approx$0.9°/100 km. Specific humidity (q) was observed to increase downwind from 1.4 $g\,kg^{-1}$ (-134W 54N) to 2.8 $g\,kg^{-1}$ (-136W 49N). At all levels, q values showed greater variability to the south than to the north. At levels 2 and 3 distinctive maxima and minima were attributed to Mesoscale Cellular Convection (MCC) or anomalies produced by the objective analysis, the latter being the most probable. Surface layer vertical q gradients were minimal which suggests well mixed conditions. SST increased from northwest to southeast with an average gradient of $\approx$ 0.5°/100 km. Because the SST gradient was orientated obliquely to the mean wind (and air temperature gradient) the strength of sensible heat transfer at the sea surface was likely not at it's theoretical maximum.

Heat fluxes were calculated using eddy correlation statistics obtained by a P-3 aircraft. Maximum observed surface total heat flux (Q_T) was 365 Wm^{-2} ($Q_E \approx 270$ Wm^{-2}, $Q_H \approx 95$ Wm^{-2}) based on eddy covariance statistics. Latent heat flux plots exhibited a weak downwind increase while sensible heat flux decreased downwind. Large sea-air temperature differences dominated a downwind air velocity increase and corresponded to the strongest sensible heat fluxes. Estimates of boundary layer height based on inversion base height (z_i) indicated that contours aligned themselves closer to SST contours than to air temperature contours. Perhaps variable cloud distribution is one of a number of processes contributing to a non-perpendicular orientation of the height gradient to the wind or the objective interpolation is inadequately assessing the distribution. X-Y vector plots of horizontal winds suggest backing winds as one moves downwind. Average wind speeds increased through each of the 3 levels from $\approx$ 15 ms^{-1} (50 m) to $\approx$ 20 ms^{-1} (150 m). Level 2 (90 m) winds increased downwind which would act to increase energy transport at the surface and encourage stronger vertical and horizontal transport of quantities throughout the boundary layer. Further evidence of increased energy transport downwind

was found in plots of Reynolds Stress (τ) and u_*. Largest u_* values (0.8 ms^{-1}) were found in the southernmost portion of the domain. Surface layer stability characteristics were investigated as well. A plot of the Monin-Obukhov stability parameter (z/L) implies a northeast to southwest increase in lower boundary layer stability. Eddy correlation estimates are smaller than bulk estimates by a factor of 2 over most of the domain. The downwind increase is not expected as increased downwind modification of the surface layer should promote increased convection.

A comparison of eddy correlation and bulk determined heat fluxes revealed significant differences between the two parameterizations. Bulk estimates of Q_H were larger than eddy correlation estimates by as much as a factor of 10 but in most cases they were larger by a factor of 3-4. Bulk estimates of Q_E were also larger than eddy correlation estimates by a factor of 3-4. Conversely, bulk estimates of surface Reynolds Stress were consistently lower than eddy correlation estimates by a factor of 2. Instrument contamination may have affected calculations of eddy correlation statistics but are unlikely to be large enough to incur a factor of 2-3 difference from bulk estimates. It remains unclear what is causing the large discrepancies. The error associated with SST measurements is large. It is possible that a systematic error of +2-3 degrees was present in the measurements. A positive error would result in artificially high bulk estimates of both latent and sensible heat fluxes.

Turbulence kinetic energy (TKE) was also explored to elucidate correlations between TKE and surface energy exchange. It was found that TKE increased in the downwind direction and that surface layer turbulence was more isotropic than has been observed under neutral conditions by others. Moreover, wind variances were observed to be more sensitive to atmospheric stability than results by others suggest.

A spectral analysis suggests the presence of roll circulations in u, v and q at scales of $\approx$ 15 and 25 km and an increasing roll aspect ratio downstream. Evidence was not

conclusive but it is speculated that rolls are produced by a combination of inflection point and convective instabilities.

To facilitate further interpretation, a simple one dimensional (z) analytic two-layer similarity model was employed, incorporating the effects of organized large eddy (OLE) circulations, baroclinicity and stratification. Model derived wind speeds, surface fluxes and stability were compared with observed fields with reasonable results.

Modelled wind fields were comparable to observed fields in well determined regions particularly in the southwest portion of the domain. Modelled near surface (90 m) wind speeds were ≈ 23 ms^{-1} on average while observed wind speeds at the same height exhibited an average value of ≈ 16 ms^{-1}. A better comparison would result from partitioning the domain into well determined regions and poorly determined regions and then comparing calculated averages of modelled and observed wind speeds in each area separately. If the two regions of anomolously high model wind speeds (points A and D in Figure 5.1) were eliminated from the average, the modelled value would be lower. Model estimates of friction velocity (u_*) were comparable to observed (bulk) estimates with an average value of 0.65 ms^{-1}. Modelled bulk estimates of Q_H were comparable to observed bulk estimates in the southwestern portion of the domain. Modelled Q_H values were considerably larger in the northeast corner, due to unreasonably large wind speed estimates there. The northeast and southeast portions of the domain were data limited. Modelled bulk stability (z/L) estimates were numerically similar to observed bulk estimates however the model failed to reproduce the observed spatial stability distribution.

6.2 Future Research

This study was carried out in an effort to better determine the relevant physical processes working vertically and horizontally in the near surface layer of the MABL under the

influence of a CAO and to relate them to the dynamical character of the MABL as a whole.

The most glaring inadequacy encountered during this study was the irregular data sampling scheme. The P-3 flight pattern was such that a large section in the middle of the study domain was not sampled. This lack of data has significant implications for the interpretation of results, particularly horizontal distributions. A spatially more regular sampling path would facilitate increased confidence in interpretations. Investigation of high frequency MABL features were hindered significantly by poor data resolution. A maximum resolvable wavelength of 4 km is insufficient for completely determining flow structure at frequencies where important air-sea exchanges may occur via finite eddy interactions.

When aircraft are used for boundary layer sampling, flight stacks (a sequence of flight legs run along the same line and at various heights above sea level) are an excellent means for determining mechanisms responsible for convective or dynamic instabilities. They allow for a better description of the vertically varying quantities which are necessary for a complete three dimensional characterization of the boundary layer. The mission #6 P-3 flight did not include any stack runs. Future studies should incorporate this technique into their boundary layer sampling strategies.

There is still poor understanding of the processes occurring within a CAO MABL in the region of transition between rolls and mesoscale cellular convection (MCC). Given the ubiquity of OLE and MCC in the atmosphere, subsequent MABL studies should consider inclusion of this region in their sampling scenarios.

Another poorly quantified phenomenon is the contribution of OLE to the horizontal and vertical transport of heat and mass within the MABL. This study suggests that the importance of OLE circulations are not trivial and that inclusion of their effects in boundary layer parameterizations for use in general circulation models (GCMs) is worth

consideration. Better parameterizations of air-sea exchange processes still need to be developed so that the *ad hoc* flux drift corrections currently being employed in large scale climate model integrations are not necessary.

Bibliography

Agee, E. and Dowell, K. (1974). Observational studies of mesoscale cellular convection. *J. Appl. Met.*, **13**, 46–53.

Agee, E., Chen, T., and Dowell, K. (1973). A review of mesoscale cellular convection. *Bull. Amer. Meteor. Soc.*, **54**, 1004–1012.

Arya, S. (1988). *Introduction to Micrometeorology*, volume 42. Academic Press, International Geophysics Series. 307 pp.

Arya, S. and Wyngaard, J. (1975). Effect of baroclinicity on wind profiles and the geostrophic drag law for the convective planetary boundary layer. *J. Atmos. Sci.*, **32**, 767–778.

Asai, T. (1970). Three-dimensional features of thermal convection in a plane couette flow. *J. Meteor. Soc. Japan*, **48**, 18–29.

Asai, T. and Nakasuji, I. (1973). The stability of the Ekman boundary flow with thermally unstable stratification. *J. Meteor. Soc. Japan*, **51**, 29–42.

Atlas, D., Walter, B., Chou, S., and Sheu, P. (1986). The structure of the unstable marine boundary layer viewed by lidar and aircraft observations. *J. Atmos. Sci.*, **43**, 1301–1318.

Bane, J. J. and Osgood, K. (1989). Wintertime air-sea interaction processes across the Gulf Stream. *J. Geophys. Res.*, **94**, 10,755–10,772.

Benard, H. (1901). Les tourbillons cellulairs dans une nappe liquide transportant de la chaleur par convection en regime permanent. *Ann. Chim. Phys.*, **23**, 62–144.

Boussinesq, J. (1877). Essai sur la thëorie des eaux courants. *Mem. Pres. Div. Savants Acad. Sci. Paris*, **23**(1), 1–680.

Boussinesq, J. (1903). Theorie analytique de la chaleur. Gauthier-Villars, Paris.

Brown, R. (1970). A secondary flow model for the planetary boundary layer. *J. Atmos. Sci.*, **29**, 850–859.

Brown, R. (1972). On the inflection point instability of a stratified Ekman boundary layer. *J. Atmos. Sci.*, **29**, 850–859.

Brown, R. (1974a). *Analytic Methods in Planetary Boundary Layer Modelling.* J. Wiley and Sons, New York. 148 pp.

Brown, R. (1974b). Matching classical boundary layer solutions: Toward a geostrophic drag coefficient relation. *Bound.-Layer Meteor.*, **7**, 489–500.

Brown, R. (1978). Similarity parameters from first order closure and data. *Bound.-Layer Meteor.*, **14**, 381–396.

Brown, R. (1980). Longitudinal instabilities and secondary flows in the planetary boundary layer: A review. *Rev. Geophys. Space Phys.*, **18**(3), 683–697.

Brown, R. (1981a). Modelling the geostrophic drag coefficient for AIDJEX. *J. Geophys. Res.*, **86**(C3), 1989–1994.

Brown, R. (1981b). On the use of exchange coefficients in modelling turbulent flow. *Bound.-Layer Meteor.*, **20**, 111–116.

Brown, R. (1982). On two-layer models and the similarity functions for the PBL. *Bound.-Layer Meteor.*, **24**, 451–463.

Brown, R. (1991). *Fluid Mechanics of the Atmosphere.* Academic Press. 486 pp.

Brown, R. and Foster, R. (1991). Comparison of a 1-D analytic PBL model with secondary flow and a second-order closure model using GCM data. In *Proceedings AGU Fall Meeting*, volume EOS 72.

Brown, R. and Foster, R. (1994). On PBL models for general circulation models. *Global Atmos. Ocean Sys.*, **2**, 163–183.

Brown, R. and Levy, G. (1986). Ocean surface pressure fields from satellite sensed winds. *Mon. Wea. Rev.*, **114**, 2197–2206.

Brown, R. and Liu, W. (1982). An operational large scale marine PBL model. *J. Appl. Met.*, **21**(3), 261–269.

Brown, R. and Zeng, L. (1994). Using ERS-1 scatterometer data to determine midlatitude storm low pressures. *J. Appl. Met.*, **33**(9), 1088–1095.

Brümmer, B. (1985). Structure, dynamics and energetics of boundary layer rolls from KONTUR aircraft observations. *Beitr. Phys. Atmos.*, **58**(2), 237–254.

Brümmer, B. (1989). Arktis 1988 – field phase report. *Hamburger Geophys. Einzel.*, **B6**.

Brümmer, B., Rump, B., and Kruspe, G. (1992). A cold air outbreak near Spitsbergen in springtime. *Bound.-Layer Meteor.*, **62**, 13–46.

Buckingham, S. (1914). On physically similar systems: Illustrations of the use of dimensional analysis. *Phys. Rev.*, **4**, 345.

Budyko, M. (1963). Atlas of heat balance of the earth's surface. USSR Glavnaia Geofizicheskaia Observatoriia, Moscow.

Budyko, M. (1978). The heat balance of the earth. In J. Gribbin, editor, *Climatic Change*, pages 85–113. Cambridge University Press.

Bunker, A. (1976). Computations of surface energy flux and annual air-sea cycles of the north Atlantic Ocean. *Mon. Wea. Rev.*, **104**, 1122–1139.

Bunker, A. and Worthington, L. (1976). Energy exchange charts of the north Atlantic Ocean. *Bull. Amer. Meteor. Soc.*, **57**, 450–467.

Burt, W. and Agee, E. (1977). Buoy and satellite observations of mesoscale cellular convection during AMTEX 75. *Bound.-Layer Meteor.*, **12**, 3–24.

Businger, J., Wyngaard, J., Izumi, T., and Bradley, E. (1971). Flux profile relationships in the atmospheric surface layer. *J. Atmos. Sci.*, **28**, 181–189.

Cess (1990). intercomparison and interpretation of climate feedback processes in 19 atmospheric general circulation models. *J. Geophys. Res.*, **25**, 16601–16615.

Chlond, A. (1992). Three-dimensional simulation of cloud street development during a cold air outbreak. *Bound.-Layer Meteor.*, **58**, 161–200.

Chou, S. (1993). A comparison of airborne eddy correlation and bulk aerodynamic methods for ocean-air turbulent fluxes during cold-air outbreaks. *Bound.-Layer Meteor.*, **64**, 75–100.

Chou, S. and Atlas, D. (1982). Satellite estimates of ocean-air heat fluxes during cold air outbreaks. *Mon. Wea. Rev.*, **110**, 1434–1450.

Chou, S. and Ferguson, M. (1991). Heat fluxes and roll circulations over the western Gulf Stream during an intense cold-air outbreak. *Bound.-Layer Meteor.*, **55**, 255–282.

Chou, S., Atlas, D., and Yeh, E. (1986). Turbulence in a convective marine atmospheric boundary layer. *J. Atmos. Sci.*, **43**(6), 547–564.

Chrobok, G., Raasch, S., and Etling, D. (1992). A comparison of local and non-local closure methods for the case of a cold air outbreak. *Bound.-Layer Meteor.*, **58**, 69–90.

Coleman, G., Ferzinger, J., and Spalart, P. (1990). A numerical study of the turbulent Ekman layer. *J. Fluid Mech.*, **213**, 313–348.

Cubasch, U. (1989). *Aspects of Coupling Atmosphere and Ocean Models*, pages 39–60. Meteorologisches Institut, Universität Hamburg.

Davis, R. (1985). Objective mapping by least squares fitting. *J. Geophys. Res.*, **90**(C3), 4773–4777.

Deardorff, J. (1972). Numerical investigation of neutral and unstable planetary boundary layers. *J. Atmos. Sci.*, **29**, 91–115.

Dirks, R., Küttner, J., and Moore, J. (1988). Genesis of atlantic lows experiment (GALE): An overview. *Bull. Amer. Meteor. Soc.*, **69**, 148–160.

Driedonks, A. (1982). Models and observations of the growth of the atmospheric boundary layer. *Bound.-Layer Meteor.*, **23**, 283–306.

Ekman, V. (1905). On the influence of the earth's rotation on ocean currents. *Arkiv. Matem. Astr. Fysik.*, **2**(11).

Etling, D. (1971). The stability of an Ekman boundary flow as influenced by thermal stratification. *Beitr. Phys. Atmos.*, **44**, 168–186.

Etling, D. and Brown, R. (1993). Roll vortices in the planetary boundary layer: A review. *Bound.-Layer Meteor.*, **65**, 215–248.

Etling, D. and Wipperman, F. (1975). On the instability of a planetary boundary lyer with Rossby number similarity. *Bound.-Layer Meteor.*, **9**, 341–360.

Faller, A. and Kaylor, R. (1966). A numerical study of the laminar ekman layer. *J. Atmos. Sci.*, **23**, 466–480.

Fleagle, R. and Nuss, W. (1985). The distribution of surface fluxes and boundary layer divergence in midlatitude ocean storms. *J. Atmos. Sci.*, **42**(8), 784–799.

Fleagle, R., Miyake, M., Garrett, J., and McBean, G. (1982). Storm transfer and response experiment. *Bull. Amer. Meteor. Soc.*, **63**(1), 6–14.

Foster, R. and Brown, R. (1991). An investigation into the importance of stratification, thermal wind, non-stationarity and rolls in PBL parameterizations. In *Proceedings AGU Fall Meeting*, volume EOS 72.

Foster, R. and Brown, R. (1994a). On large-scale PBL modelling: surface layer models. *Global Atmos. Ocean Sys.*, **2**, 185–198.

Foster, R. and Brown, R. (1994b). On large-scale PBL modelling: surface wind and latent heat flux comparisons. *Global Atmos. Ocean Sys.*, **2**, 199–219.

Friehe, C. and Schmitt, K. (1976). Parameterization of air-sea interface fluxes of sensible heat and moisture by bulk aerodynamic formulas. *J. Phys. Oceanogr.*, **6**, 801–809.

Frisch, A., Miller, L., and Strauch, R. (1974). Three-dimensional air motion measured in snow. *Geoph. Res. Letters*, **1**, 86–89.

Garratt, J. (1994). *The Atmospheric Boundary Layer.* Cambridge Atmospheric and Space Science. Cambridge University Press. 316 pp.

Greenhut, G. (1981). Analysis of aircraft measurements of momentum flux in the sub-cloud layer over the tropical atlantic ocean during GATE. *Bound.-Layer Meteor.*, **20**, 75–100.

Greenhut, G. and Gilmer, R. (1985). Calibration and accuracy of the NOAA/ERL gust probe system and intercomparisons with other systems. Technical Report ESG-22, NOAA. 30 pp.

Grossman, R. (1982). An analysis ov vertical velocity spectra obtained in the BOMEX fair-weather, trade-wind boundary layer. *Bound.-Layer Meteor.*, **23**, 323–357.

Grossman, R. and Betts, A. (1990). Air-sea interaction during an extreme cold air outbreak from the eastern coast of the United States. *Mon. Wea. Rev.*, **118**, 324–342.

Hasse, L. (1990). Oceanic micrometeorological field experiments: An historical perspective. *Bound.-Layer Meteor.*, **50**, 139–146.

Hein, P. and Brown, R. (1988). Observations of longitudinal roll vortices during arctic cold air outbreaks over open water. *Bound.-Layer Meteor.*, **45**, 177–199.

Hoeber, H. (1982). KONTUR field phase report. *Hamburger Geophys. Einzel.*, **B6**.

Holton, J. (1979). *An Introduction to Dynamic Meteorology*, volume 48. Academic Press, International Geophysics Series, 2nd edition.

Jackson, P. (1993). *Gap Winds in a Fjord: Howe Sound, British Columbia.* Ph.D. thesis, University of British Columbia, Vancouver B.C.

Kellner, G., Wamser, C., and Brown, R. (1992). An observation of the planetary boundary layer in the marginal ice zone. *J. Geophys. Res.*, **92**(C7), 6955–6965.

Kelly, R. (1977). The onset and development of rayleigh-benard convection in shear flows: A review. In D. Spalding, editor, *Physiochemical Hydrodynamics*, volume 1, pages 65–79. Advance Publications.

Kelly, R. (1984). Horizontal roll and boundary-layer interrelationships observed over Lake Michigan. *J. Atmos. Sci.*, **41**, 1816–1826.

Kiehl, J. (1992). *Atmospheric Circulation Models.* Climate System Modelling. Cambridge University Press.

Krishna, K. (1981). A two-layer first-order closure model for the study of the baroclinic atmospheric boundary layer. *J. Atmos. Sci.*, **38**(7), 1401–1417.

Krueger, A. and Fritz, S. (1961). Cellular cloud patterns revealed by tiros 1. *Tellus*, **13**, 1–7.

Küttner, J. (1959). The band structure of the atmosphere. *Tellus*, **11**(3), 267–294.

Küttner, J. (1971). Cloud bands in the earth's atmosphere: Observations and theory. *Tellus*, **23**, 404–425.

Large, W. and Pond, S. (1982). Sensible and latent heat measurements over the ocean. *J. Phys. Oceanogr.*, **12**, 464–482.

LeMone, M. (1973). The structure and dynamics of horizontal roll vortices in the planetery boundary layer. *J. Atmos. Sci.*, **30**, 1077–1091.

LeMone, M. (1976). Modulation of turbulence energy by longitudinal rolls in an unstable boundary layer. *J. Atmos. Sci.*, **33**, 1308–1320.

LeMone, M. and Pennell, W. (1976). The relationship of trade wind cumulus distribution to subcloud layer fluxes and structure. *Mon. Wea. Rev.*, **101**, 524–539.

Lenschow, D. (1972). The air mass transformation experiment (AMTEX). *Bull. Amer. Meteor. Soc.*, **53**, 353–357.

Lenschow, D. and Agee, E. (1974). The air mass transformation experiment (AMTEX). *Bull. Amer. Meteor. Soc.*, **55**, 1228–1235.

Lenschow, D. and Agee, E. (1976). Preliminary results from the air mass transformation experiment (AMTEX). *Bull. Amer. Meteor. Soc.*, **57**(11), 1346–1355.

LeTraon, P. (1990). A method for optimal analysis of fields with spatially variable mean. *J. Geophys. Res.*, **95**(C8), 13,543–13,547.

Levy, G. and Brown, R. (1991). Southern hemisphere synoptic weather from a satellite scatterometer. *Mon. Wea. Rev.*, **119**, 2803–2811.

Lilly, D. (1966). On the instability of Ekman boundary flow. *J. Atmos. Sci.*, **23**, 481–494.

Liu, W., Katsaros, K., and Businger, J. (1979). Bulk parameterization of air-sea exchanges of heat and water vapor including the molecular constraints at the interface. *J. Atmos. Sci.*, **36**, 1722–1734.

Martin, T. and Bakan, S. (1991). Airplane investigation of a case of convective cloud bands over the north sea. *Bound.-Layer Meteor.*, **50**, 359–380.

Mason, P. (1983). On the influence of variation in monin-obhukov length on horzontal roll vortices in an inversion-capped planetary boundary layer. *Bound.-Layer Meteor.*, **27**, 43–68.

Mason, P. (1985). A numerical study of cloud streets in the planetary boundary layer. *Bound.-Layer Meteor.*, **32**, 281–304.

Mason, P. and Sykes, R. (1982). A two-dimensional numerical study of horizontal roll vortices in the neutral atmospheric boundary layer. *Q. J. R. Meteorol. Soc.*, **108**, 801–823.

Mason, P. and Thomson, D. (1987). Large-eddy simulations of the neutral-static-stability planetary boundary layer. *Q. J. R. Meteorol. Soc.*, **113**, 413–443.

Merceret, F. (1983). A study of NOAA-P3 terminal navigation errors based on navigator's logbooks. Tech. Memo OAO 2, NOAA, Miami, FL. 63 pp.

Miura, Y. (1986). Aspect ratios of longitudinal rolls and convection cells observed during cold air outbreaks. *J. Atmos. Sci.*, **43**(1), 26–39.

Miyake, M. and Recker (1980). *STREX Field Phase Report.* STREX Data Center.

Moeng, C.-H. (1984). A large-eddy simulation model for the study of planetary boundary layer turbulence. *J. Atmos. Sci.*, **41**, 2052–2062.

Monin, A. and Obukhov, A. (1954). Basic laws of turbulent scaling in the atmosphere near the ground. *Tr. Akad. Nauk.*, **24**(151), 1963–1987.

Overland, J. and Wilson, J. (1984). Mesoscale variability in marine winds at mid-latitude. *J. Geophys. Res.*, **89**(C6), 10,599–10,614.

Palmen, E. and Newton, C. (1969). *Atmospheric Circulations Systems: Their Structure and Physical Interpretation.* Academic Press. 603 pp.

Panin, G. (1990). Some experimental results from studies of air-sea interactions. *Bound.-Layer Meteor.*, **50**, 147–152.

Panofsky, H., Tennekes, H., Lenschow, D., and Wyngaard, J. (1977). The characteristics of turbulent velocity components in the surface layer under convective conditions. *Bound.-Layer Meteor.*, **11**, 355–361.

Paulson, C. (1970). The mathcmatical representation of wind speed and temperature profiles in the unstable atmospheric surface layer. *J. Appl. Met.*, **9**, 857–861.

Pennell, W. and LeMone, M. (1974). An experimental study of turbulence structure in the fair-weather trade wind boundary layer. *J. Atmos. Sci.*, **31**, 1308–1323.

Plank, V. (1965). The cumulus and meteorological events of the Florida peninsula during a particular summertime period. Technical report, Air Force Cambridge Research Lab, Bedford, MA.

Prandtl, L. (1904). Flow near a boundary.

Prandtl, L. (1925). Über die ausgebildste turbulence. *ZAMM*, **5**(136). and Proc. Inst. Congress Appl. Mech., Zurich, 1926.

Randall, D., Presley, E., and Bush, G. (1992). Intercomparison and interpretation of surface energy fluxes in atmospheric general circulation models. *J. Geophys. Res.*, **97**(D4), 3711–3734.

Reinking, R. (1980). Vertical eddy motion and energy transfer at very low altitudes over the tropical Atlantic ocean. *Deep Sea Res. (Suppl.)*, **26**, 23–49.

Riehl, H. (1979). *Climate and Weather in the Tropics.* Academic Press. 611 pp.

Rossby, C. and Montgomery, R. (1935). The layer of frictional influence in wind and ocean currents. *Papers Phys. Oceanog. and Met.*, **3**(3), 101 pp.

Rothermal, J. and Agee, E. (1980). Aircraft investigation of mesoscale cellular convection during AMTEX 75. *J. Atmos. Sci.*, **37**, 1027–1040.

Schmidt, H. and Schumann, U. (1989). Coherent structure of the convective boundary layer derived from large-eddy simulations. *J. Fluid Mech.*, **200**, 511–562.

SethuRaman, S., Riordan, A., Holt, T., Stunder, M., and Hinman, J. (1986). Observations of the marine boundary layer thermal structure over the Gulf Stream during a cold air outbreak. *J. Climate Appl. Meteor.*, **25**, 14–21.

Sheu, P. and Agee, E. (1977). Kinematic analysis and air-sea heat flux associated with mesoscale cellular convection during AMTEX 75. *J. Atmos. Sci.*, **34**, 793–801.

Smith, S. (1980). Wind stress and heat flux over the ocean in gale force winds. *J. Phys. Oceanogr.*, **10**, 709–726.

Sorbjan, Z. (1986). On similarity in the atmospheric boundary layer. *Bound.-Layer Meteor.*, **34**, 377–397.

Stage, S. and Businger, J. (1981a). A model for entrainment into a cloud-topped marine boundary layer, part I: Model description and applications to a cold air outbreak episode. *J. Atmos. Sci.*, **38**, 2213–2229.

Stage, S. and Businger, J. (1981b). A model for entrainment into a cloud-topped marine boundary layer, part II: Discussion of model behaviour and comparison with other models. *J. Atmos. Sci.*, **38**, 2230–2251.

Stewart, R. (1979). The atmospheric boundary layer. In *IMO Lecture Series*, volume 3. WMO.

Stull, R. (1988). *An Introduction to Boundary Layer Meteorology.* Kluwer Academic. 666 pp.

Sykes, R., Lewellen, W., and Henn, D. (1990). Numerical simulation of the boundary layer structure during cold air outbreak of GALE IOP-2. *Mon. Wea. Rev.*, **118**, 363–374.

Taylor, G. (1914). Eddy motion in the atmosphere. *Philo. Trans. R. Soc.*, **215**(Series A), 1–26.

Thomas, G. J. and Finney, R. (1979). *Calculus and Analytic Geometry.* Addison-Wesley, 5th edition. 891 pp.

Van der Borght, R. and Agee, E. (1978). Nonlinear convection in a moist atmospheric layer heated from below. *J. Meteor. Soc. Japan*, **56**, 284–292.

Vukovich, F., Dunn, J., and Crissman, B. (1991). Aspects of the evolution of the marine boundary layer during cold air outbreaks off the southeast coast of the united states. *Mon. Wea. Rev.*, **119**, 2252–2279.

Wallace, J. and Hobbs, P. (1977). *Atmospheric Science: An Introductory Survey.* Academic Press. 467 pp.

Walter, B. (1986). *The Mesoscale Organization, Dynamics and Evolution of the Marine Planetary Boundary Layer During Cold Air Outbreaks.* Ph.D. thesis, University of Washington, Seattle, WA.

Walter, B. and Overland, J. (1984). Observations of longitudinal rolls in a near neutral atmosphere. *Mon. Wea. Rev.*, **112**, 200–208.

Walter, B., Overland, J., and Gilmer, R. (1984). Air-ice drag coefficents for first-year sea ice derived from aircraft measurements. *J. Geophys. Res.*, **89**, 3550–3560.

Wayland, R. and Raman, S. (1994). Structure of the marine atmospheric boundary layer during two cold air outbreaks of varying intensities: GALE 86. *Bound.-Layer Meteor.*, **71**, 43–66.

Weaver, A. and Hughes, T. (1995). Flux corrections in coupled ocean-atmosphere models. Submitted to Climate Dynamics.

WMO (1981). Scientific results of the air mass transformation experiment. *GARP Publications Series*, **24**, 236 pp.

Woodcock, A. (1940). Convection and soaring over the open sea. *J. Mar. Res.*, **3**(3), 248–253.

Woodcock, A. (1942). Soaring over the open sea. *Sci. Mon.*, **55**, 226–232.

Wyngaard, J. (1973). *Workshop on Micrometeorology*, pages 101–148. American Meteorological Society.

Wyngaard, J. and Brost, R. (1984). Top-down and bottom-up diffusion of a scalar in the convective boundary layer. *J. Atmos. Sci.*, **41**, 102–112.

Yamada, T. (1976). On the similarity functions A, B and C of the planetary boundary layer. *J. Atmos. Sci.*, **33**, 781–793.

Young, H. (1962). *Statistical Treatment of Experimental Data.* McGraw-Hill. 172 pp.

Zhao, Y. and McBean, G. (1986). Annual and interannual variability of the north pacific ocean-to-atmosphere total heat transfer. *Atmos.-Ocean*, **24**, 265–282.

Appendix A

Objective Analysis

The objective analysis scheme used in this thesis is based on the work of Davis (1985) and on the application of his work by LeTraon (1990). Conventional objective analysis is confined to fluctuations where the larger-scale component of the signal is assumed to be known and is subtracted from the data. Furthermore, the mean field is usually not perfectly known and error maps do not take into account additional error arising from difficulties in distinguishing between the mean field and the mesoscale fluctuations. LeTraon (1990) developed a method for estimating simultaneously the mean field and mesoscale field and incorporating the mean field estimate uncertainty into the error budget. The estimator is a best linear unbiased estimator which has the advantage of being a maximum likelihood estimator for Gaussian fields.

In univariate objective analysis a set of N observations $\Psi_{obs}(\mathbf{x}_i)(i = 1, \cdots, N)$ of a given field Ψ at positions $\mathbf{x}_i = (x_i, y_i)$ is said to consist of a large-spatial scale component and a mesoscale component: $\Psi = \{\Psi(\mathbf{x})\} + \Psi\prime(\mathbf{x})$. The smoothing operator $\{\cdot\}$ is used to define the large scale component and the above expression can be rewritten as:

$$\Psi_{obs}(\mathbf{x_i}) = \{\Psi(\mathbf{x_i})\} + \Psi\prime(\mathbf{x_i}) = \{\Psi(\mathbf{x_i})\} + \Psi''(\mathbf{x_i}) + \epsilon_\Psi(\mathbf{x_i}) \tag{A.1}$$

where,

$\epsilon_\Psi(\mathbf{x_i})$= instrumental error and unresolvable scales of Ψ.

$\Psi''(\mathbf{x_i})$= mesoscale turbulence.

The large scale component is determined by function fitting as outlined in Davis

(1985). He chooses a complete set of functions $F_m(\mathbf{x})$, so that any function f of $\mathbf{x}$ can be expanded over the area of interest.

$$f(\mathbf{x}) = \sum_{m=1}^{\infty} b_m F_m(\mathbf{x_i})$$

The functions $F_m(\mathbf{x})$ can be chosen from a complete set of orthogonal functions such as a polynomial or Fourier series. The smoothing operator $\{\cdot\}$ is then specified to pass the first M functions while rejecting all others:

$$\{\Psi(\mathbf{x})\} = \sum_{m=1}^{M} b_m F_m(\mathbf{x})$$

Therefore the large scale component is defined by the truncated sum over the first M basic functions, assumed to be ordered inversely to their spatial scales.

$\Psi(\mathbf{x})$ is estimated as a linear combination of N observations with the weights $\beta(\mathbf{x}, \mathbf{x}_n)$ selected to minimize the mean square error as in conventional objective analysis:

$$\Psi_{est}(\mathbf{x}) = \sum_{n=1}^{N} \beta(\mathbf{x}, \mathbf{x_n}) \Psi_{obs}(\mathbf{x_n}) \tag{A.2}$$

and,

$$e^2(\mathbf{x}) = \langle [\Psi(\mathbf{x}) - \Psi_{obs}(\mathbf{x})]^2 \rangle_{\text{MINIMUM}}$$

where $\langle \cdot \rangle$ is an average over an ensemble of realizations. The key difference relative to conventional objective analysis lies in the zero-bias constraint on the estimator:

$$\langle \Psi_{est}(\mathbf{x}) - \Psi(\mathbf{x}) \rangle = 0$$

Hence,

$$\sum_{m=1}^{M} \langle b_m \rangle [\sum_{m=1}^{N} \beta(\mathbf{x}, \mathbf{x}_n) F_m(\mathbf{x}_n) - F_m(\mathbf{x})] = 0$$

The mean square error is written as:

$$e^2(\mathbf{x}) = C_{\mathbf{xx}} - 2\sum_{s=1}^{N}\beta(\mathbf{x},\mathbf{x}_n)C_{\mathbf{x},n} + \sum_{r=1}^{N}\sum_{s=1}^{N}\beta(\mathbf{x},\mathbf{x}_r)\beta(\mathbf{x},\mathbf{x}_s)A_{rs} \tag{A.3}$$

where,

$$C_{\mathbf{x}n} = \langle\Psi'(\mathbf{x})\Psi'_{obs}(\mathbf{x}_n)\rangle = \langle\Psi'(\mathbf{x})\Psi'(\mathbf{x}_n)\rangle$$

$$A_{rs} = \langle\Psi'_{obs}(\mathbf{x}_r)\Psi'_{obs}(\mathbf{x}_s)\rangle = \langle\Psi'(\mathbf{x}_r)\Psi'(\mathbf{x}_s)\rangle + \langle\epsilon_\Psi\mathbf{x}_r)\epsilon_\Psi(\mathbf{x}_s)\rangle$$

The minimization problem itself is solved using Lagrange multipliers which when applied to A.2 yields:

$$\Psi_{est}(\mathbf{x}) = \sum_{m=1}^{M}F_m(\mathbf{x})\sum_{k=1}^{M}Z^{-1}_{mk}\sum_{p=1}^{N}\sum_{n=1}^{N}A^{-1}_{np}F_k(\mathbf{x_p})\Psi_{obs}(\mathbf{x_n}) + \sum_{r=1}^{N}\sum_{s=1}^{N}A^{-1}_{rs}C_{\mathbf{x}s}\cdot$$

$$[\Psi_{obs}(\mathbf{x_r}) - \sum_{m=1}^{M}F_m(\mathbf{x_r})\cdot\sum_{k=1}^{M}Z^{-1}_{mk}\sum_{p=1}^{N}\sum_{n=1}^{N}A^{-1}_{np}F_k(\mathbf{x}_p)\Psi_{obs}(\mathbf{x}_n)] \tag{A.4}$$

where,

$$Z_{mk} = \sum_{r=1}^{N}\sum_{s=1}^{N}A^{-1}_{rs}F_m(\mathbf{x}_r)F_k(\mathbf{x}_s)$$

For a field with spatially variable but perfectly known mean, the best linear unbiased estimator at $\mathbf{x}$ is given by:

$$\Psi_{est}(\mathbf{x}) = \langle\Psi(\mathbf{x})\rangle + \sum_{r=1}^{N}\sum_{s=1}^{N}A^{-1}_{rs}C_{xs}[\Psi_{obs}(\mathbf{x_r}) - \langle\Psi(\mathbf{x_r})\rangle] \tag{A.5}$$

The mean field $\langle\Psi(\mathbf{x})\rangle$ is subtracted from each observation value $\Psi_{obs}(\mathbf{x_r})$ and added back to the estimate. The mean field in A.5 is replaced in A.4 by a large-scale estimated field $\{\Psi(\mathbf{x})\}$.

In this study the mean field was estimated using three fundamental functions: $F_1(\mathbf{x}) = 1$, $F_2(\mathbf{x}) = x$, $F_3(\mathbf{x}) = y$ with $\mathbf{x} = (x, y)$. The smoothing operator's properties are implicit

in selection of the M fundamental functions. The choice of the fundamental functions is therefore somewhat subjective and the utility of any estimate of Ψ will depend on whether the implied spatial filter removes or preserves the features of interest. This lack of objectivity is due to the inability to estimate the mean field correlation matrix, $\langle \Psi(\mathbf{x})\Psi(\mathbf{y}) \rangle$. Selection of the number of functions to use in fitting influences the result in two ways. As the number of functions increases, the filter $\langle \cdot \rangle$ becomes less severe and there are more features in Ψ which might be resolved. But the fitting error also increases with M so the analysis becomes less reliable. The mesoscale field was assumed to have a Gaussian distribution with an exponential autocorrelation function given by:

$$C_{rr} = \exp^{-a}$$

where

$$a = \delta x^2 * x_{eff} + \delta y^2 * y_{eff}$$

In the parameter a, δx and δy are the E-W and N-S distances (km) respectively between points on the interpolation grid and x_{eff} and y_{eff} are the $\sqrt{2}\times$ correlation scales (km) which define the ellipse of influence. In this study, $(x, y)_{eff}$ were held constant at 125 km which corresponds to a correlation scale of $\approx$ 90 km in any direction. This spatial symmetry is based on an assumption that the mesoscale turbulence is isotropic and homogeneous.

The effect of not knowing the mean flow appears in the associated error calculation,

$$e^2(\mathbf{x}) = C_{\mathbf{xx}} - \sum_{r=1}^{N}\sum_{s=1}^{N} C_{\mathbf{x}r} C_{\mathbf{x}s} A_{rs}^{-1} + \sum_{r=1}^{M}\sum_{s=1}^{M} Z_{mk}^{-1}[F_m(\mathbf{x}) - G_m(\mathbf{x})][F_k(\mathbf{x}) - G_k(\mathbf{x})] \quad \text{(A.6)}$$

The last term is the additional error due to uncertainty on the mean field.

Lagrange Multipliers It is sometimes inconvenient in physical problems to determine minima by using imposed constraints to eliminate one variable and then to proceed with a smaller number of independent variables. The method of Lagrange Multipliers is an elegant means of minimizing a function $f(x,y,z)$ subject to a constraint $g(x,y,z)=0$. An auxiliary equation is formed from the two functions with the constraint scaled by a constant ξ:

$$H(x,y,z,\xi) = f(x,y,z) - \xi g(x,y,z) \tag{A.7}$$

The final step is finding values of x, y, z, ξ for which the partial derivatives of H are all zero:

$$H_x = 0, \quad H_y = 0, \quad H_z = 0, \quad H_\xi = 0.$$

The constant ξ is often left undetermined since the zero partial derivative constraint acts as a conduit to solving for the relevant variables. A detailed discussion of the method can be found in Thomas and Finney (1979).

Appendix B

Model Parameters

Following is a summary of fields and relevant parameters used as input to the Brown model. The only required model forcing is a grid of sea level pressures (Figure B.1) for estimating surface winds. Additional forcings include sea surface temperature (Figure B.2), near surface air temperature (Figure B.3) and an assumption of 80% relative humidity to both account for stratification and calculate the sensible heat flux. Dew point temperature or relative humidity can be supplied to determine latent heat flux.

Table B.1 summarizes all other pertinent input variables used to initialize the model as well as limits imposed on some of the them.

Default surface drag coefficient	C_D	10^{-3}
Default relative humidity	RH	80%
Input height	z_{in}	10 m
Output height	z_{out}	10 m
Similarity parameter	$\lambda_R = h_p/\delta$	0.15
von Kármán constant	k	0.4
LKB parameter (for surface layer model)	-	2.2
Sea-Air temperature difference	ΔT	$\leq$16.0 °C
Geostrophic wind speed	G	$\geq$2.0 ms^{-1}
Horizontal temperature gradient	∇T	$\leq$3.0 °C 100 km^{-1}
Gradient wind speed	U_{grad}	$\leq 1.3G$

Table B.1: Summary of model input values. A descriptor is given in the first column, with it's symbol name and value appearing in the second and third columns respectively. LKB means Liu, Katsaros and Businger.

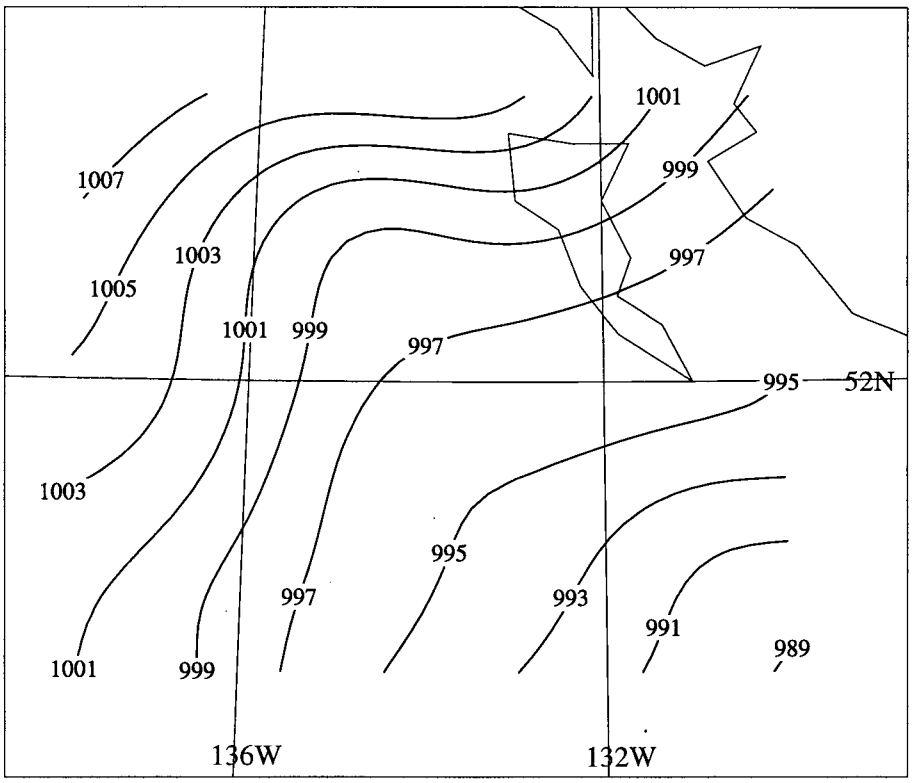

Figure B.1: *MSLP* model input contours with a contour interval of 2 hPa.

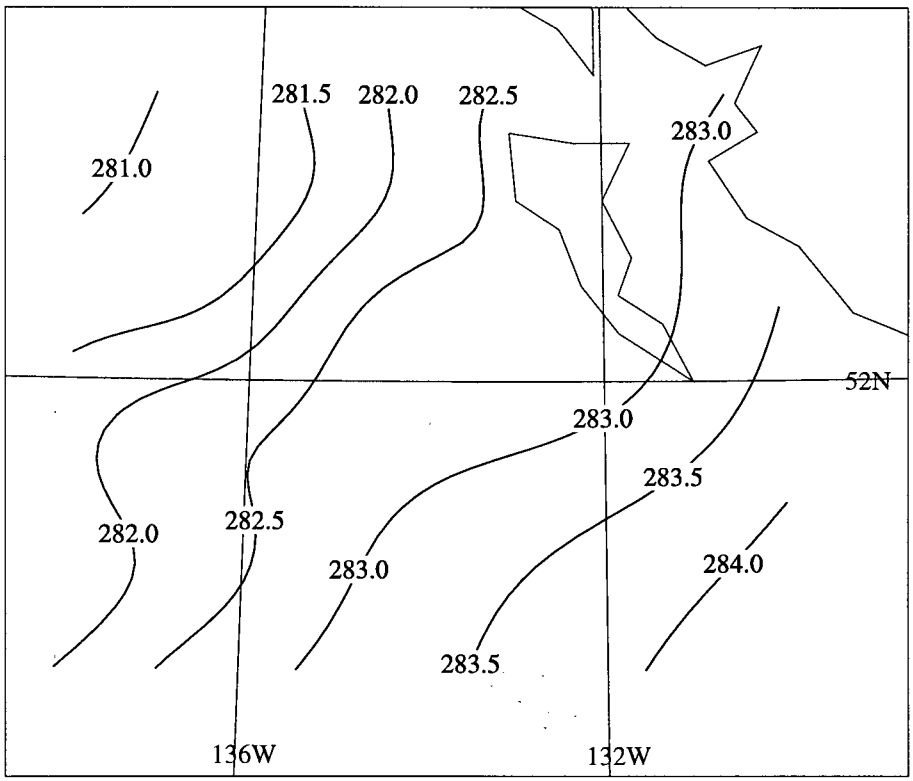

Figure B.2: Sea surface temperature (SST) model input contours with a contour interval of 0.5 K.

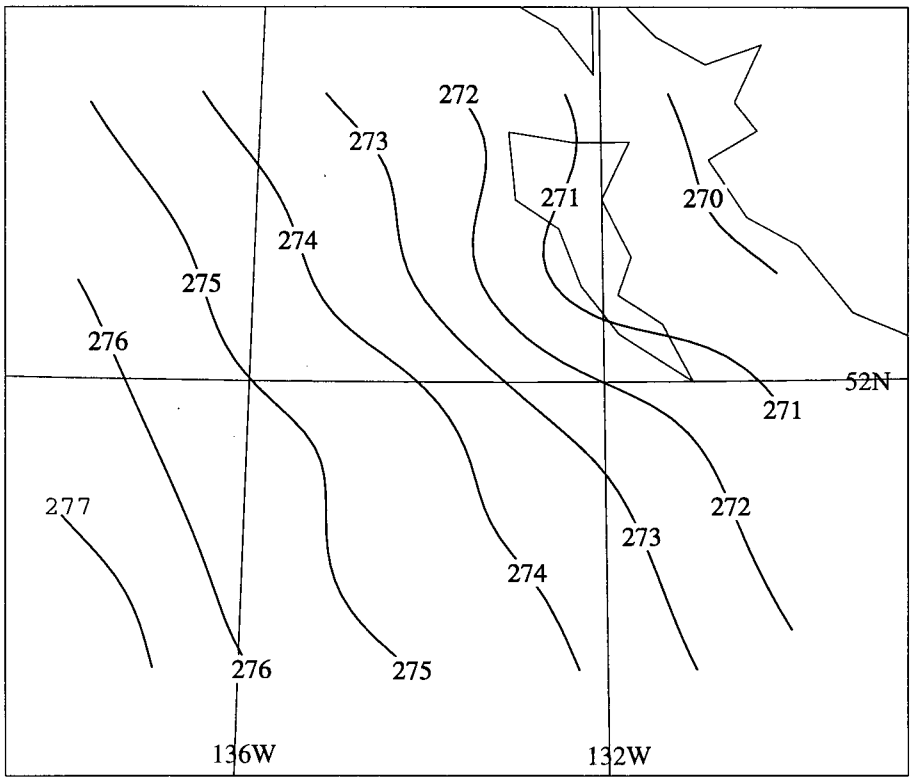

Figure B.3: Surface air temperature (SAT) model input contours with a contour interval of 1 K. Temperatures were corrected to 10 m.